Nanocomposite Silicon and Graphene Composite Negative Electrode Materials for Lithium Ion Batteries

Peter E. Gaskell

Electrical and Computer Engineering
McGill University
Montreal, Canada

December 2016

A thesis submitted to McGill University in partial fulfilment of the requirements for the degree of Doctor of Philosophy.

For Anne.

Abstract

Engineering electrical energy storage systems with high energy density is critical to the adoption of electric vehicles as a green transportation system. The Li-ion battery has the highest energy density of any mature technology and is currently employed in this application. Improving the energy density of the Li-ion battery system requires new electrode materials, for both the anode and cathode, with high volumetric and gravimetric capacity for Li storage. Si is a potential anode material with extraordinarily high gravimetric capacity 4200mAhg^{-1} , as compared to the theoretical limit of 373mAhg^{-1} for conventional graphite electrodes. However, Si is beset by several technical challenges, including the formation of an unstable solid-electrolyte interphase that irreversibly consumes Li, and a 400% volumetric expansion that pulverizes bulk Si. These challenges require novel solutions to realize viable Si based anode technology.

In this thesis, we present a family of engineered Si / graphene composites for anode applications. These composites consist of Si nanoparticles attached to micron scale graphene flakes. We have experimentally shown that the nature of the attachment between Si nanoparticles and graphene flakes - physical, ionic, or covalent - is critical to the suppression of capacity fading in the composite anodes. A covalently coupled composite material containing 60% Si by weight has an initial capacity after formation of 1600mAhg^{-1} , more than 4 times greater than commercial carbon anodes.

We also present a novel strategy for improving the overall capacity of the Li-ion battery anode by eliminating the heavy copper foil current collector. A light-weight, flash reduced graphene oxide thin film current collector is integrated with a high capacity film of graphene encapsulated Si nanoparticles. The resulting two-layered structure forms a single self-supporting, conductive anode film with improved gravimetric capacity of 1100mAhg^{-1} with

60% Si by weight loading. The specific capacity after 200 cycles is stable at greater than $600\mathrm{mAhg}^{-1}$.

The final contribution of this thesis is a comparative study of thermal reduction, flash reduction, and hybrid reduction techniques for the preparation of Si / graphene composites. Flash reduced graphene oxide is open and porous to accept Li ions, but easily disintegrates upon handling. Thermally reduced graphene oxide films are mechanically robust, but exhibit poor electrolyte penetration and poor rate performance. The use of a hybrid reduction technique, first partially thermally reducing films and completing the reduction with a flash process, allows for the tuneable introduction of pores. The films are mechanically robust, have good electrical conductivity, and show much reduced initial capacity loss due solid electrolyte interphase formation. We close the thesis with a discussion of the opportunities and remaining challenges for realizing viable Si / graphene composite anodes.

Sommaire

L'ingénierie de systèmes de stockage d'énergie électrique à haute densité énergétique est essentielle à l'adoption des véhicules électriques respectueux de l'environnement. La batterie Li-ion a la densité d'énergie la plus élevée parmi les technologies matures et est actuellement employée dans ce créneau. L'amélioration de la densité d'énergie du système de batterie Li-ion nécessite de nouveaux matériaux pour fabriquer l'anode et la cathode. Ceux-ci devraient avoir une grande capacité volumétrique et gravimétrique pour le stockage de Li. Le Si est un choix potentiel comme matériau d'anode avec une capacité gravimétrique extrêmement élevée de 4200 mAhg^{-1} comparée à la limite théorique de 373 mAhg^{-1} pour des électrodes traditionnelles en graphite. Cependant, le Si est en proie à plusieurs défis techniques, la formation d'une interphase solide-électrolyte instable qui consomme de façon irréversible le Li et une expansion volumétrique de 400% qui pulvérise le Si entier. Ces défis exigent de nouvelles solutions afin de réaliser une technologie d'anode à base de Si.

Dans cette thèse, nous présentons une famille de composites conçus à base de Si / graphène pour des applications reliées à l'anode. Ces composites sont constitués de nanoparticules de Si attachées aux flocons de graphène de l'ordre du micron. Nous avons démontré expérimentalement que la nature de l'attachement entre les nanoparticules de Si et les flocons de graphène - physique, ionique ou covalente - est essentielle à la suppression du déclin de la capacité dans les anodes composites. Un matériau composite couplé de manière covalente contenant 60% en masse de Si a une capacité initiale après la formation de 1600 mAhg^{-1} ce qui est plus de 4 fois supérieur à celle des anodes en carbone commerciales.

Nous présentons également une nouvelle stratégie pour améliorer la capacité globale de l'anode de la batterie Li-ion en éliminant le collecteur de courant à base de feuilles de cuivre lourd. Une couche mince d'oxyde de graphène, réduit par flash et agissant en collecteur de courant est intégrée à un film de haute capacité de nanoparticules de Si encapsulée dans du graphène. La structure à deux couches résultante forme un seul film d'anode autoportant conducteur avec une meilleure capacité gravimétrique de $1100 \mathrm{mAhg}^{-1}$ avec 60% de Si en masse. La capacité spécifique après 200 cycles est stable à plus de $600 \mathrm{mAhg}^{-1}$.

La dernière contribution de cette thèse est une étude comparative entre la réduction thermique, la réduction avec flash et les techniques de réduction hybrides pour la préparation de composites Si / graphène. De l'oxyde de graphène réduit par flash est ouvert et poreux pour accepter des ions de Li, mais se désagrège facilement lors de la manipulation. Des films d'oxyde de graphène réduits thermiquement sont mécaniquement robustes, mais présentent une pénétration faible d'électrolyte et une performance faible au rendement. L'utilisation d'une technique de réduction hybride, en commençant par la réduction thermique partielle des couches et en complétant la réduction par un procédé de flash, permet l'introduction ajustable de pores. Les films sont mécaniquement robustes, ont une bonne conductivité électrique, et démontrent une réduction des pertes de capacité dues à la formation d'une interphase solide-électrolyte. Nous clorons la thèse avec une discussion sur les opportunités et les défis restant à relever pour la réalisation d'anodes composite à base de Si / graphène.

Acknowledgments

I gratefully acknowledge my advisors Prof. Thomas Szkopek and Prof. Marta Cerutti who provided guidance, resources and encouragement during the course of this project. I would also like to thank members of my thesis advisory committee Prof. Nate Quitoriano and Prof. Ishiang Shih.

I am grateful for the consistent help of my project partners and coauthors Gul Zeb and Kaiwen Hu, who's assistance with chemical synthesis and materials analysis techniques was invaluable. I would also like to acknowledge Dr. Xingcheng Xiao and Dr. Youngnam Kim at General Motors Technical Center in Warren, MI. Without their knowledge, assistance with battery testing, and use of facilities this project would not have been possible.

I am also grateful Philippe Plamondon at the Centre de Caracterisation Microscopique des Materiaux at Ecole polytechnique who coordinated access to an electron microscope after ours was destroyed in a flood.

I acknowledge the assistance Ngoc Duc Trinh and Prof. Steen Schougaard at the Université du Québec à Montréal département de chimie for running some of the battery tests under a commercial agreement. I also acknowledge Seyed Mohammad Valashani, and Prof. Francois Barthelat in the McGill mechanical engineering department for access to mechanical test equipment and assistance in performing mechanical tests.

I am also incredibly grateful for my lab mates Shadi Sabri, Helgi Skulason, Elizabeth Ledwosinska, Jonthan Guillamette, Shariar al Imam, Mohamed Abdelghany, Nick Hemsworth, William Dickerson, and all the others in the lab with whom I collaborated on separate unrelated projects but still provided immense moral support throughout this project and the entirety of my time at McGill. I am ever grateful to Don Pavlasek of the ECE Design & Machining facility who taught me a great deal about the practical side of

things. His friendship and advice were indispensable over the course of this work.

Finally, The following agencies financially supported this work:

General Motor Canada

Canada Research Chairs Program

Natural Sciences and Engineering Research Council

Contents

List of Figures

List of Tables

List of Terms

APS	amino-polysiloxane
C.E.	Coulombic Efficiency
CVD	Chemical Vapour Deposition
DC	Direct Current
DEC	diethyl carbonate
DI	Deionized
DMC	dimethyl carbonate
EC	ethylene carbonate
EDC	1-Ethyl-3-(3-dimethylaminopropyl)carbodiimide
EDX	Energy Dispersive X–ray Spectroscopy
EIS	Electro Impedance Spectroscopy
EMC	ethyl methyl carbonate
EV	Electric Vehicle
FCE	First Cycle Efficiency
FEC	fluoroethylene carbonate
FrGO	Flash Reduced Graphene Oxide
FTIR	Fourier Transform Infrared Spectroscopy
GNP	Graphene Nanoplatelets

GO	Graphene Oxide
HC	Highly Concentrated
HEV	Hybrid Electric Vehicle
HF	Hydrofluoric Acid
HOMO	Highest Occupied Molecular Orbital
HOPG	Highly Ordered Pyrolytic Graphite
LiB	Lithium-Ion Battery
LUMO	Lowest Unoccupied Molecular Orbital
MCMB	Meso Carbon Micro Beads
NP	Nanoparticle
NW	Nanowire
PAN	polyacrylonitrile
PANM	polymethacrylonitrile
PC	polycarbonate
PET	polyethylene terephthalate
PHEV	Plug-in Hybrid Electric Vehicle
PVDF	polyvinylidene fluoride
rGO	Reduced Graphene Oxide
SEI	Surface Electrolyte Interphase
SEM	Scanning Electron Microscopy
SOC	State of Charge
TEM	Transmission Electron Microscopy
TFrGO	Thermal + Flash Reduced Graphene Oxide
TrGO	Thermally Reduced Graphene Oxide

TGA	Thermogravimetric Analysis
UV	Ultra-Violet
XPS	X–Ray Photoelectron Spectroscopy
XRD	X–Ray Diffraction

Chapter 1

Introduction

1.1 Introduction

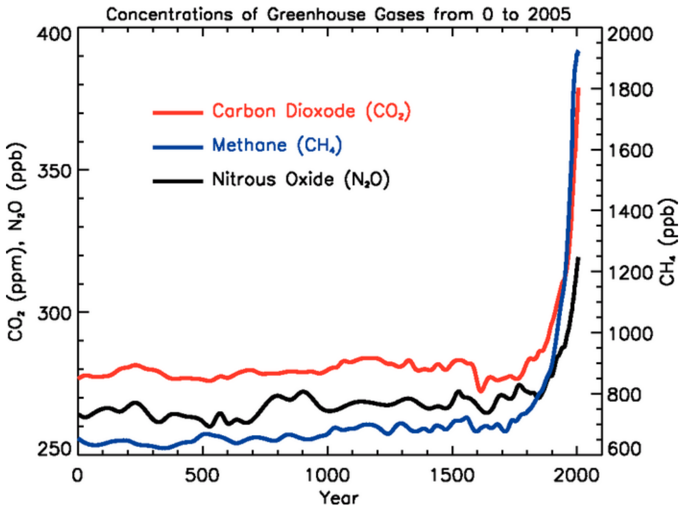

Fig. 1.1 Atmospheric concentration of greenhouse gases produced by combustion of fossil fuels that are contributing to anthropogenic climate change, reproduced from [1].

Environmentally speaking, personal automobiles powered by hydrocarbon fuels are a poor choice for mass transportation. The energy efficiency per passenger kilometre of car travel is lower than for rail travel, most bus travel, and even passenger jet travel [2]. Cars produce large amounts of the greenhouse gases CO_2 and N_2O in a distributed way that makes sequestration prohibitively expensive. These gasses are the two primary contributors to the anthropogenic climate change that has already increased average global temperature by 0.9°C [3]. Fig. 1.1 shows atmospheric levels of the three primary greenhouse gases for the last two millennia derived from measurements of ice core samples in Greenland and Antarctica [1]. Road transportation accounts for 23% of CO_2 emissions in “developed” countries [4] and reducing emissions in this sector is a crucial component of limiting global average temperatures to well below 2°C . Drastically reducing the emissions associated with road transportation requires two solutions. The first would be to drastically reduce the number of small cars and trucks on the road, replacing them with efficient public transportation and human powered modes of transport. Cycling and walking are the most efficient modes of transportation. The second is to replace gasoline vehicles with ones that are powered by electricity, and produce that electrical energy in a way that generates far lower greenhouse gas emissions by using solar, wind, hydro, or nuclear power.

Adoption of technologies is primarily governed by economics and despite the urgent environmental need, electric vehicles will not be widely adopted unless there is some clear advantage in cost or capability. The primary advantage of hydrocarbon fuels is their extraordinary energy density; no rechargeable electrical or electrochemical storage system currently available comes close. A purely economic shift from fossil fuel burning automobiles to potentially cleaner electric vehicles requires technical advances in electrical energy storage systems.

Currently, the best solution to electrical energy storage for electric vehicles (EVs) is the lithium-ion battery. However, realizing the energy capacity required for an EV requires a large, heavy, and expensive battery. This thesis focuses on potential improvements to the capacity of Li-ion batteries by way of improving the capacity of one critical component, the anode. Graphene and Si based composite materials have the potential to increase capacity of anodes 10-fold over current materials. If the storage capacity and lifetime of Li-ion ion batteries can be improved and cost reduced, market penetration of EVs should increase drastically and the emissions from the transportation sector will be reduced significantly.

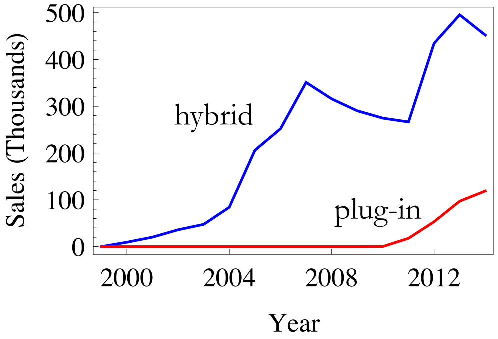

Fig. 1.2 Sales of electric vehicles in the U.S. from 1999 to 2014. An average of 15,000,000 non-electric vehicles were sold per year over this period. Compiled by the Transportation Research Center at Argonne National Laboratory.

1.2 Overview of the Dissertation

This chapter begins by giving an outline of the structure of the dissertation, chapter by chapter. This is followed by a brief history of the Li-ion battery and the technical developments that made the Li-ion battery realizable. Then, the basic operating principles of batteries and Li-ion cells are summarized. Next, Li-ion battery component materials and their properties are catalogued. Finally, a review of the key technical requirements of Li-ion batteries for EVs is given.

Chapter 2 reviews the technology currently employed in commercial battery anodes as well as a review of the literature on advanced carbon and silicon materials for Li-ion battery anodes. This overview includes graphene based materials as well as nanostructured Si materials and composite materials containing both carbon and silicon. The review identifies the physical, electrical, and chemical attributes that facilitate high capacity Li-ion battery anodes.

Chapter 3 describes the methods and tools used in this thesis to characterize the structure and measure the performance of Li storage materials for Li-ion battery anodes. Tools such as scanning and transmission electron microscopy allow the physical imaging of nanoscale structures. The spectrographic and analytical chemistry techniques allow analysis of material composition. Electrical and mechanical measurements are also covered. Finally, key electrochemistry tools commonly used to characterize Li-ion batteries are described.

Chapter 4 traces the production and characterization of coupled graphene nanosheet GNP) and Si nanoparticle (SiNP) materials. The principle objective in this chapter is the direct comparison of uncoupled, ionically coupled, and covalently coupled composite materials to one entirely formed from Si NP. The nature of the coupling has a clear effect on battery performance and covalently coupled materials offer superior performance to the other strategies of composite formation discussed. This work is the first which directly compares composites where the chemical nature of the coupling is the only difference in composition.

Chapter 5 introduces a novel freestanding self-assembled anode material which seeks to replace the copper current collector that is a standard component of commercial batteries. The new material uses a integrated graphitic film for current collection and has a simple and efficient synthesis method. This strategy reduces the ensemble weight of the anode system, increasing significantly the overall gravimetric storage capacity.

Chapter 6 introduces a novel fabrication method for freestanding conductive films with potential applications in Li-ion batteries. Using a dual reduction method, the properties of freestanding graphitic films are shown to be tunable. This work directly improves on the material presented in chapter 5.

Finally, chapter 7 concludes the thesis and discusses challenges and ideas for future work.

1.3 Advantages of Li batteries

Li is lightest metal at standard temperature and pressure, 6.94 g mol^{-1} with a density of 0.53 g cm^{-3}. It is also the most electropositive (-3.04V versus a standard hydrogen electrode). These attributes give Li metal a huge gravimetric capacity compared to other ions used in batteries (Zn and Pb) and allow higher voltage, and thus higher power, cells [5].

While Li is a good material for primary, non-rechargeable batteries, Li metal is unsafe for rechargeable batteries. It is highly reactive and charging forms dendrites on the surface and eventually creates a short circuit internally which destroys the battery. Practical methods of using Li in a rechargeable battery develop a system where Li only exists in ionic form, and not in metallic form.

1.4 Invention of the Li-ion battery

The first rechargeable Li-ion battery prototype was assembled in 1985 by A. Yoshino [6] working for Asahi Kasei Corporation. The cell was designed to overcome safety issues with using pure Li metal as an electrode material by using a novel rocking-horse mechanism. By incorporating two intercalation compounds whereby Li ions could shuttle back and forth across the electrolyte and occupy each material in a different redox potential, Yoshino realized a high voltage (>3 V) cell that withstood mechanical impact without explosive decomposition. The negative electrode material for this cell was formed from graphite, shown to be capable of Li intercalation by electrochemical means by R. Yazami and P. Touzain [7]. The $LiCoO_2$ positive electrode material used had been designed and patented by K. Mizushima, J. B. Goodenough and P.J. Wiseman in 1981 [8]. The technology was then rapidly commercialized by Sony in 1991, and Asahi Kasei and Toshiba in 1992.

1.5 Fundamentals of Lithium-Ion Battery Technology

A Li-ion battery is a galvanic cell. A voltage is held across two electrodes due to the differing electrochemical potentials of two half reactions in two different Li compounds. An oxidation reaction occurs during discharge at the negative electrode, also called the anode. In this reaction, Li ions are oxidized, liberating electrons. The electrons are transported to the positive electrode, or cathode, through the load where a reduction reaction occurs with a free Li ion. This reaction is reversed during charging. In a Li-battery [9] the anode oxidation reaction is:

$$x\mathrm{LiC}_6 \rightleftharpoons x\mathrm{Li}^+ + x\mathrm{e}^- + x\mathrm{C}_6 \tag{1.1}$$

For the cathode, the reduction reaction is:

$$\mathrm{Li}_{1-x}\mathrm{CoO}_2 + x\mathrm{Li}^+ + x\mathrm{e}^- \rightleftharpoons \mathrm{LiCoO}_2 \tag{1.2}$$

The Li ions liberated in each reaction travel back and forth between the anode and cathode inside the cell through the ion conducting electrolyte. The overall electrochemical reaction is:

$$\mathrm{Li}_{1-x}\mathrm{CoO}_2 + \mathrm{LiC}_6 \rightleftharpoons \mathrm{LiCoO}_2 + \mathrm{C}_6 \tag{1.3}$$

Upon assembly of the battery cell, all of the Li in the cell is stored in the electrolyte in the form of Li ions, and in the cathode in the form of a lithium intercalated transition metal oxide. This means the cell is assembled in the fully discharged state as there are no ions in the anode. Upon galvanostatic charging of the cell, electrons flow out of the cathode and into the anode due to an electromotive force provided by the charging circuit. Li ions move from the cathode into the electrolyte solution, and from the electrolyte into the anode. When the anode is saturated with Li ions, the battery is fully charged. When disconnected from the charging circuit and applied to an external load, electrons will flow out of the anode and into the cathode through the external load, while the Li ions in the anode travel to the cathode via the electrolyte. Figure 1.3 shows a schematic of the operating principle of a full Li-ion battery cell.

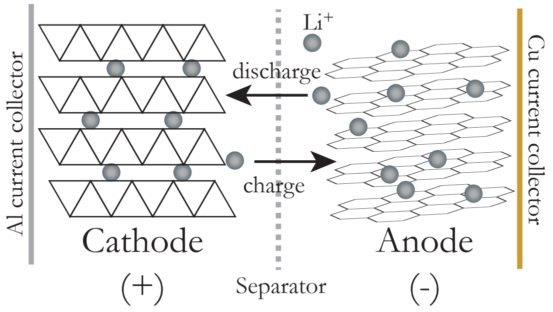

Fig. 1.3 Schematic of the operation of a Li-ion battery. Redrawn from [9]

1.5.1 Energy Bands in the Li-ion Battery

The energy diagram for a Li ion battery cell is shown in fig. 1.4.

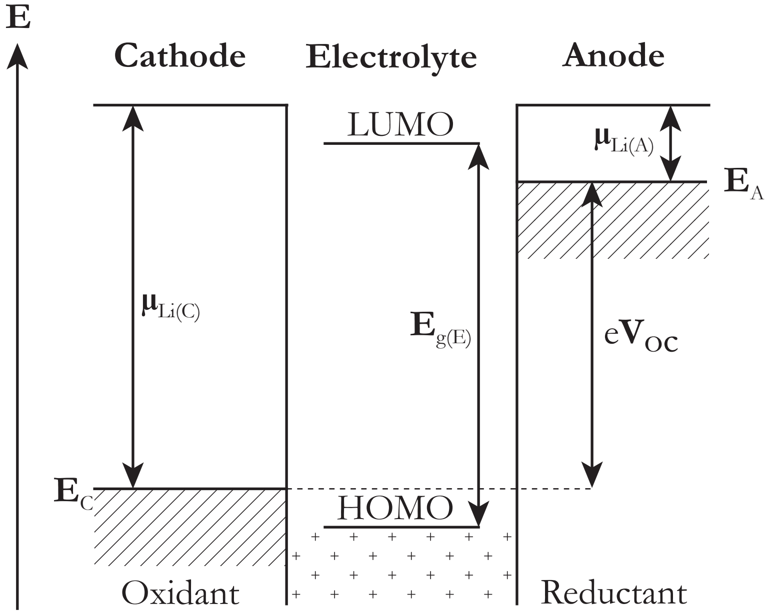

Fig. 1.4 Energy band diagram of a full Li-ion battery. Redrawn from [9]

The open circuit voltage of a lithium-ion battery V_{oc} is related to the difference in chemical potential of Li between the cathode and the anode and is given by:

$$V_{oc} = \mu_{Li(C)} - \mu_{Li(A)} \tag{1.4}$$

Where $\mu_{Li(C)}$ and $\mu_{Li(A)}$ are the work functions for the valence electrons in Li at the anode and cathode respectively. To prevent reduction or oxidation of the electrolyte, the redox energies of the cathode and the anode must lie between the band gap $E_{g(E)}$ of the electrolyte, between the highest occupied and lowest unoccupied molecular orbitals (HOMO and LUMO). This requirement practically means that excessive voltage while charging Li-ion batteries can result in the explosive destruction of the cell. The thermodynamic stability requirement is then that the open circuit energy is less than the energy band gap of the electrolyte:

$$V_{oc} = \mu_{Li(C)} - \mu_{Li(A)} < E_{g(E)} \tag{1.5}$$

When discharged, the internal ionic resistance R_b reduces the open circuit voltage by a polarization voltage $\eta = I_d R_b$. Likewise during charging, this polarization must be overcome by an overcharge voltage $\eta = I_c R_b$. The voltages of the cell during discharging (V_d) and charging (V_c) are then:

$$V_d = V_{oc} - \eta(q, I_d) \tag{1.6}$$

$$V_c = V_{oc} + \eta(q, I_c) \tag{1.7}$$

where q is the state of charge. The maximum charge stored per unit mass Q is known as the capacity of the cell, typically measured in units of mAhg^{-1} , and is given by the integration of all the current into or out of the cell on a given cycle.

$$Q = \int_0^{\Delta t} I dt = \int_0^{Q} dq \tag{1.8}$$

The capacity Q is a strong function of the current and it reduces at high currents because the intercalation of ions into the electrode materials is diffusion limited. This represents a reversible loss in capacity as the cell could be charged or discharged at a slower rate. If there are losses of available Li ions between a subsequent charge and discharge due to irreversible chemical reactions in the cell, there will be an irreversible loss of capacity. The efficiency of a single charge and discharge cycle is known as the Coulombic Efficiency and is given by:

$$\text{C.E.}(\%) = 100 \times \frac{Q_d}{Q_c} \tag{1.9}$$

The energy U available in a cell is then the integral of the output power $P(q) = I_d V(q)$. For a constant discharge current, the energy becomes:

$$U = \int_0^{\Delta t} I_d V_d(t) dt = \int_0^{Q} V_d(q) dq \tag{1.10}$$

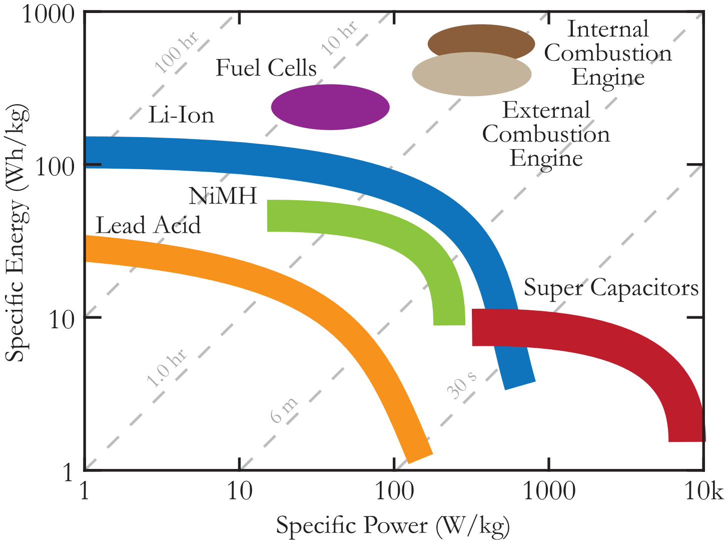

Fig. 1.5 Ragone plot of common electrochemical storage systems. A Ragone plot shows the trade off between power density and energy density for a system. Adapted from [10]

The gravimetric energy density U, which is of particular importance to electric vehicle applications, is dependent on the discharge current. Thus, deriving more power from a battery reduces the available energy. This can be seen in the Ragone plot in figure 1.5. A Ragone plot plots energy density versus power density. Because of the diffusion limited ion transport, all electrochemical storage systems exhibit this trade-off between power and energy density.

1.5.2 Properties of Negative Active Materials

The negative active material is used to store Li in the anode. Ideally Li metal would be used, however the safety issues due to dendrite formation make it unsuitable. Achieving performance near that of metallic Li, without the safety issue, requires a material that can store a large number of Li-ions, and those ions can exist in an electrochemical state close to the potential of Li metal. The electrical and ionic conductivity of the anode material is crucial to the power density of the battery, as a high resistance material will limit the current.

Table 1.1 contains a sample of potential high capacity anode materials. Carbon is the basis of nearly all commercial Li-ion batteries. The potential of Li in carbon is very near that of Li in a metallic state. The capacity however is quite low compared to Li metal and other potential materials.

Silicon is an obvious choice for a high capacity anode. The potential is not quite as low as carbon, but the theoretical capacity is more than a factor of 10 greater, greater even than Li metal. The primary issue with Si materials is however the large volume increase upon lithiation whereas the volume increase for carbon upon lithiation is very small. It is also worth noting the high capacity of Mg, which is another active area of materials research for Li ion batteries.

1.5.3 Properties of Positive Active Materials

A positive active material is used to form the cathode. It must be a good intercalation host to Li ions, while preventing the co-intercalation of electrolyte [12]. It must also be chemi-

Materials	Li	C	Si	Sn	Al	Sb	Mg
Density (g/cm^3)	0.53	2.25	2.3	7.3	2.7	6.7	1.3
Lithiated phase	Li	LiC_6	$Li_{4.4}Si$	$Li_{4.4}Sn$	LiAl	Li_3Sb	Li_3Mg
Theoretical capacity (mAh/g)	3862	372	4200	994	993	660	3350
Volume Change (%)	100	12	420	260	96	200	100
Potential vs. Li (V)	0	0.05	0.4	0.6	0.3	0.9	0.1

Table 1.1 Table of potential high capacity anode materials adapted from [11]

cally compatible with and stable in the electrolyte used. Having a low chemical potential level and Li-ion site energy allows for a high open-circuit voltage. The ability to intercalate large amounts of Li-ions is critical for energy density, and to do so at a high intercalation rate is critical for power density. The molecular mass and volume of the material per intercalated ion determines the gravimetric and volumetric density respectively.

In addition to the chemical requirements, the price of raw materials and cost of production must be reasonable. Cathode materials are the most expensive aspect of Li-ion battery production, and account for almost 50% of the cost of the battery [13]. With the high cost of cathode materials, the ability to recycle the materials after the usable lifetime of a battery becomes a serious consideration.

1.5.4 Electrolyte

The electrolyte provides a medium for ionic transport in a battery. Earlier batteries such as NiMH use an aqueous electrolyte for the transport of H+ ions. The electrochemical stability window of water limits the cell operating voltage to 1.5V. The primary motivation to move to Li ion batteries was the expansion of this window. By moving to an organic solvent, typically a carbonate, the stability window can be increased up to about 4V. The higher cell voltage immediately provides double the power output for the same ionic current. The particular battery application typically determines the formulation of electrolyte, which consists of a Li salt in a solvent. There are half a dozen salts normally used in Li-ion battery electrolyte, as shown in Table 1.2. The most commonly used Li salt is $LiPF_6$. A battery designer may also tune performance with the wide selection of organic solvents and combinations. The most common electrolytes , as shown in Table 1.3, are made from mixtures of various carbonates. The choice of salt and solvent affect ionic conductivity at the operating temperature range as well as the side reactions in a Li-ion cell that may help or hinder the performance of the battery.

Name	Formula
lithium hexafluorophosphate	$LiPF_6$
lithium tetrafluoroborate	$LiBF_4$
lithium perchlorate	$LiClO_4$
lithium hexafluoroarsenate	$LiAsF_6$
lithium triflate	$LiSO_3CF_3$
lithium bisperfluoroethane-sulfonimide	$LiN(SO_2C_2F_5)_2$

Table 1.2 Table of common Li salts for Li-ion batteries. Adapted from [14]

Acronym	Name	Formula
EC	ethylene carbonate	$(CH_2O)_2CO$
PC	propylene carbonate	$CH_3C_2H_3O_2CO$
DMC	dimethyl carbonate	$OC(OCH_3)_2$
EMC	ethyl methyl carbonate	$C_2H_5OCOOCH_3$
DEC	diethyl carbonate	$OC(OCH_2CH_3)_2$

Table 1.3 Table of carbonates for Li-ion battery electrolyte solvents. Adapted from [14]

1.5.5 Separator

The separator is a 10μm to 30μm thick microporous membrane used to physically isolate the anode and the cathode sides of the battery. The membrane is typically made from polyethylene or polypropylene or a combination of the two. The key property of the separator with respect to lithium-ion batteries is the ability to readily transport ions across the barrier through the micropores, typically 30nm -100nm while preventing electrical contact which would cause an internal short and likely explosive decomposition of the electrolyte. Because of this safety concern, separators must also be resistant to puncture and stable in contact with electrolytes. The manufacturing process requires the separator to have high yield strength so it may be used in automatic winding machinery.

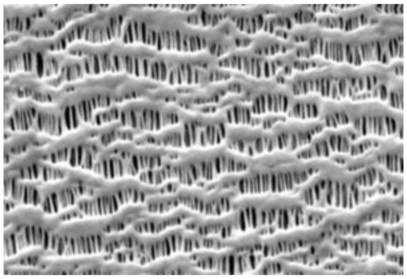

Fig. 1.6 SEM micrograph of Celgard brand separator from the manufacturer website. The microporous structure allows the free flow of ions across the barrier, but prevents unintentional electrical internal contact between the anode and cathode that would result in the cells rapid destruction.

1.6 Technical Requirements for Electric Vehicle Batteries

The adoption of Li-ion battery technology for both plug-in electric vehicles (EV) and hybrid (HEV) and plug-in hybrid (PHEV) electric vehicles by the automotive industry was a necessary move. From purely an energy density perspective, Li-ion is the only current rechargeable battery technology coming close to the energy density of an internal combustion engine system utilizing some form of hydrocarbon fuel, be it gasoline, diesel, ethanol, or natural gas (see Fig. 1.5). The range of the 2014 Chevrolet Volt, with its 16.5 kWh, 200kg Li-ion battery pack can store the energy equivalent of 3.5L of gasoline weighing 2.6kg. There is significant room for improvement in Li-ion batteries.

1.6.1 Energy Density

Energy density, or specific energy, typically measured in $^{\text{kWh}}/_{\text{kg}}$ is a critical parameter of the battery. As energy density is improved, the mass of a vehicle can be reduced, decreasing the energy needed to reach travelling speed. In addition a higher energy density allows for longer distances between charging cycles. This would alleviate “range anxiety,” identified as a major barrier to the widespread adoption of EVs. Energy density can be increased, holding other parameters constant, by increasing the voltage, decreasing the mass, or improving the capacity of each cell.

1.6.2 Power Density

EVs require a certain power density to accelerate and sustain the velocity of the automobile. To accelerate a vehicle from a stop at the typical vehicle acceleration of 2.5 $^{\text{m}}/_{\text{s}^2}$ (0-80 kph in 8.9 s) to the typical highway speed of 80kph requires the battery deliver nearly 100 kW. The power output of the electric motor of the 2014 Chevrolet Volt is 111 kW. The battery achieves this power output with its 288 cells arranged 3 in parallel by 96 in series, giving the pack a voltage of 360 V. Delivering the maximum power to the electric motor requires each cell to deliver over 100 A of current. Improving power density of calls would allow using fewer parallel cells in a battery system.

1.6.3 Capacity

The energy density of automotive gasoline is about 12 $^{\text{kWh}}/_{\text{kg}}$. At a density of 0.75 $^{\text{kg}}/_{\text{l}}$, the capacity of a typical 70 l gas tank can hold over 600 kWh of energy at a weight of 50 kg. The 2014 Chevrolet Volt has a 16.5 kWh, 360 V Li-ion battery pack weighing 200kg. Table 1.4 shows target specifications of batteries for different classes of EVs.

	HEV	PHEV	EV
Power (kW)	30	150	160
Energy (kWh)	2	9	28
Mass (kg)	19	89	210
Specific Power (W/kg)	1500	1715	762
Specific Energy (Wh/kg)	100	110	130
Range (km)	N/A	48	160

Table 1.4 Table of target specifications for batteries depending on application from the U.S Department of Energy [15]

1.6.4 Cycle Ability

A fundamental issue for batteries used in EVs is the number of charge cycles they are able to endure before the capacity falls too low to be useful. The operational life of an average car is 10 years. Because the battery is a significant cost fraction of an EV, reducing the total cost of ownership requires batteries that would not need to be replaced within the lifetime of the car. For an EV battery to survive through 300 charge cycles a year for the life of the car, the battery should not decrease by more than 20% of the initial capacity after 3000 cycles. This requires batteries to have Coulombic efficiencies approaching 99.995%. Measuring efficiency as high as this requires voltage and current measurements with better than 10ppm accuracy [16]. To improve the cyclability of the battery electric vehicles, the state-of-charge (SOC) is kept between 30% and 80%. This reduces the usable energy of the battery but significantly increases the Coulombic efficiency and thus the lifetime of the battery. The battery cells in the Volt are estimated to handle 6000 cycles without significant degradation.

1.6.5 Safety

Safety is a primary concern for the use of Li-ion batteries in electric vehicles. In a typical EV battery, electronics frequently monitor the cell voltage and SOC of the battery to ensure it does not exceed safe operating range. Cells are typically designed with thermal fuses to prevent destructive thermal run-away in the event of failure. The temperature of an EV battery is regulated using electric heating and coolant to maintain an optimal operating temperature near 20°C and to prevent overheating. The casing of the battery assembly is reinforced with steel to prevent damage in a crash.

1.7 Mass of components of EV batteries

The heaviest part of any battery is the cathode. The cathode active material accounts for nearly a third of the mass of the battery. Including the aluminium current collector, the cathode accounts for nearly half. The anode active material accounts for less, 15%, but with the copper current collector this figure rises to 25%. Table 1.5 summarizes the components of mass in three example HEV, PHEV, and EV battery systems.

	Percent Mass		
Component	HEV	PHEV	EV
$LiMn_2O_4$	27.0	28.0	33
Graphite	12.0	12.0	15
Binder	2.1	2.1	2.5
Copper	13.0	15.0	11.0
Aluminum	24.0	23.0	19.0
$LiPF_6$	1.5	1.7	1.8
EC	4.4	4.9	5.3
DMC	4.4	4.9	5.3
PP	2.0	2.2	1.7
PE	0.26	0.40	0.29
PET	2.2	1.7	1.2
Steel	2.8	1.9	1.4
Thermal Insulation	0.43	0.33	0.34
Glycol	2.3	1.3	1.0
Electronic Parts	1.5	0.9	1.1

Table 1.5 Table of the relative mass of components of typical electric vehicle batteries from the U.S Department of Energy [15].

1.8 Thesis Original Contributions

The research presented in this thesis was done as part of an industry/academic partnership with General Motors Canada with help from the technical staff at the General Motors Warren Technical Center in Warren, Michigan. The focus of this partnership was the investigation of new materials and strategies to produce high energy density Li-ion battery anodes, specifically for the automotive industry. The work presented here on functionalized graphene and Si nanoparticle materials was only a part of the investigations, which also included studies of functionalized graphene and Sn nanoparticle anodes and work on producing these materials using an electrospray production method.

While there is a large body of research in this general area, many of the successful materials and production methods presented in the literature were decided to be cost prohibitive for the needs of automotive batteries. Many of the design choices made were in order to reduce the cost of precursor materials and complexity of synthesis techniques. The ultimate goal of this work was to find cost effective routes to produce high capacity anode materials specifically for the automotive industry.

The original contributions reported in this thesis are:

- **First direct comparison of coupling techniques for performance of SiNP/Graphene anode materials.** This work shows the importance of covalent coupling for immobilization of Si NP on Graphene flakes. Covalently coupled graphene and Si NP materials exhibit higher specific capacity after repeated charge and discharge cycles than ionically or physically coupled graphene and Si NP materials with the same initial capacity.

- **First use of dual layered rGO/rGO-SiNP freestanding material as an anode material.** This work demonstrates a novel technique to engineer new layered materials for electrodes in electrochemical devices.

- **First documentation of the performance of Flash reduced Si/GO composite materials.** This material holds Si NP in a porous carbon structure and displays stable long term capacity greater than presently used commercial anode materials.
- **Introduction of a novel graphene oxide two step reduction technique.** This technique allows efficient and tunable introduction of pores into reduced graphene oxide films, and has potential applications in high capacity batteries and electrochemical super capacitors.

1.9 Relevant Publications and Co-Author Contributions

The publications associated with the work presented in this thesis are:

1. "Decoration of Graphitic Surfaces with Sn Nanoparticles through Surface Functionalization Using Diazonium Chemistry," Gul Zeb, **Peter E. Gaskell**, Xuan Tuan Le, Xingcheng Xiao, Thomas Szkopek and Marta Cerruti. Published August 7, 2012 in Langmuir.

   The author of this thesis performed microscopic image analysis, Raman spectroscopy, the analysis of surface functionalization density, and the analysis of nanoparticle size distribution and surface density. Co-authors of this work performed material synthesis and chemical analysis. The work was supervised by Thomas Szkopek and Marta Cerruti.

2. "The importance of covalent coupling in the synthesis of high performance composite anodes for lithium ion batteries," Gul Zeb, **Peter E. Gaskell**, Young Nam Kim,

Xingcheng Xiao, Thomas Szkopek and Marta Cerruti. Published May, 2016 in RSC Advances.

The author of this thesis performed Raman spectroscopy, some SEM imaging, and assisted with the analysis of battery cycling results, particularly the differential capacity analysis. Cell fabrication for reference cells, chemical production and functionalization of precursor materials as well as operation of XPS and TGA instruments were performed by co-authors. Thomas Szkopek and Marta Cerruti supervised this work.

3. "Freestanding micro/nano layered graphene/silicon nanocomposites for lithium-ion battery anodes," **Peter E. Gaskell**, Gul Zeb, Kaiwen Hu, Xingcheng Xiao, Thomas Szkopek and Marta Cerruti. In preparation.

   Material fabrication, Raman analysis, SEM imaging, cell fabrication for the freestanding anode devices and analysis of battery cycle performance were performed by the author. Cell fabrication for reference cells, chemical production and functionalization of some precursor materials as well as operation of XPS and TGA instruments were performed by co-authors. Marta Cerruti and Thomas Szkopek supervised this work.

4. "Two step reduction of graphene oxide films allows tunable surface porosity," **Peter E. Gaskell**, Gul Zeb, Kaiwen Hu, Marta Cerruti and Thomas Szkopek. In preparation.

   Inception of reduction method, preparation of all materials, mechanical testing, SEM imaging, cell fabrication for some freestanding anode devices, and analysis of battery cycle performance were performed by the author. Fabrication of TFrGO cells were done as part of a commercial agreement. Cell fabrication for reference cells, chemical production and functionalization of some precursor materials as well as operation of XPS and TGA instruments were performed by co-authors. Marta Cerruti and Thomas Szkopek supervised this work.

Work reported in this thesis was also presented in a series of technical reports to General Motors under the requirements of an Natural Sciences and Engineering Research Council of Canada Collaborative Research Development grant.

1.10 Publications Resulting from Methods Described in this Thesis

In addition to the publications above, the methods described for the production of large area graphene oxide paper films were used in the following published works:

1. "Bolometric response of free-standing reduced graphene oxide films." W. Dickerson, N. Hemsworth, **P. Gaskell** and E. Ledwosinska and T. Szkopek, Applied Physics Letters (2015) vol. 107, 243103.

2. "Graphene Oxide Based Materials as Acoustic Transducers: A Ribbon Microphone Application Case Study." **P. Gaskell**, R.E. Gaskell, J.W.J. Hong, and T. Szkopek. Proceedings of the 137th Audio Engineering Sociey Convention.

3. **P. Gaskell**, R.E. Gaskell, J.W.J. Hong, and T. Szkopek. "Graphene Oxide Based Acoustic Transducer Methods and Devices" U.S. Patent Provisional Application No. 62/060,043, filed October 6, 2014.

Chapter 2

Literature Review: Carbon, Silicon, and Composite Materials for Advanced Li-ion Battery Anodes

2.1 Introduction

The anode material for nearly all commercial Li-ion batteries is some form of carbon. The use of graphitic anode material was the breakthrough that made rechargeable Li-ion batteries possible. The ability to store significant numbers of Li ions in an intercalation compound slightly less electro-positive than pure lithium metal allows for the maximum open circuit voltage and mitigates the deleterious effects of Li dendrite growth. The high conductivity of graphitic carbon materials allows for high current density. Presently, graphitic anode materials are a mature technology, inexpensive to produce, and well understood. There is, however, a fundamental limit to the capacity of a graphitic anode that makes alternative materials very appealing for improving the energy density of batteries.

Silicon is one such material, with theoretical capacity over ten times that of graphite [17]. The significant limitations of Si materials and their potential resolution by moving to the nano-scale is a major avenue of research in the field of high capacity anode materials. Similarly, graphene, the isolated 2D crystal that forms the layers of graphite, is another material with great potential. The ability to engineer, layer by layer, the nano-structure of a material is one of the major prospects of graphene research, and could provide an unprecedented level of control over material properties.

2.2 Carbonaceous Anodes

In carbonaceous materials, Lithium storage is strongly dependent on the nanostructure of the material, and different materials can provide specific advantages when engineering the performance of an anode in terms of power density, energy density or cycle lifetime. The ideal anode material would facilitate high power, high capacity, long life batteries that have low weight and a small size. In reality there are trade-offs to be made. The materials currently used are all forms of carbon, and fall into three general categories: graphite (either natural or synthetic), soft carbon, and hard carbon. The structural differences in these forms of carbon, and the relationship between the structure and heat treatment are shown in Fig. 2.1. More recently, another form of carbon, graphene, has been studied as a potential anode material.

2.2.1 Graphite

Graphite is a carbon crystal with the stacked hexagonal planer structure shown in Fig. 2.2. Graphite has high strength sp2 hybidized bonds in-plane but individual layers are weakly bonded to adjacent layers by van der Waals potential. Stacking can occur with different

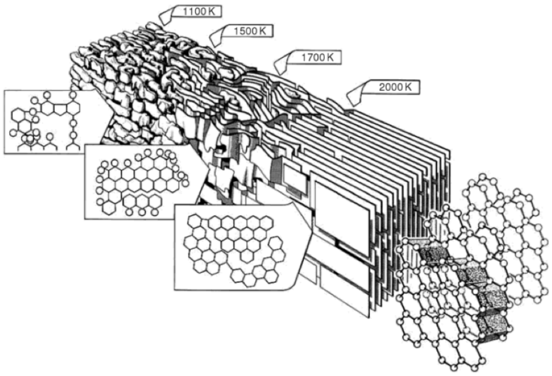

Fig. 2.1 The evolution of carbon from amorphous to crystalline graphite with heat treatment. Reproduced from [18]

spacial offsets, though, direct AA stacking is less energetically favourable than the more common AB stacking shown. The weak interlayer bonding allows the diffusion of ions in between layers. Li ions can readily diffuse between graphite layers forming an intercalation compound with Li with a stoichiometric formula of LiC_6[19]. The diffusion coefficient for Li in graphite is around $10^{-8}\ \frac{\mathrm{cm}^2}{\mathrm{s}}$ [20]. Used as a Li-ion battery anode this allows the storage equivalent of one electron per 6 carbon atoms, corresponding to a theoretical gravimetric capacity of $371.95\mathrm{mAhg}^{-1}$. Generally, the actual capacity in a commercial anode material is lower, typically 280-330mAhg^{-1} [21].

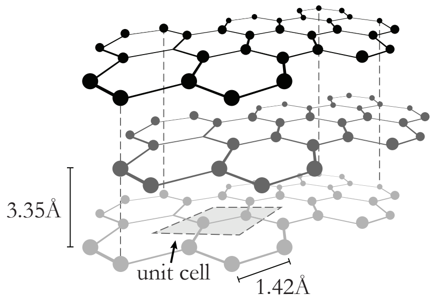

Fig. 2.2 Diagram of the crystal structure of graphite with common Bernal (AB) stacking.

Because of the energy required to overcome the van der Waals forces and to separate the individual layers of the graphite crystal, the intercalation of Li happens in discrete stages as shown in Fig. 2.3. Stage IV represents a lightly lithiated graphite structure, with randomly intercalated Li ions. As more Li is added to the graphite structure, it favours intercalating into layers already separated by some Li ions until stage III when those layers are saturated. When a layer is saturated, opening a new layer requires additional free energy in the form of an electrochemical potential[7]. During intercalation in each stage the potential remains static, while the ionic current is non-zero. Stage II occurs between the stoichiometric ratios of $Li_{0.33}C_6$ and $Li_{0.5}C_6$, where alternate layers are occupied and unoccupied with Li ions, the splitting between IIL and II is due to differences in Li packing density in the plane. Finally in stage I, the graphite structure is fully saturated with Li ions.

In order to promote adequate Li diffusion for suitable charge and discharge rates, the ratio of surface area to volume should be high. In order to achieve a high ratio using natural graphite, the flakes must be purified and milled into a fine powder in order to be suitable for battery production. The financial costs associated with mining and purifying graphite, then grinding it into a fine powder are large compared to the costs associated to synthesizing the power from other carbon sources. Therefore, unless there is a specific need for very pure graphite, the majority of anodic powders are synthesized from other sources producing either hard or soft carbon.

2.2.2 Soft Carbon

Soft carbon anode materials are made from hydrocarbon precursors, primarily tar and pitch, that graphitize when pyrolyzed. On short length scales they have the same layered structure as graphite, though the layer spacing is variable and greater than that of graphite. On longer length scales they resemble a more disordered form carbon. Soft carbons have

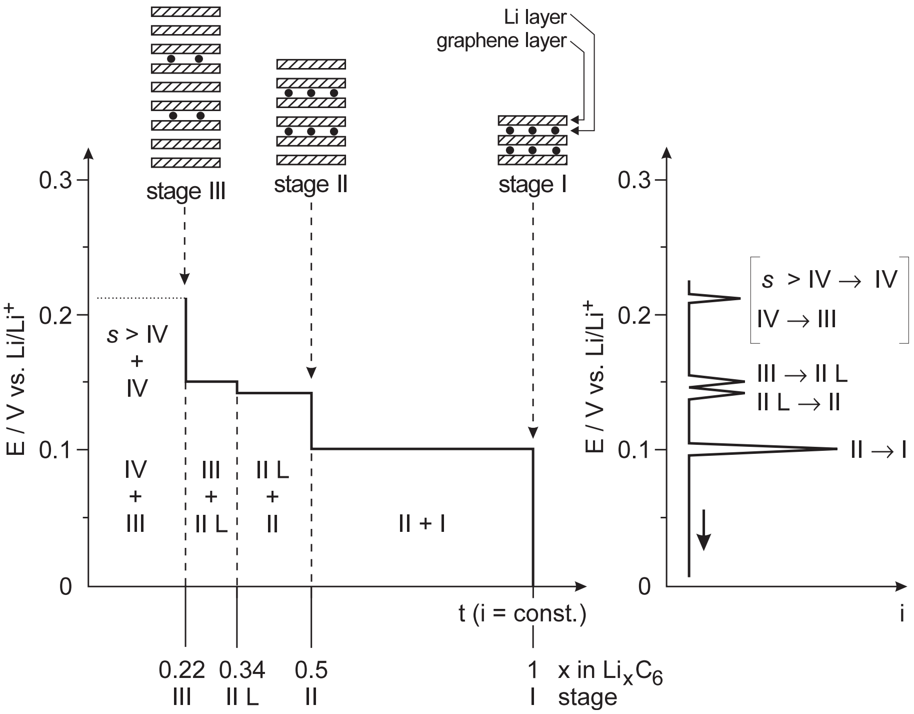

Fig. 2.3 Intercalation stages of Li insertion into graphite reproduced from [19]. On the left is the schematic representation of the galvanostatic curve, on the right is the schematic of the voltammetric curve. In the last stage, LiC_6, the electrochemical potential is only 0.1V above atomic Li.

lower first cycle efficiency, and greater irreversible capacity, but can have a greater reversible capacity than graphite because of the increased layer spacing and large surface area and edges for Li adsorption[19].

2.2.3 Hard Carbon

Hard carbons are formed from precursors such as petroleum coke or sugars that do not graphitize when pyrolyzed [22]. The disordered structure of hard carbon has many more defect sites than graphitic carbons, allowing greater lithium storage and thus higher reversible capacity approaching $1000\mathrm{mAhg}^{-1}$ [21]. Hard carbons are processed at a much lower temperature (1100°C vs 3000°C) than graphitizable carbons, and thus have a lower energy cost in production. The defects, however, also contribute to the over-formation of an SEI layer on the material, causing significant irreversible capacity loss after the SEI is formed during the first charging cycle. This initial capacity loss can be overcome by the introduction of extra positive electrode material, but the extra material is wasted as it only participates in the initial cycle, and no subsequent cycles.

2.2.4 Graphene

Graphene is a single layer of a graphite crystal; It was only recently successfully isolated directly from bulk graphite in 2004 by Geim and Novoselov [23]. Using only Scotch Tape, they showed it possible to mechanically cleave single layers from a graphite crystal. Previous efforts to isolate graphene date back to 1859 when Brodie, in order to determine the atomic weight of graphite, developed a method to chemically exfoliate layers from bulk graphite [24]. The isolated layers were oxidized by the process into a form now termed graphene oxide. The method of producing graphene oxide was refined by Hummers and Offeman in the late 1950s [25]. This method is presently the most common route for the synthesis of graphene oxide [26]. Graphene oxide can be reduced to graphene by various processes, including thermal and chemical methods. While the production and reduction processes introduce significant defects compared to directly isolated graphene, the quality is sufficient to produce electrode materials.

Graphene offers several advantages over graphite materials in Li-ion anode applications. In graphite, Li intercalates between layers Because Graphene is a single isolated carbon layer, Li ions can theoretically adsorb on both sides of the crystal structure. This process does not require an excess of energy to open the layer structure to intercalation. Graphene has been shown to have a higher reversible capacity than graphite [27] [28]. Density of State calculations for very small graphene flakes (containing between 24 and 216 carbon atoms) suggest the addition of edge states for Li binding actually give a maximum stoichiometric formula of Li_4C_6 [29]. The introduction of nitrogen or boron defects can improve the capacity of Graphene [30][31].

2.3 Si Anodes

Silicon is an attractive next generation anode material for Li-ion batteries. Compared to carbon materials, Si forms high capacity compounds with Li. The highest capacity compound $Li_{22}Si_5$ [17] has a maximum theoretical capacity of $4200 mAhg^{-1}$ [32], the highest gravimetric capacity of any Li containing compound [33]. Silicon is also an abundant natural material and has good electrical conductivity when doped or in polycrystalline form. In addition, the electrochemical potential of formation is close to that of metallic Li, allowing batteries made with Si anodes to achieve a high open circuit voltage. Finally Si has a low reactivity and low toxicity, both of which are important concerns when considering a vehicle battery system's safety. These factors are all favourable to silicon's use as a battery anode.

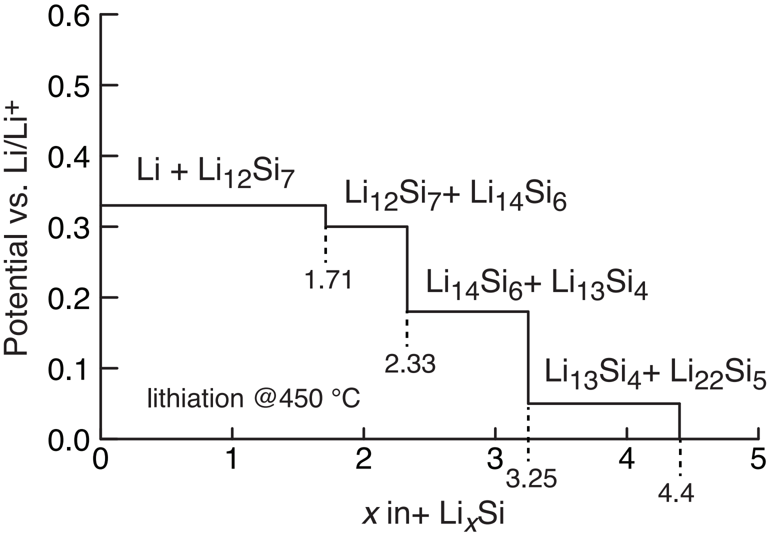

Fig. 2.4 High temperature electrochemical Si lithiation curve. Reproduced from [34].

The primary challenge with the use of bulk Si in anodes is the large volume expansion upon lithiation. The space occupied by the high capacity compound $Li_{22}Si_5$ is 2.5× that of the silicon alone [35]. This 250% volume expansion means in most cases bulk silicon will fracture and break apart when used as an anode. Once broken away from the anode, the fractured Si will no longer be in electrical contact with the current collectors and no longer participate in the rocking-chair reaction, leading to irreversible capacity and severe capacity fading [36].

One possible way to mitigate the volume expansion of Si anodes is to use nanostructured Si materials [32, 37]. The inherent strength of nanostructures allows for the volume expansion to occur without mechanical degradation. The nanostructuring of Si can be achieved in one, two, or three dimensions in order to produce thin films, nanowires, or nanoparticles respectively. In the following sections these three forms of nanostructured Si are reviewed.

2.3.1 Si Thin Films

A very thin film, if it is thin enough, will expand mostly in out-of-plane direction, preventing the material from breaking apart. Bourderau et. al. found amorphous silicon films with a thickness of 1.2μm failed after only a few cycles [36]. Takamura et. al. deposited five different thicknesses of Si from 100nm to 3.6μm on a roughened current collector and found capacity fading increased with the thickness of the films [38, 39]. The rough surface morphology was found to improve the performance. Guo et. al. found amorphous Si films sputtered on roughened Cu foil exhibited a dramatic drop in gravimetric capacity as the film thickness increased above 300nm [40].

Graetz et. al. used CVD to deposit 100nm films on smooth Ni foil and reported stable performance of 1800mAhg^{-1} after a large initial capacity loss [41]. Ohara et. al. similarly explored thin Si films on Ni foils and found stable capacity over 3500mAhg^{-1} for 50nm films but only 2500mAhg^{-1} for 150nm films [42]. Jung et. al. found silicon films with thickness less than 50nm provide good reversibility and high capacity, with a reversible capacity of 3800mAhg^{-1} after 200 cycles [43]. It is clear with thin films of Si, performance increases as the thickness decreases. This simple relationship has a fundamental problem, however— making the Si anode layer very thin makes the areal capacity very low, even if the gravimetric capacity is high. An anode with such low areal capacity is not practical for a commercial battery system.

2.3.2 Si Nanowires

For Si nanowires (NWs), volume expansion occurs mostly in the radial direction. NWs anchored vertically on one end to a current collector allow the wires to maintain electrical connectivity while expanding radially. The efficiency of electron transport in Si NP is such that even longer wires can provide a low resistance path for current collection. The high surface area of nanowires is favourable to Li diffusion dynamics allowing faster charging and discharging. Crystalline nanowires will turn amorphous upon lithiation, but amorphous Si is still a high capacity material.

There are several routes to the production of Si NW. Cui et. al. demonstrated CVD grown nanowires on steel foil with a gravimetric capacity of 1000mAhg^{-1} after 100 cycles [44]. Chan et. al. produced NW anodes with gravimetric capacity of 3500mAhg^{-1} using a Vapor-Liquid-Solid (VLS) method. They found the wires remained intact despite an increase in both length and diameter corresponding to approximately 400% volume expansion [45]. Citing the VLS growth process as a prohibitively expensive method, Chan et. al. demonstrate Si NW anodes solution grown with a Supercritical Fluid-Liquid-Solid (SFLS) method [46]. They report a gravimetric capacity of 1500mAhg^{-1} for 30 cycles. Chockla et. al. demonstrate a freestanding Si NW fabric created from solution grown Si NWs with an initial capacity of 1485mAhg^{-1} falling to 804mAhg^{-1} after 20 cycles. Ge et. al. produced porous Si NW anodes by direct etching of Boron doped Si wafers. The porous NW, isolated in powder form and mixed with an Alginate binder, exhibited a gravimetric capacity >3400mAhg^{-1} for 10 cycles at low charge rates (C/6), and better than 1100mAhg^{-1} for 250 cycles even at high rate approaching 5C [47]. They conclude the porosity is critical for good cyclability.

2.3.3 Si Nanoparticles

Although the use of Si in a nano-particle form allows the mitigation of volume expansion, Si nanoparticles alone do not make effective anodes. This is particularly because of the poor transport properties of agglomerations of Si NP [48]. Adding conductive additives can aid electron transport. Li et. al. demonstrated a Si NP anode with 70nm particles with a significant amount of carbon black conductive additive in a PVDF binder with a reversible 1700mAhg^{-1} after 30 cycles [49]. Kim et. al. demonstrated that the capacity of a Si NP based anode varies significantly with particle size, with smaller particles improving capacity, and 10nm Si NP have the most stable capacity [50].

The SEI created between Si and the electrolyte upon Lithiation is another major concern with Si materials. With the large volume expansion, even if the NP does not breakapart, the lithium silicates do, leading to the repeated loss of SEI and continual consumption of Li to form a new SEI. There are several reported methods for addressing this issue. Creating an artificial SEI by grafting COOH with diazonium leads to more stable SEI [51]. The most effective method shown, however, is encapsulating Si in carbon to form a composite anode.

2.4 Composite Anodes

With the well established functionality of carbon based materials and the attractive high capacity of Si, the most promising route to high capacity anode materials may well be a composite structure. Reported designs of composite graphene and Si materials for Li-ion battery applications have followed 4 broad strategies. The simplest strategy, as one might expect, is merely to couple the nanoparticles to the surface of the graphene so they remain attached mechanically and electrically during battery cycling. The second strategy addresses the formation of an unstable SEI on the surface of the Si nanoparticles. This strategy involves encapsulating individual or groups of particles with some carbonaceous coating, be it amorphous or crystalline, so that a stable SEI layer is formed only with the carbonaceous material. The third strategy addresses the volume expansion of the Si nanoparticles in the material. By engineering vacancy into the material, there exists unoccupied space for the silicon to expand and fill. This has been shown to prevent the degradation of the material as well as the SEI layer due to Si volume expansion.

While these first three strategies involve making materials that are compatible with the current slurry coating methods employed in commercial batteries, the final one does not. The fourth strategy, which may contain elements of the first three, is to incorporate the materials into a free standing film that is both active material and current collector. This method allows for a significant reduction of mass by doing away entirely with the copper foil. This section summarizes published reports utilizing one of these four strategies, along with comments on the performance to give context to the work presented in this thesis.

2.4.1 Silicon Nanoparticles on Graphene Powders

Attachment of Si NP to graphene flakes allow the formation of simple, high capacity composite materials that are largely compatible with current production methods. The powders, like graphite or MCMB powders used in commercial battery production, can be mixed with binders and slurry coated to copper foil current collectors. Some strategies for making silicon coupled to graphene sheets have focused on attaching nanoparticles of Si to graphene oxide (GO). GO powder is available with small flake size, and is readily dispersible in various solvents, including water. The GO/SiNP material is then made conductive by removing the oxygen groups through chemical or thermal reduction [52][53].

Another route to the synthesis of Si NP attached graphene nano powders (GNP) is through the use of functionalized graphene flakes to promote ionic or covalent attachment [54]. This route does not require reduction to create a conductive material. Attachment of Si NP to GNP and the comparative performance of different attachment methods is the subject of work presented in chapter 4. Table 2.1 summarizes the performance of some reported anode materials that incorporate coupling Si nanoparticles to graphene powders.

Description	Reduction	Capacity	Rate	Ref.
TrGO/Si	500°C in Ar	$800 mAhg^{-1}$ @ 30 cycles	$300 mAg^{-1}$	[52]
TrGO/Si treated in HF	500°C in Ar	$1200 mAhg^{-1}$ @ 100 cycles	$200 mAg^{-1}$	[53]
GNP/Si covalently coupled	N/A	$830 mAhg^{-1}$ @ 50 cycles	$300 mAg^{-1}$	[54]
GNP/Si covalently coupled	N/A	$1200 mAhg^{-1}$ @ 50 cycles	$230 mAg^{-1}$	Chap. 4
TrGO/APS-Si	800°C in N_2	$800 mAhg^{-1}$ @ 100 cycles	$100 mAg^{-1}$	[55]
TrGO/Si covalently coupled	700°C in Ar	$800 mAhg^{-1}$ @ 50 cycles	$150 mAg^{-1}$	[56]

Table 2.1 Reported performance of coupled Si/Graphene composite powder anode material

2.4.2 Carbon Coated

Carbon coating Si nanoparticles allows carbon material to form a stable carbon based SEI on the surface of the nanoparticles. This SEI is more stable than an SEI formed with the Si resulting in less capacity fading. If the carbon material is soft, it can also act as a buffer to volume expansion. The most common route to producing carbon coated materials is by coating Si nanoparticles in a thin layer of hydrocarbon material such as pitch or some polymer, and then pyrolyzing the material to graphitize the coating. The resultant carbon coated powder is assembled into an anode using the standard method, mixing with binder and slurry coating copper foil.

Published reports describing the carbon coating universally find a benefit to encapsulation. Where uncoated Si nanoparticles lose their capacity rapidly, encapsulated Si anodes are able to retain high capacity at moderate to high charging rates. Table 2.2 lists several materials incorporating the coating of Si nanoparticles. The amount of Si by weight is the most important factor determining capacity. The poly(acrylonitrile) (PAN)

& poly(methacrylonitrile) PANM coated graphite encapsulation from Wang et. al. [57] has low Si content yet still maximizes the percentage of theoretical Si capacity used in the anode.

Coating	%Si	Capacity	Rate	Reference
Pitch carbon & graphite	31%	600mAhg^{-1} @ 23 cycles	160mAg^{-1}	[58]
carbon aerogel	60%	1450mAhg^{-1} @ 50 cycles	200mAg^{-1}	[59]
PAN & PANM coated graphite	22%	590mAhg^{-1} @ 45 cycles	160mAg^{-1}	[57]
PZS polymer	78%	1200mAhg^{-1} @ 40 cycles	600mAg^{-1}	[60]
PAN polymer	76%	1550mAhg^{-1} @120 cycles	200mAg^{-1}	[61]

Table 2.2 Reported performance of coated pyrolyzed Si/C composite powder anode material

2.4.3 Engineered Vacancy

A recent development in the design of Si based anode materials is the idea of engineering vacancy in the coated material to better facilitate the volumetric expansion of Si, while still providing the advantages of a carbon based outer layer for the formation of a stable SEI. Liu et. al. describe a high capacity fast charging material created by first oxidizing a thick layer of SiOx on the surface of the nanoparticles [62]. The oxidized particles are then coated and the SiOx is removed by etching with Hydrofluoric Acid. The resultant material is describes as having a "yolk-shell" structure, and has an initial capacity of 3500mAhg^{-1} and a measured capacity of 1500mAhg^{-1} after 1000 cycles at 4.2 Ag^{-1}.

A similar structure was reported by Luo et. al. where Si nanoparticles were atomized along with GO in a tube furnace [63]. The particles are wrapped in a crumpled graphene sheets, which are reduced by the high temperatures in the furnace. The crumpled graphene wrapped Si nanoparticles contain 60% Si and have a capacity of 950mAhg^{-1} after 250 cycles at 1000mAg^{-1} .

Zhao et. al. demonstrate a different strategy to engineer vacancy for Si expansion [64].

They utilize a wet chemical etching technique to make nanoporous Si from Si wafers before pulverizing the wafer into 3-10μm sized particles. The vacancy in the Si powder allows for the expansion of the Si material without the destructive expansion of the microparticle. A carbon coating on the particles allows for the formation of a stable SEI layer. Anodes made from porous carbon coated Si microparticles show no capacity fading when cycled at a capacity of 1500mAhg^{-1} for 50 cycles. The exceptional performance of these materials demonstrates the benefit of accommodating the Si expansion with some vacancy, as well as the need for providing a carbon based interface with the electrolyte.

2.4.4 Freestanding Films

All of the strategies previously discussed offer methods to improve the gravimetric capacity of the anode materials, but as shown in Fig. 1.5, a large fraction of the mass of an anode, 50-60%, consists of the binder and copper foil, not the active material. A sufficiently conductive and strong freestanding film of active material could act also as the current collector, while possibly not requiring any additional binder material. For freestanding films to make effective alternatives to the slurry coated anodes widely used today they must achieve comparable conductivity and mechanical stability. However, the typical method of measuring only the active material gravimetric capacity does not allow for direct comparison between slurry coated anodes and free standing films. When comparing the gravimetric capacity of a freestanding film, one must keep this in mind. Doing away with the copper foil and binder materials implies that a freestanding film with the same capacity actually has approximately twice the total effective gravimetric capacity as that quoted for a slurry coated active material.

Graphite foil, while strong and conductive, lacks the large edge area of graphitic powders, hindering the diffusion of Li ions into the material. Yazici et. al tested freestanding graphite foils and measured gravimetric capacity of only 50mAhg^{-1} [65] even at low current density. Because the Li mobility is largely in plane, a uniform layered structure is not optimal for maximizing capacity. Cross-plane Li mobility is essential in freestanding graphitic films [66]. Defects in the carbon lattice can contribute significantly to basal plane Li conductivity [67], and can be introduced by chemical oxidation [68] or photo-thermal (flash) reduction of a graphene oxide films [69].

2.4.5 Freestanding Composite Films

While freestanding carbon based anode films could alleviate the need for a metallic current collector, the inclusion of higher capacity active materials could further increase the capacity of anodes well beyond that for graphitic materials. The addition of silicon nanoparticles has synergistic effect of opening space in the structure which both allows faster Li diffusion, and leaves vacancy for Si NP expansion. Si NPs are trapped in the structure which promotes stable SEI formation with the carbon instead of unstable SEI formation with the silicon. Wang et. al report a freestanding graphene paper film incorporating 25% by weight Si NP. Their film is produced by the filtration of Graphene Oxide mixed with Si NP through a PVDF Membrane filter and is reduced chemically with hydrazine vapour. The freestanding anode showed 800mAhg^{-1} after 100 cycles at 50mAg^{-1} [70]. Lee et. al. achieved a much higher loading of 60% Si NP, with a film reduced thermally in Argon at 700°C . They note the film had poor mechanical stability but a high initial capacity of 2500mAhg^{-1} with a capacity of 1500mAhg^{-1} after 300 cycles using a charge rate of 100mAg^{-1} [71]. They test additional materials as well but use a different method for charging and discharging that make comparison to other materials difficult. Tao et. al. used a similar procedure for the production of a freestanding film 66% Si by weight and report capacity of 1000mAhg^{-1} after 30 cycles at 50mAg^{-1} [72]. In chapter 5 of this work a flash reduced freestanding composite anode is described with a capacity of 600mAhg^{-1} for 200 cycles at 50mAg^{-1} .

Reduction	%Si	Capacity	Rate	Reference
Hydrazine	25%	800mAhg^{-1} @ 200 cycles	50mAg^{-1}	[70]
700°C in Ar	60%	1500mAhg^{-1} @ 300 cycles	100mAg^{-1}	[71]
700°C in Ar	60%	1000mAhg^{-1} @ 30 cycles	50mAg^{-1}	[72]
Flash	60%	600mAhg^{-1} @ 200 cycles	50mAg^{-1}	Chap. 5

Table 2.3 Reported performance of freestanding composite films

2.4.6 Summary

Carbon based anodes are the current standard in Li ion batteries, but have gravimetric capacities limited to around 372 mAhg^{-1}. Silicon materials have been shown to offer a significant improvement in gravimetric capacity, however the volume expansion and unstable SEI formation make silicon anodes challenging to engineer. Nanostructured Si and graphene composite materials offer a very promising route to overcoming the issues of Si anodes, allowing the production of anodes with far higher capacity than currently available. The specific nanostructure of the materials is a key factor in performance. Materials that protect the Si from direct contact with the electrolyte while also providing a mechanism for the volume expansion of Si have the best performance reported in the literature. The expense and energy costs of producing these materials could be a significant factor. Chapter 5 of this thesis is a report on freestanding composite films made with the photo-thermal reduction method. This is a low energy synthesis method providing both SEI protection and volume expansion mitigation.

Chapter 3

Experimental Methods

3.1 Introduction

This chapter describes briefly the analysis and measurement techniques used in this work. Forming a complete picture of the function and performance of an electrode active material requires a variety of material science analysis techniques. To analyze, predict, and tune the performance of an electrode material it is necessary to have an accurate understanding of the physical and chemical structure of the material.

3.2 Micro Structural Analysis

Visualizing the structure of a nano-composite material requires the use of high resolution electron imaging techniques. The two most effective instruments to image materials with electrons are the scanning electron microscope (SEM) and the transmission electron microscope (TEM).

3.2.1 Electron Microscopy

The scanning electron microscope (SEM) is a standard instrument for visualizing the surface of materials with sub micron (typically 1-10nm) resolution. SEM is primarily a surface imaging technique, but can also be used for elemental analysis by detecting backscattered electrons which interact more strongly with elements with higher atomic numbers, or by analyzing the energy spectrum of x-rays produced by the interaction of the electron beam and the sample. Energy Dispersive X-ray (EDX) spectroscopy can give an elemental analysis of the surface of a sample. SEM analysis in this work was performed with a 15kV Hitachi SU70 and a 30kV Jeol JSM-7600F.

The transmission electron microscope (TEM) is similar to the SEM but operates at higher potentials, typically 100-300kV, and detects electrons transmitted through the sample instead of scattered at the surface. TEM is capable of directly imaging the atomic structure of crystalline and amorphous materials. By detecting the diffracted electrons from a crystalline sample, the precise crystal structure and atomic spacing can be determined. TEM analysis in this work was performed on a Philips CM200 TEM operated at 200 kV.

3.3 Thermal and Mechanical Analysis

3.3.1 Thermogravimetric Analysis

Thermogravimetric Analysis (TGA) is an analysis technique that allows a quantitative estimation of the composition of a composite material. By heating a sample of material to a high temperature at a controlled rate under a flow of inert gas while concurrently measuring the mass, the thermal decomposition of a material can be studied in detail. TGA requires very accurate measurements of mass and temperature. If the approximate composition of a material is known, and the thermal decomposition process for a given material is well understood, the mass loss at different temperature ranges can give quantitative measures of the relative mass of component materials. TGA analysis in this work was performed on a Q500 from TA Instruments. The temperature for all measurements was ramped at 20°C /m to 900°C under ambient conditions with a 40 ml/m flow of N_2 gas.

3.3.2 Tensile Strength

The tensile strength of a material is determined by measuring a force F applied to a sample of cross-sectional area A. The tensile stress $\sigma = F/A$ of material at breaking is the tensile strength. The measurement is taken while simultaneously measuring the strain ϵ given by the percent displacement $l_0/\Delta l$ for a given force. The Young's modulus E is an important mechanical property of a material and is given by $E = \sigma/\epsilon$. A sample of material should be cut into a dog bone shape, with a narrow channel between two anchoring sections of material. A sample of uniform width would have the highest stress where clamped to the measurement apparatus. For a sample with the dog bone shape the forces are strongest in the narrow channel, and the material should yield in the channel, giving an accurate measure of strength without the problem of clamping induced stress.

3.4 Spectroscopic Characterization

3.4.1 Confocal Raman Spectroscopy

Raman spectroscopy is a nonlinear optical technique using the inelastic scattering of a monochromatic laser source involving the emission (Stokes) or absorption (anti-Stokes) of phonons in a material. Raman is a particularly powerful technique for characterizing sp2 carbon materials such as graphite and graphene [73]. The experimentally accessible Raman scattering cross-section of graphene is large, as a result of resonant enhancement of Raman scattering and a strongly suppressed luminescence. The spectral signatures of sp2 carbons are well characterized. Shown in figure 3.1 is an example Raman spectrum for a single layer of graphene CVD grown on Cu and transferred to a SiOx on Si substrate. Table 3.1 summarizes the spectral features seen in graphene, graphene oxide and graphite. The G peak at 1585cm^{-1} and G$'$ peak at 2700cm^{-1} are characteristic of sp2 hybridized carbon. The D peak at 1350cm^{-1} arises due to disorder in the carbon lattice due point defects and edges. The response is generally strong enough to produce both overtones and mixing frequencies.

Name	ω (cm^{-1})	$\partial\omega/\partial E$ (cm^{-1}/eV)	Notes
D	1350	53	activated by disorder
G	1585	0	sp^2 Raman signature
D$'$	1620	10	activated by disorder
G*	2450	-10	sp^2 Raman signature
G$'$	2700	100	sp^2 Raman signature
G+D	2935	50	mixing mode
D+D$'$	2970	60	mixing mode
2G	3170	0	overtone of G
G+D$'$	3205	10	mixing mode
G$''$	3240	20	sp^2 Raman signature
$E_{laser} = 2.41$eV			

Table 3.1 Table of common features in Raman spectroscopy for planer sp2 carbon materials. Additional features are found when performing Raman on nanotubes and buckyballs. Adapted from [73]

3.4.2 X-ray Photoelectron Spectroscopy

X-ray Photoelectron Spectroscopy (XPS) is a surface analysis technique which used high energy X-ray photons to probe the electronic structure of atoms in the surface of a solid material. When bombarded with high energy X-rays, electrons from the inner orbitals of

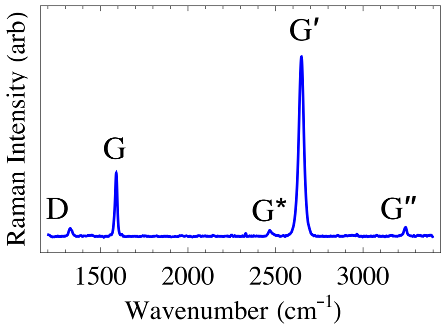

Fig. 3.1 Example Raman spectrum for a graphene material, in this case a single layer of graphene grown on copper foil with chemical vapour deposition.

the atoms are ejected. An analysis of the number of electrons ejected vs. their energy gives an XPS spectrum. Photoelectron energy E_k is a function of the energy of the X-ray photon $h\nu$, with a shift from the binding energy of the electron E_b and the work function ϕ of the spectrometer.

$$E_k = h\nu - E_b - \phi \tag{3.1}$$

Because the binding energy E_b is a function of the electronic structure of the atoms, XPS can be used to identify the elements present in a sample. The binding energy is, to a smaller extent, affected by the chemical bonds to an atom. The slight measurable shift in energy can thus identify to what other atomic species an atom is bonded. A database of binding energies for different elements and chemical bonds is referenced to determine the species present in the sample. The probability of an ejected photoelectron interacting with the material is very high, so the technique only probes the first few nm of the surface. XPS in this work was performed on a K Alpha from Thermo Scientific with an Al Kα X-ray source (1486.6 eV). The C1s peak was calibrated to 284.4 eV.

3.5 Electrochemical Characterization

3.5.1 Sheet Resistance

Sheet resistance is the preferred method of characterizing the resistivity of thin films where the thickness in negligible or difficult to determine, and is measured with a 4-point Van der Pauw technique [74]. The technique relies on measuring the resistivity of a sample in two orthogonal directions, R_V and R_H. Solving the van der Pauw formula

$$e^{-\pi R_V/R_S} + e^{-\pi R_H/R_S} = 1 \tag{3.2}$$

gives a measurement of the sheet resistance R_S. The resistance measured is independent of the shape and area of the sample as long as the measurement probes are close to the edge of the sample. The van der Pauw technique gives a sheet resistance measured in $\Omega/\square$. By multiplying by the thickness of the sample, the resistivity ρ of a material can be calculated. For a isotropic symmetrical sample where $R_V = R_H$, the van der Pauw equation simplifies to $R_S = \frac{\pi R}{\ln 2}$.

3.5.2 Half Cell Testing

The performance of a Li-ion battery depends both on the characteristics of both the cathode and anode. In order to isolate and test the performance of the anode, the anode is assembled into a battery against a reference Li metal electrode. The anode material is used as the positive electrode as shown in Fig. 3.2. Li ions can be transfered to the anode material by connecting an external current path, allowing the electrochemical reaction to proceed.

Charging the cell with an external power source runs the reaction in reverse, removing Li ions from the anode material. Assembling the battery in this fashion allows measuring most of the significant parameters of an anode material: the gravimetric and volumetric capacity, Coulombic efficiency, charge and discharge voltage profiles, differential capacity (dQ/dV), rate capability and electrochemical impedance.

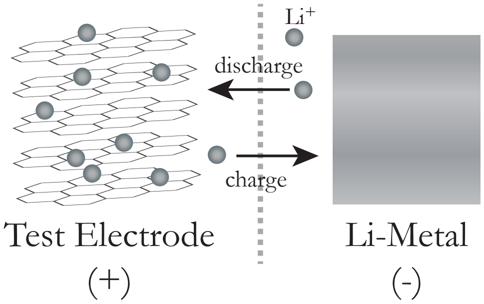

Fig. 3.2 Schematic of the transport of Li ions in a half cell test. Li-ions are moved in and out of the test electrode against a reference electrode of Li metal.

The test cell is assembled in a standard CR2032 coin cell with component parts as shown in Fig. 3.3. Assembly of the battery must be performed in an anaerobic glove box to ensure an oxygen and moisture free environment. The components are placed in the cell casing and a liquid electrolyte is added. The cell is hermetically sealed using an automated pressing machine. Once assembled, the cell can then be transfered out of the glove box for further testing.

3.5.3 Galvanostatic Charge and Discharge Testing

In Galvanostatic cycle testing, the half cell is charged and discharged repeatedly with a constant current source. In order to gain an accurate accounting of the charges entering and exiting the material under test, the current must be precisely controlled and the voltage

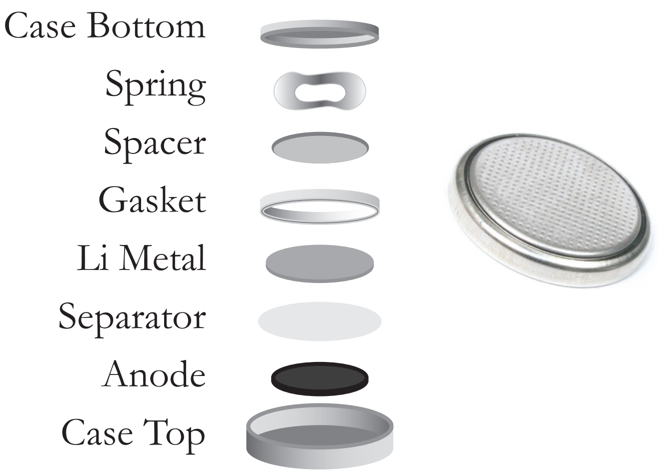

Fig. 3.3 Schematic of the components of the CR2032 coin cell package used to test anode materials in a half cell.

accurately measured. The circuit diagrams for charging and discharging a battery and half cell are shown in Fig. 3.4. In a full cell during discharging, current flows from the cathode to the anode as Li ions move from the anode to the cathode. This is flipped in the half cell test where the anode material is acting as the cathode against a Li metal anode. For an ideal battery the voltage measured during discharge will not change until the cell is fully depleted.

The voltage profile for the first five cycles of a typical half cell test is shown in Fig. 3.5. The initial cycle is done slowly in order to form a stable SEI. A well formed SEI will stabalize the capacity and improve the lifetime and efficiency of the battery.

3.5.4 Capacity fading and Coulombic Efficiency

The capacity in each cycle and Coulombic efficiency are two critical measurements of battery performance. For each cycle of the battery, the current delivered to or from the battery is measured and integrated. Plotting the capacity vs. cycle number gives a good indication of battery performance over time. A good battery material will lose very little capacity

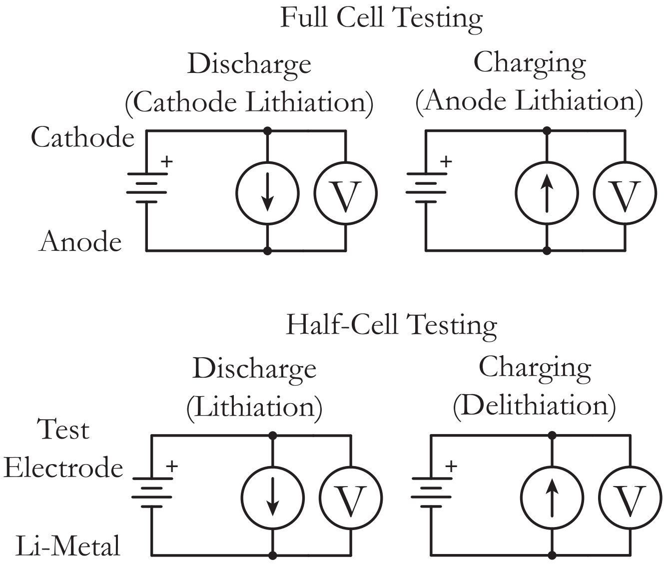

Fig. 3.4 Schematic showing the direction of electrical current used to charge and discharge full and half cells and the nodes at which the cell voltage is measured.

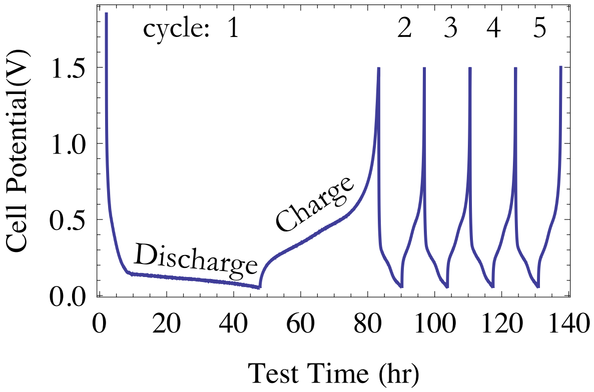

Fig. 3.5 Plot of cell voltage versus time for five cycles of a typical galvanostatic charge/discharge test. Generally a cell would be tested for a few hundred cycles.

from cycle to cycle, and the efficiency in this case will be close to 100%.

3.5.5 Charge/Discharge Capacity Profile

The charge and discharge capacity profile curves plot the cell voltage against the integrated current, or capacity. The curve gives a measure of the potential as it changes with the insertion of Li ions. The difference in end points of the curves of consecutive cycles display the loss in capacity. When used in a full cell test, the charge/discharge curve gives the open circuit voltage for at different states of charge. A typical capacity profile graph is shown in Fig. 3.7. This plot shows the first three charge/discharge cycles of a galvanostatic test of a Li-ion half cell.

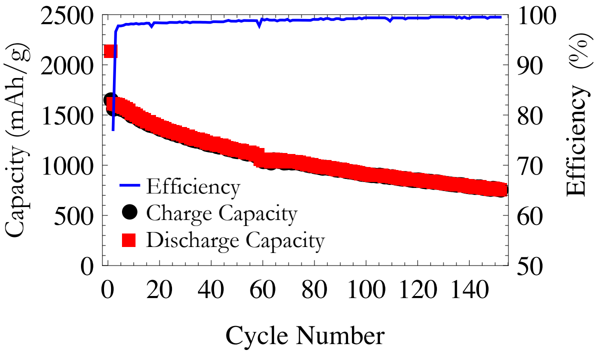

Fig. 3.6 Plot of charge and discharge capacities versus cycle number. The right axis shows the Coulombic efficiency at each cycle.

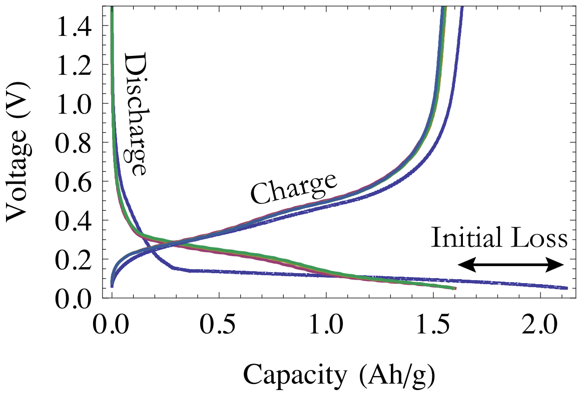

Fig. 3.7 Plot of voltage capacity profile for the initial three cycles of a battery. Often plots such as this do not indicate the exact cycle number because it can be inferred where in the cycling the curve is from by observing the upper limit of capacity and comparing it to the plot of charge discharge capacities vs cycle number.

3.5.6 Differential Capacity Analysis

Differential capacity analysis is done by finding the derivative of the charge and discharge capacity profiles. By performing this analysis we can find at what potentials Li ions are forming compounds with the anode material. Particularly for Si anodes, this information can allow the determination of the stoichiometry of the alloys being formed. A typical differential capacity profile is shown in Fig. 3.8.

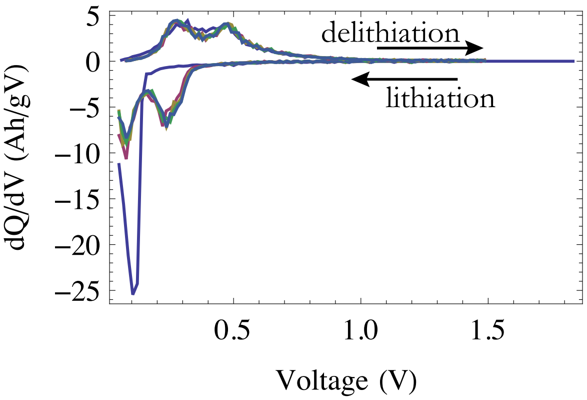

Fig. 3.8 Plot of the differential capacity, dQ/dV. This plot is derived from the derivative of the charge/discharge capacity profile and is useful for visualizing the potentials associated with significant ion transport into the test electrode.

Chapter 4

Coupled Graphene Powder and Si Nanoparticle Composite Anodes

4.1 Introduction

The inclusion of Si as a high capacity active material in Li-ion battery anodes presents significant benefits in terms of both gravimetric and volumetric capacity. The theoretical specific capacity of Si is 4400mAhg^{-1} , more than 10 times that of the graphitic materials commonly used today, and has a low lithiation potential (<0.5 V vs Li/Li^{+}) allowing higher cell voltages than other high capacity materials.

The use of Si as a Li storage material also presents significant challenges. The volumetric expansion that Si undergoes upon lithiation is one of the largest barriers to the use of Si materials in Li-ion battery anodes. The 300% volume change upon full lithiation causes pulverization of the Si materials. Bulk Si, thin Si films, and micro scale Si particles all suffer from disintegration upon repeated charge/discharge cycles. Only nanoscale Si materials, such as Si nanowires or Si nanoparticles can withstand repeated cycling and volume expansion without harmful material degradation.

Anodes comprised solely of Si nanomaterials tend to have poor cycle lives. Nanomaterials have a high surface area to volume ratio. The high surface area results in the production of large amounts of SEI. With Si materials, during repeated cycling and volume expansion, the SEI breaks away, exposing new surface to form more SEI in the subsequent cycle. In addition, particles can break away and become electrically isolated. These isolated particles can no longer participate in the electrochemical reaction. The effect of continuous SEI formation and particle isolation is rapid capacity fading and low Coulombic efficiency.

One potential strategy to mitigate the volume expansion of Si materials is the inclusion of Si NP in a conductive matrix of carbon materials. This matrix provides electrical pathways for current collection, and buffers the volume expansion of the Si NP. Additionally, the SEI formed with carbon materials is more stable than that formed with Si. Preventing formation of Si SEI by instead forming SEI with carbon materials stabilizes the capacity of the anode. Graphene sheets provide a promising host material for the inclusion of Si NP. Si NP can be attached directly to the surface of graphene flakes through various means forming a high capacity composite material compatible with commercial anode production methods.

The method of attaching Si NP to the surface of graphene flakes has a large effect on the ultimate anode performance. This chapter investigates three methods for coupling nanoparticles to the surface of graphene flakes. Physical coupling (mixing), ionic coupling, and covalent coupling as shown in Fig. 4.1 are all potential routes to the production of composite materials. Each strategy represents trade-offs in ease of production, chemical compatibility and performance. The strategies employed to attach materials are kept as similar as possible to facilitate direct comparisons of the coupling strategies.

There is very little macroscopic difference between these methods, each produced a pow-

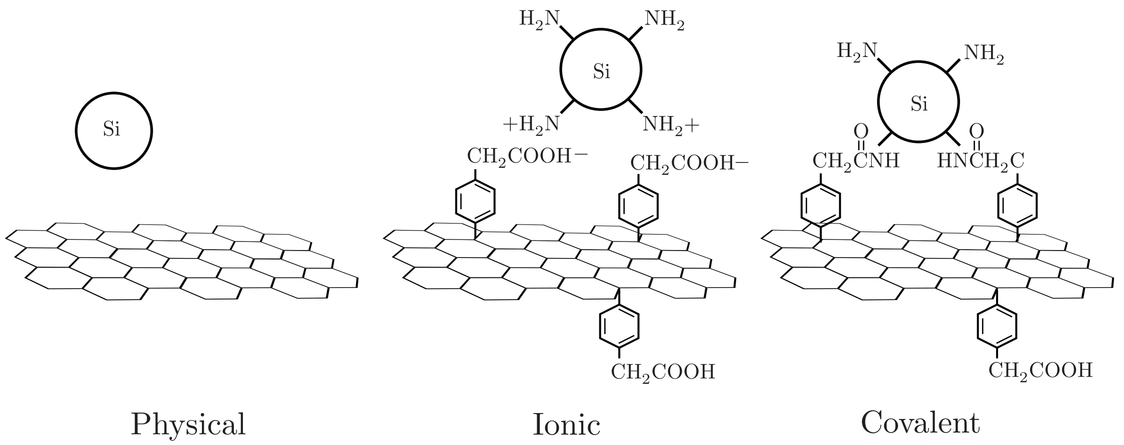

Fig. 4.1 Schematic of the coupling strategies employed in the Si graphene composite anode materials in this chapter.

dered composite that is compatible with current slurry coating methods for the production of anodes. The three different composite materials are tested as slurry coated electrodes on a copper current collector in a half cell and compared to a slurry coated Si NP electrode. All of the anodes tested had higher initial capacity than commercially available graphitic materials. The covalently coupled material has less capacity fading and superior gravimetric capacity after 100 cycles. This result suggests that covalently coupling is the best strategy for attaching Si NP to graphene in composite battery anode applications.

4.2 Physical Coupling Graphene to Si NP

The creation of a functional physically coupled Si NP and graphene composite material requires the selection of component materials suitable for inclusion in Li-ion battery anodes. The carbon material must be highly conductive and contain few impurities that could contribute to reduced conductivity and undesired chemical reactions that would consume excess lithium and degrade the performance. The Si NP material must have an appropriate particle size for best performance.

4.2.1 Graphene Nanopowder

Graphene nanopowder (GNP) is an ultrafine black powder of conductive graphene flakes with high carbon content (97%) and with low oxygen (<2.5%) and hydrogen content (<2%). The high surface area (400-800 m^2g^{-1}) is ideal for maximizing the functional groups available for attaching nanoparticles. A high density of surface functional groups is important to facilitate good coupling for ionically and covalently coupled materials. An SEM image of the GNP used to create composite materials is shown in Fig. 4.2.

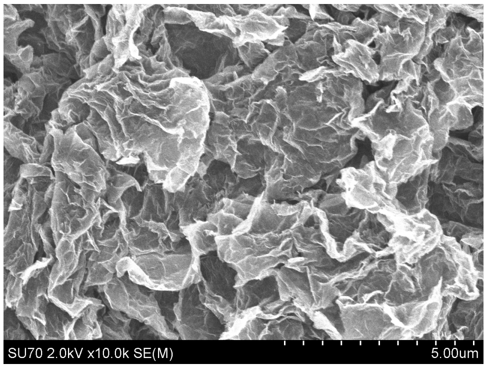

Fig. 4.2 SEM micrograph of the GNP material used for the production of composite materials. The manufacturer specifies that the typical flake size is 10μm with an average thickness of 3 layers (1.6nm).

4.2.2 Silicon Nanoparticles

Si NP can be formed by purely physical means from Si wafers by laser ablation or ball milling. Chemical and electrochemical etching of Si wafers can also be used to form Si NP. Chemical synthesis can be achieved using silane gas or silicon halides in solution as precursors. These methods produce smaller Si NP <10nm [75]. The size of Si NP used in preparation of composite materials is critical to the long term performance of the anode.

Si NP less than 150nm do not experience fracture upon lithiation [76]. The Si NP used for production of composite materials in this work were sourced from Alfa Aesar. The manufacturer specifies the crystalline particles were plasma synthesized and had a typical diameter of approximately 100nm. These claims were not independently verified. An SEM image of the Si NP used is shown in Fig. 4.3 and a TEM image of a crystalline NP is shown in 4.8. While the Si NP used were crystalline, ultimately during cycling the structure is reorganized by repeated lithiation and delithiation, and in the battery anode all the crystalline nanoparticles become amorphous, so ultimately the crystallinity of the precursor NP is not an important factor in anode performance.

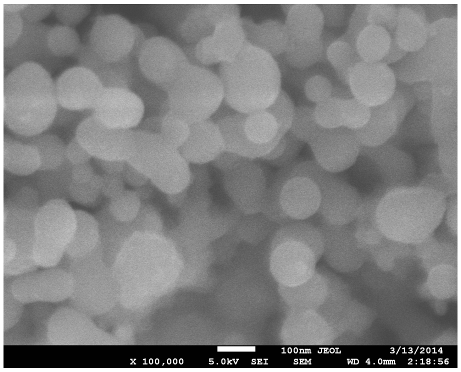

Fig. 4.3 SEM micrograph of the Si NP used for production of composite materials. The manufacturers specified size of the Si NP is approximately 100nm

A sample of physically coupled composite Si/GNP material was prepared by adding weighed quantities of both Si and GNP to ethanol and dispersing in an ultrasonic bath. The mixture was stirred with a magnetic stirrer for 48h to facilitate uniform mixing. The resulting composite was dried in reduced pressure and kept in a sealed container until it was used to prepare the anode slurry.

4.3 Ionic Coupling Graphene to Si NP

Forming an ionic coupling between the Si NP and the graphene flakes requires the modification of the surface charge state of the component materials. Opposite charge must be established on the surface of each material to promote electrostatic attachment. A simple route to accomplish this is the functionalization of the surfaces with groups that maintain opposite charges in an aqueous solution with controlled pH. To perform the attachment of functional groups, two different chemistries are used. Diazonium chemistry is used to attach functional groups to a graphitic surface, and silane chemistry is used to attach functional groups to the native silicon oxide layer of Si NP. The surface charge after functionalization in solutions of varying pH is found by measuring the ζ-potential.

4.3.1 Surface Attachment of Functional Groups

The pristine surface of a graphitic material is stable and typically does not allow chemical bonding without modification. The surface must be modified to add functional groups in order to attach molecules. Common methods for the modification of graphitic surfaces include the use of strong acids and high temperatures to induce oxidation, providing various oxygen containing functional groups including carboxylic and hydroxylic groups to facilitate further chemical modification. The level of oxidation and the specific groups introduced are difficult to control using these methods. Diazonium chemistry can be used to functionalize the graphitic surface with specific groups. The variety of specific functional groups that may be attached for later reactions is determined by the selection of diazonium salts[77, 78].

Functionalizing a graphitic surface introduces point defects where the functional groups are attached. These defects appear in the Raman spectrum as disorder related spectral features. To characterize the density of functional groups attainable on a graphitic surface,

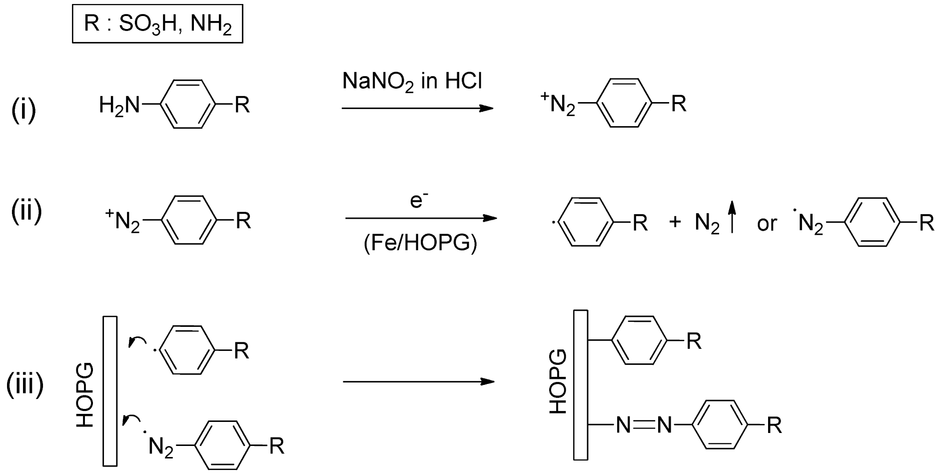

Fig. 4.4 Reactions performed to attach functionalized phenyl groups to a graphitic surface. Adapted from [79]

a pristine sample of HOPG was functionalized using diazonium chemistry with sulfophenyl (S-HOPG) and aminophenyl (A-HOPG) groups. Fig. 4.5 shows the Raman spectrum of an HOPG surface before and after functionalization. The density of functional groups can be estimated by comparing the ratio of the integrated intensity of the D peak to that of the G peak by using an empirical model from [73]. When the defect density is low ($< 10^{12}\text{cm}^2$), the model for the average distance between defects L_D is given by solving:

$$\frac{I_D}{I_G} = \frac{(102 \pm 2)\text{nm}^2}{L_D^2} \tag{4.1}$$

Where I_D and I_G are the intensity of the D and G peaks in the Raman spectrum. The defect density can be inferred from L_D. The density of functional groups for functionalized A-HOPG was estimated to be $5 \times 10^{10}\text{cm}^{-2}$ while S-HOPG had an estimated density of $2 \times 10^{11}\text{cm}^{-2}$. Because HOPG is the least reactive of the graphitic materials, we anticipate greater coverage of phenyl groups on graphitic materials with a higher initial defect density like GNPs.

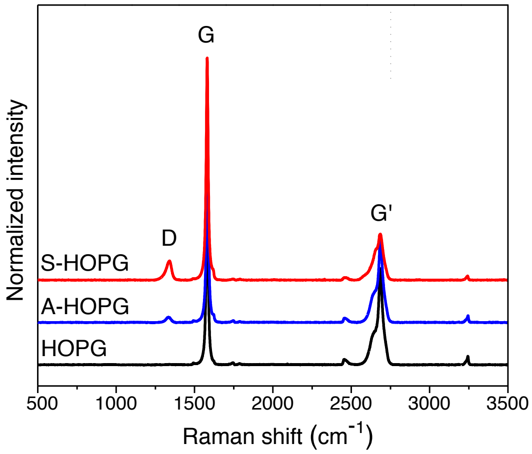

Fig. 4.5 Raman on HOPG before and after functionalization with diazonium chemistry. Adapted from [79]

The density of defects generated by functionalization is relatively uniform. Fig. 4.6 shows measurements of D to G ratio before and after the functionalization of a pristine HOPG surface with sulfophenyl groups.

4.3.2 Design of Ionically Coupled Anode Material

To facilitate the ionic attachment of Si NP to functionalized graphene, the surface of Si NP was aminated using anhydrous silane chemistry [55]. The presence of a native oxide on the surface of the NP allows this procedure to take place. The amination of Si NPs imparts a positive surface charge which will ionically couple with the negative charge of the COOH functional groups on the surface of the GNP.

4.3.3 Carboxylic Functionalization of Graphene through Diazonium Chemistry

Graphene nanopowder (AO-1 GNP, Graphene Supermarket) was used as a precursor material. The manufacturer specification indicates average flake size of 10μm and an average

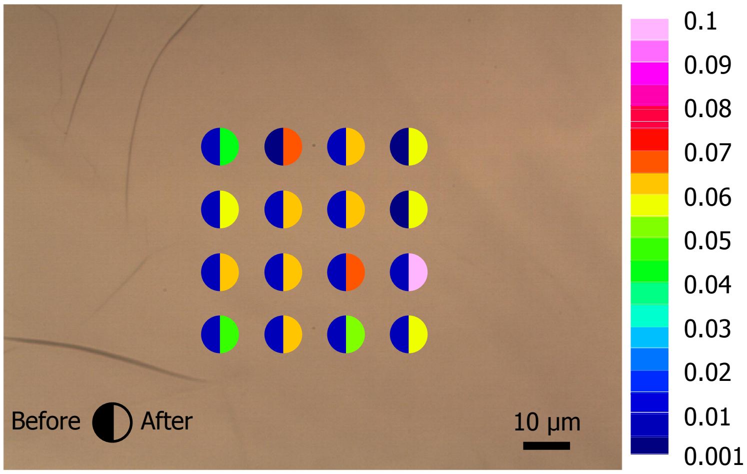

Fig. 4.6 Spatial map of the integrated Raman intensity ratio I_D/I_G before and after functionalization of HOPG surface with sulfophenyl groups. The intensity ration increases from 0.001 to a value 0.05-0.10. This corresponds to a defect density between 10^{10} and 10^{9} cm^{-2}. Reproduced from [79]

thickness of 1.6nm (<3 layers). Carboxylated GNP (COOH-GNP) was synthesized using diazonium chemistry by preparing a solution of 4-aminobenzene acetic acid (1.37 g, Sigma) and sodium nitrite (0.7 g, Sigma) in 0.5M hydrochloric acid (100 ml) to achieve a 0.1M concentration of the corresponding diazonium cations. Hypophosphorous acid (20ml, 50%) was added to the solution to reduce the diazonium cations to radicals. GNP (100 mg) was then dispersed in the solution with magnetic stirring for 2h to graft the radicals on its surface. Following functionalization, the COOH-GNP was collected using vacuum filtration and resuspended in DI water using an ultra-sonic bath. This process was repeated for 5 iterations to remove excess reactants.

4.3.4 Amino functionalization of Si NP through Silane Chemistry

Aminated Si NP (NH_2-Si) was synthesized by grafting amino groups to the surface of Si NPs using anhydrous silane chemistry. Si NP (average diameter 100 nm, Alfa Aesar) were exposed to air for several hours to ensure the formation of a native surface oxide layer. The oxidized Si NP (200 mg) were dispersed in toluene (10 mL) and (3-aminopropyl)trimethoxysilane (APS, 2mL, Aldrich) for 24h under magnetic stirring. N2 gas bubbles were introduced to provide protection. After, the Si NP were separated by centrifugation, washed with toluene and ethanol, and dried under reduced pressure. The modified Si NP was denoted as NH_2-Si.

4.3.5 ζ-Potential

A measurement of ζ-potential can confirm the surface charge of a material for a given pH of solution. Figure 4.7 shows ζ-potential measurements for the functionalized and unfunctionalized component materials of the composite anode material. This measurement allows the determination of a pH of solution that will promote ionic binding of Si-NP to the GNP. At pH levels where the surface charges are of opposite polarity, the Si-NP will be electrostatically attracted to and attach to the surface, forming the composite material.

For NH_2-Si the surface charge is positive in $pH < 7$, whereas without functionalization the native oxide provides a negative surface charge in this range of pH. The surface charge of COOH-GNP is negative for $pH > 3.5$ but for unfunctionalized GNP the surface charge becomes negative only above pH 7. A solution of pH 6 gives the largest potential difference (>50mV) to optimally promote electrostatic attraction. ζ-potential analysis of aqueous solutions was performed with a zeta sizer Nano ZS from Malvern Instruments.

4.3.6 Ionic coupling

A quantity of NH_2-Si was added to COOH-GNP dispersed in DI water using an ultrasonic bath and further mixed using magnetic stirring for 48h to ensure uniform mixing. The opposite surface charge of the materials in a neutral pH facilitated ionic coupling. The material was collected using vacuum filtration and was dried under reduced pressure. This

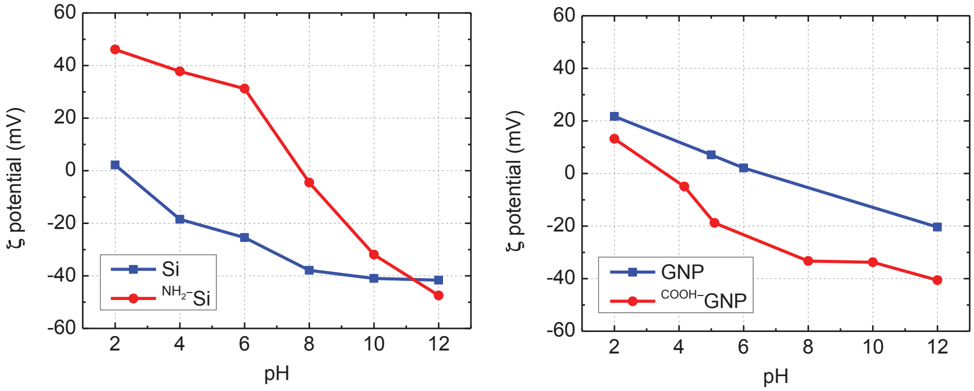

Fig. 4.7 (Left) ζ-potential measurements of Si NP and NH_2-Si. The amino groups on the surface make the surface charge positive. (Right) ζ-potential measurements of GNP and COOH-GNP. For a range of pH from 2 to 12, the ζpotential of COOH-GNP is more negative than GNP. This is expected due to the negatively charged carboxylic groups on the surface. Reproduced from [80].

material, denoted as NH_2-Si/ COOH-GNP, was stored in a desiccator until used.

4.4 Covalent Coupling Graphene to Si NP

Covalent bonding produces the strongest possible coupling between the Si NP and the GNP. This is done to reduce the detachment of Si NP during volume expansion when cycling. The coupling is accomplished by reacting functional groups on the surface of the constituent materials with a coupling agent to form a highly stable molecular link.

After the modification of the graphene surface with aminophenyl groups using diazonium chemistry, and modification of the Si oxide surface with amine groups using silane chemistry, the two functionalized materials were coupled using a carbodiimide coupling agent. N-(3-dimethylaminopropyl)-N'-ethylcarbodiimide hydrochloride (EDC) in the presence of N-hydroxysuccinimide (NHS) was used to couple NH_2-Si and COOH-GNP to form a composite Si-NHCO-GNP. In order to ensure only covalently coupled Si NP remained attached to the GNP, the material was washed, filtered, and resuspended in both neutral and basic aqueous solutions using ultrasonication.

4.5 Anode Material Characterization

4.5.1 Electron Microscopy

The morphology of the coupled Si/GNP materials was analyzed with SEM. The attachment of the particles on the graphene surface can be directly viewed, giving insight into the density of Si NP on the surface as well as the size distribution of Si NP after attachment. TEM was used to analyze the structure of the Si NP. Fig. 4.8 shows images of the materials under electron microscopy. SEM shows the wide coverage and close coupling of Si NPs on the GNP. TEM shows the crystalline nature of the Si NPs as well as the thin native oxide layer (1 - 2nm).

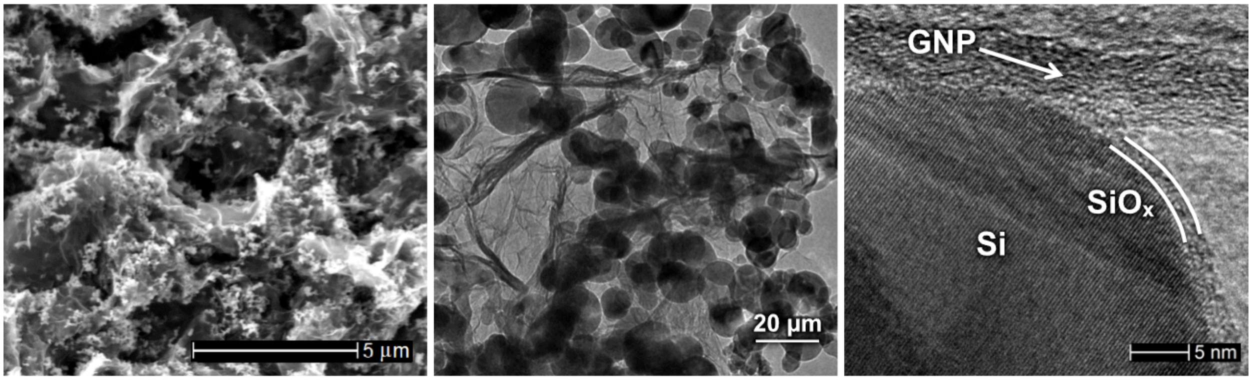

Fig. 4.8 Left: SEM image of covalently coupled material showing the coverage of Si NP (white). Center: TEM image of covalently couple material. Right: high resolution TEM showing crystalline Si NP with 2nm amorphous native oxide layer. Reproduced from [80].

4.5.2 TGA

Thermogravimetric analysis (TGA) was carried out on a Q500 (TA Instruments) at a heating rate of 20°C /min in air. TGA performed on NH_2-Si is shown in Fig. 4.9. Compared to unfuctionalized NP, the NH_2-Si sample loses mass at slightly elevated temperatures due to the removal of amino groups from the surface. Above 400°C thermal oxidation of the Si begins and the sample gains mass as oxygen from the environment reacts with the Si NPs.

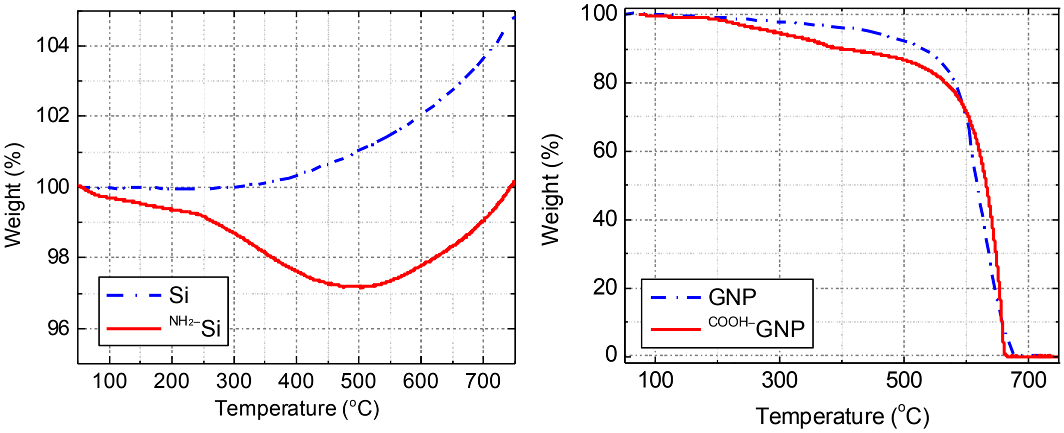

Fig. 4.9 Left: TGA in ambient conditions on SiNP and NH_2-Si. The amino groups are removed at lower temperatures leading to a loss in mass for the NH_2-Si sample. The increase of weight at higher temperatures is due to the thermal oxidation of the Si nanoparticles. Right: TGA in ambient conditions on COOH-GNP. The functional groups are removed from 200 to 400°C before the material completes burns away above 500°C. Reproduced from [80].

TGA on COOH-GNP in Fig. 4.10 similarly shows a reduction in mass as functional groups are removed at temperatures between 200 and 400 °C . The GNP material completely above 500°C .

To determine the theoretical capacity of the coupled materials, the percentage of Si by weight was determined by TGA. The weight of material remaining after GNP decomposition is entirely Si. TGA on Si/GNP, NH_2-Si/COOH-GNP, and Si-NHCO-GNP is shown in Fig. 4.10. TGA on all materials indicates the Si content above 60%. Si/GNP and

NH_2-Si/COOH-GNP contain slightly more Si, likely due to the extra steps used to remove non-covalently coupled Si NP from the Si-NHCO-GNP material. The representative TEM in 4.8 shows a 2nm oxide layer. We estimate the mass of native SiOx layer to be about 10% of the SiNP mass for a mean Si NP diameter of 100nm . Despite this significant contribution we neglect the oxide layer in further analysis. The theoretical capacity, $Q_{\text{theoretical}}$, is then:

$$Q_{\text{theoretical}} = \%\text{Si} \times 4200 + (1 - \%\text{Si}) \times 372 \text{ mAhg}^{-1} \tag{4.2}$$

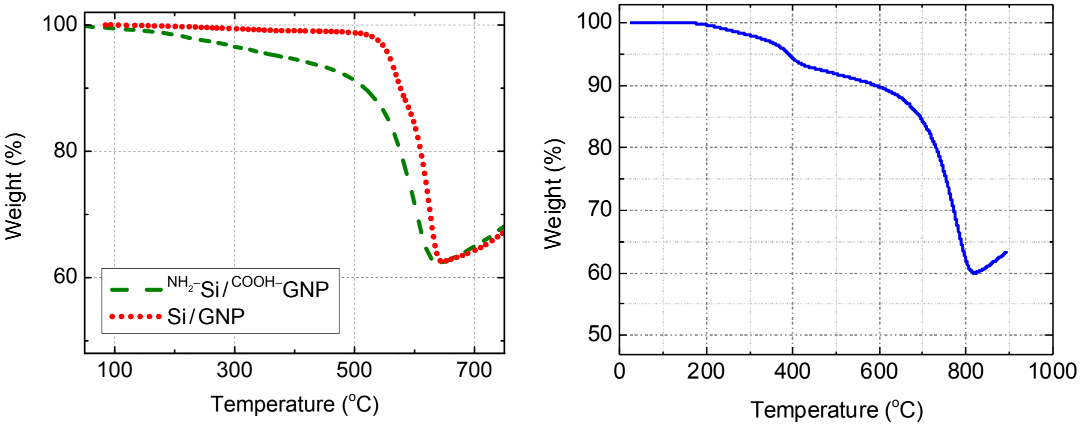

Fig. 4.10 Left: TGA on physically coupled Si/GNP and ionically coupled NH_2-Si/COOH-GNP materials. Right: TGA on Si-NHCO-GNP material. The analysis indicates that the Si content of all materials is around 60%. Reproduced from [80].

4.5.3 XPS

X–ray photoelectron spectroscopy (XPS) was performed on a monochromatic X-ray photoelectron spectrometer K-Alpha (Thermo Scientific), equipped with an Al Kα X-ray source (1486.6 eV). Survey scans and high resolution scans were collected with energy steps of 1 and 0.1 eV, respectively. The spectral energies were calibrated by setting the binding energy of the C 1s component corresponding to C=C bonds to 284.4 eV. XPS on the functionalized GNP materials shows the appearance of the O1s peak from the carboxyl croups on the surface as well as the appearance of the N1s peak due to the N=N bonds bridging the phenyl to the graphitic surface. XPS on Si NP shows the appearance of the N1s peak due to the amine functional groups on the surface. The appearance of the C1s peak in the functionalized Si NP is due to the APS alkyl chain. XPS spectra of COOH-GNP and NH_2-Si are shown in 4.11.

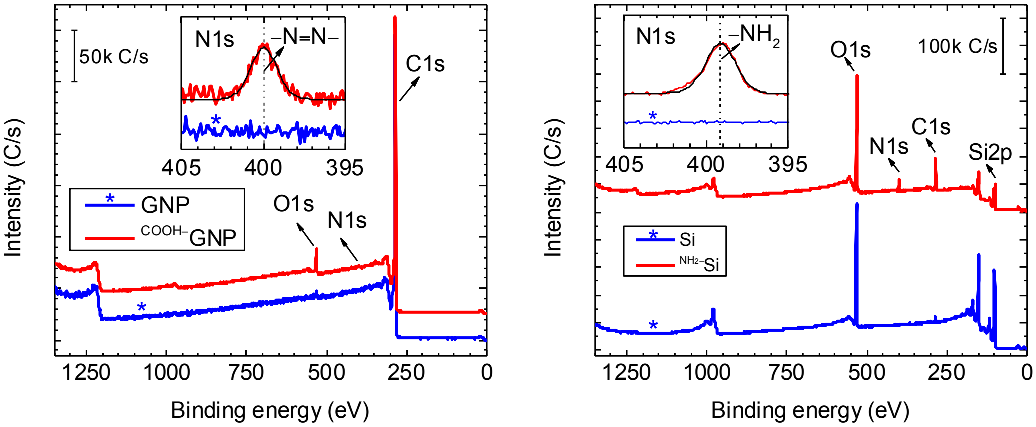

Fig. 4.11 Left: XPS on COOH-GNP including a high resolution inset of the nitrogen peak. The oxygen peak in the spectrum indicated the presence of oxygen groups on the surface. The N1S peak shown in the inset is due to the presence of N=N bonds in bridging the phenyl groups to the graphitic surface. Right: XPS on NH_2-Si including a high resolution inset of the N peak indicating the presence of NH_2 groups on the surface of the SiNP. Reproduced from [80].

4.6 Galvanostatic Cell Testing

4.6.1 Cell Production

The working anodes made of Si-NHCO-GNP, NH_2-Si/ COOH-GNP, Si/GNP, and bare Si NP were assembled by first creating a slurry of each material with sodium alginate as binder

(20% by weight). Carbon black (10% by weight) was also added to bare Si NP to improve the conductivity. Powders were dried in atmosphere at 80°C for 2 hours. Dried materials (40mg) were mixed with sodium alginate binder (10mg) and crushed repeatedly in a small mortar for 5-10m to mix thoroughly. 10-20 drops of water were added and mixed into the powder to create a spreadable ink.

Each slurry was coated on a 25μm Cu foil current collector with a Baker type cylindrical applicator set to 6 mil (250μm). The copper foil was then dried overnight in an oven at 120°C and the thickness of the active material after drying was measured with a micrometer to be 10μm -15μm . Discs 12mm in diameter were punched out of the anode foil and weighed on a digital microbalance to determine the weight of the active material and copper foil.

CR 2032 coin cells were fabricated in an Ar filled glove box with the working anodes and the Li metal as the reference and counter electrode. Each cell contained a microporous tri-layered polypropylene (PP) and polyethylene (PE) polymer membrane separator (Celgard, USA) and electrolyte fromed from a 1 M $LiPF_6$ solution of ethylene carbonate and dimethyl carbonate (1:1 volume ratio, Novolyte, USA). A schematic of the assembly is shown in 3.3.

4.6.2 Cell Testing

Assembled cells were allowed to sit for several hours in order to saturate the open circuit voltage. Galvanostatic charging and discharging was carried out for 100 cycles between 0.05 V and 1.5 V with a current density of 231 mAg^{-1} for Si–NHCO–GNP, NH_2–Si/COOH–GNP and Si/GNP, and 360 mAg^{-1} for Si, corresponding to C/10 rate based on the weight of the active materials.

4.7 Results

The specific charge capacity, discharge capacity, as well as Coulombic efficiency (C.E.) for the four anodes under test are shown in Fig. 4.12. A table summarizing the results for the first, second and hundredth cycle is shown in Table 4.1. The first discharge for all the cells is a formation cycle. The capacity is higher than subsequent cycles due to the formation of an SEI layer, where some of the Li is consumed and does not participate in the following charge cycle. The capacity regained during the first charge cycle is the usable capacity in the electrode, this represents the amount of Li that can participate in subsequent cycles. Capacity retention (C.R.) is defined as the capacity retained in subsequent charge cycles from the initial charge cycle. All of the materials tested had similar first cycle discharge capacity.

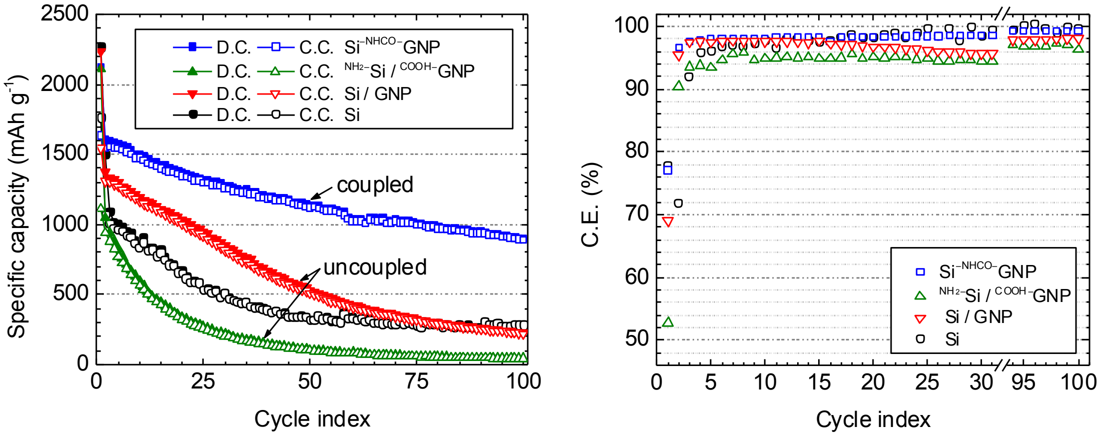

Fig. 4.12 Left: Specific capacity for 100 discharge and charing cycles for covalently, ionically and physically coupled composite material as well as reference Si NP material anodes. Right: Coulombic efficiency of the tested anodes for 100 cycles. Reproduced from [80].

There are two primary processes causing the loss of capacity after the initial formation of SEI, however other loss processes are possible through parasitic reactions that consume Li. During the discharge cycles, if the previous SEI layer is broken due to the expansion of the Si materials, the unprotected surface is exposed. More SEI will form consuming additional Li and reducing the C.E. of the cycle. During the charge cycles, the volume of the Si material is contracting as Li is pulled out of the material. If some Si NP become electrically isolated from the rest of the anode, they will no longer provide storage on subsequent cycles, reducing both the C.E. and the discharge capacity of the next cycle.

4.7.1 Si NP

The first cycle discharge capacity for the bare Si NP anode was 2260mAhg^{-1} , and it retained 1760mAhg^{-1} upon charging. The C.E. of the first cycle was 77.8%. As more SEI is formed, the C.E. should improve, yet the second cycle efficiency for Si is reduced, 71.7%. By the 4th cycle the C.E. improves to above 95%. The capacity of the Si anode steadily decreased, and stabilized after about 50 cycles to around 300mAhg^{-1} , less than the theoretical capacity of commercially available carbon anodes. After 100 cycles, the Si anode retained less than 16% of the initial charge capacity.

4.7.2 Si/GNP

The mixed Si/GNP anode material had an initial discharge capacity of 2237mAhg^{-1} and an initial charge capacity of 1543mAhg^{-1} . The material maintained higher capacity than the Si anode for more than 75 cycles. The second cycle C.E. was above 95%. The benefit of adding graphitic materials to buffer volume expansion and form stable SEI is clear. However, repeated cycling eventually reduced the capacity below that of the Si anode. The Si/GNP retained only 14.4% of the initial charge capacity after 100 cycles, demonstrating the importance of coupling for longer term performance.

4.7.3 NH_2-Si/COOH-GNP

The ionically coupled NH_2-Si/COOH-GNP had the lowest first cycle C.E. (52.7%) of all the materials. It is likely that the ionic coupling was weakened by the strong charge screening of the conductive electrolyte and additional electrochemical reactions occurred with the free functional groups on the surface of the component materials. The overall result was a rapid loss of capacity, and the material retained less than 4% of the initial charge capacity after 100 cycles.

4.7.4 Si-NHCO-GNP

The covalently coupled Si-NHCO-GNP material had a first cycle efficiency of 77%, and an initial charge capacity of 1635mAhg^{-1} comparable to the Si material. However the second cycle efficiency was far higher than that of Si, approaching 95%. The capacity fading was lower than all other materials in the comparison and by 100 cycles the material maintained nearly 900mAhg^{-1} of capacity, 55% of the initial charge capacity.

4.8 Discussion

This chapter demonstrated a route to synthesize coupled Si and graphene composite materials for Li-ion battery anodes. Silane and diazonium chemistries were utilized to achieve the functionalization of component materials and the covalent coupling of functionalized materials was achieved using a carbodiimide coupling agent. This is the first direct comparison of different coupling strategies without significant differences in composite material composition. Covalent coupling was found to be superior to both ionic coupling and simple mixing in stabilizing the performance of Si NP attached graphene materials in Li-ion battery anodes.

	Discharge $mAhg^{-1}$	Charge $mAhg^{-1}$	C.E. %	C.R. %
	Cycle #1			
Si	2262.3	1759.7	77.8	
Si-NHCO-GNP	2120.9	1634.5	77.1	
NH_2-Si/COOH-GNP	2111.5	1112.0	52.7	
Si/GNP	2236.5	1542.9	69.0	
	Cycle #2			
Si	1491.1	1069.7	71.7	60.8
Si-NHCO-GNP	1600.5	1546.2	96.6	94.6
NH_2-Si/COOH-GNP	1043.3	943.0	90.4	84.8
Si/GNP	1369.9	1307.2	95.4	84.7
	Cycle #100			
Si	279.3	278.2	99.6	15.8
Si-NHCO-GNP	897.6	891.0	99.3	54.5
NH_2-Si/COOH-GNP	44.7	43.1	96.3	3.9
Si/GNP	226.0	221.5	98.0	14.4

Table 4.1 Table of capacities, Coulombic efficiency, and capacity retention for the first, second and 100th cycle of the Si NP anode and composite anodes synthesized using different coupling methods.

By producing three composite materials with nearly identical formulations, and comparing them to a simple Si NP based anode, two important results are clearly shown. First, The inclusion of significant amounts of GNP material serves to stabilize the initial cycles of the composite material, improving the C.E. for the first cycles by buffering the volume expansion and allowing the formation of stabilizing SEI with the carbon materials. This effect is seen even for the simple case of mixing Si NP with graphene powders, with no additional treatment. Second, the covalent coupling of Si NP to GNP creates a more stable material, with less capacity fading than a simple mixture. The capacity of this material after 50 cycles is 1200mAhg^{-1} , higher than previously reported for a covalently coupled Si NP/graphene material [54], and after 100 cycles is almost 2.5× higher than carbon based commercial anode materials.

The ionic bonding of Si NP to GNP is not sufficient to ensure good long term performance. In fact, the ionically coupled material demonstrated very poor performance—far worse than even the simple mixed Si/GNP material. It is likely that there were unforeseen interactions between the functional groups on the materials and the chemistry in the cell, which degrade the performance of the material. Further study is needed to fully characterize this effect.

In the next chapter, a similar ionic coupling technique is used in a process to create layered Si and graphene oxide composite material., In this process, however, further steps remove the functional groups from the graphene oxide material and a similar degradation of performance is not observed.

Chapter 5

Flash Reduced Freestanding Layered Graphene/Silicon Nano-composite

5.1 Introduction

This chapter describes a novel method of producing a class of self-assembled composite materials that have the potential to be cost-effective high capacity Li-ion battery anodes. A lightweight flash reduced GO thin film current collector is integrated with a high capacity film of encapsulated Si NP. The resulting two-layered structure forms a single self-supporting, conductive anode film with improved gravimetric capacity over traditional carbon anode materials.

In a typical Li-ion battery manufactured for EV applications, the copper current collector constitutes nearly half of the mass of the anode system and more than 10% of the total mass of the battery [15]. The copper used in anodes as a current collector and substrate for slurry coating of carbon active materials provides no Li storage capacity. When researchers report the gravimetric capacity of an electrode, they usually report the capacity of the material only, and not the entire electrode. A freestanding electrode, one capable of performing the dual functions of Li storage and current collection, is therefore not directly comparable to traditional slurry coated materials. Nontheless, it is informative to compare gravimetric capacity, keeping in mind a freestanding film has a significant advantage without the heavy metallic substrate.

	Percent Mass		
Component	HEV	PHEV	EV
$LiMn_2O_4$	27.0	28.0	33.0
Graphite	12.0	12.0	15.0
Binder	2.1	2.1	2.5
Copper	13.0	15.0	11.0
Aluminum	24.0	23.0	19.0
$LiPF_6$	1.5	1.7	1.8
EC	4.4	4.9	5.3
DMC	4.4	4.9	5.3
PP	2.0	2.2	1.7
PE	0.26	0.40	0.29
PET	2.2	1.7	1.2
Steel	2.8	1.9	1.4
Thermal Insulation	0.43	0.33	0.34
Glycol	2.3	1.3	1.0
Electronic Parts	1.5	0.9	1.1

Table 5.1 Table of the relative mass of components of typical electric vehicle batteries.

Carbon films formed from CNTs [81, 82, 83] or graphitic materials [65, 84, 85] can perform the same function as metallic current collectors while also providing a maximum theoretical 372mAhg^{-1} of Li-ion storage capacity. Incorporating high capacity active lithium storage materials into the conductive carbon film can further improve the gravimetric capacity of the freestanding composite anode for Li-ion batteries. In addition, a properly designed coupling between the high capacity material and the carbon material can eliminate the need for non-conductive binder materials, further improving gravimetric capacity.

The challenge in designing a composite film is to create an appropriate micro structure to function well as a battery anode. The structure must allow conduction of both electrons and Li-ions. There is typically a trade off between surface area, which provides high ionic conductivity into the material, and initial capacity loss. Materials with high surface area tend to have more SEI formation, which can consume Li and cause a low initial Coulombic efficiency and capacity fading.

SEI formed with graphitic materials is generally stable and well understood [86]. SEI formation with other materials may not be as stable, and with Si especially is decidedly unstable [87]. When incorporating Si NP into a composite anode, it is highly beneficial to encapsulate the Si in layers of carbon, allowing the SEI to form only with the carbon and protecting the Si surface from direct contact with the electrolyte.

The structure must also accommodate the physical changes of the active materials. For an all carbon anode, this change is small, and almost negligible. For materials containing Si, however, the volume expansion upon lithiation is >400%. Accommodating this expansion is critical to the long term cycleability of the electrode.

5.2 Production of Freestanding GO Paper

The main precursor material to the freestanding composite anode is GO. The production of stable GO paper films is an essential step in the synthesis of graphene/Si NP composite anode materials. This section describes the properties of GO and the processes used to produce freestanding GO papers.

GO is a oxidized form of graphene, containing numerous surface functional groups. The basic structure is shown in figure 5.1. GO is produced by the extreme oxidation and exfoliation of graphite into graphite oxide and then into atomically thin sheets with sizes up to several μm using H_2SO_4, $K_2S_2O_8$ and P_2O_5. The oxidation results in functionalization of the surface with hydroxyl, and epoxide groups and some edges with carbonyl and carboxyl groups [88]. The process to produce graphite oxide was developed by Hummers and Offeman in 1958 [25] as a large scale industrial process. A modified process suitable for small scale production of GO was published by Kovtyukhova et. al.[89] in 1998. Aqueous GO suspensions are currently commercially available.

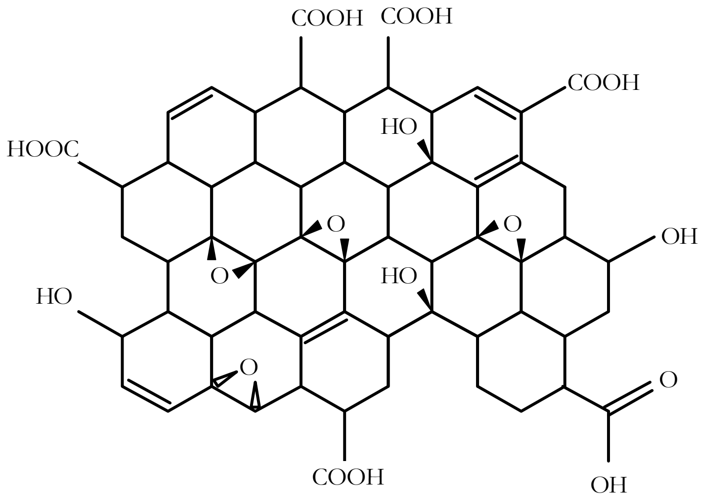

Fig. 5.1 Schematic of the general structure of GO. The surface contains both epoxide and hydroxyl groups, while the edges are terminated with carbonyl and carboxyl groups.

GO paper is a capable precursor for high strength, flexible films because of its compatibility with aqueous chemistry and the multitude of routes for reduction into conductive reduced graphene oxide (rGO) paper. GO paper can be readily produced in two principle ways: from an aqueous suspension of GO by vacuum filtration [26, 90], or by drop casting and subsequent evaporation of water [91].

Vacuum filtration of GO is common in the literature, however, the directed flow of vacuum filtration requires many hours of active pumping through expensive alumina filters, and is not actually critical to the formation of layered graphene oxide papers. Additionally, the alumina filters typically used to produce GO paper films introduce Al-ion contamination that could potentially affect the electrochemical performance of the anode [92].

A graphene oxide suspension left to evaporate will self assemble into a continuous, uniform film of overlapping sheets. This method of drop-casting and evaporation is passive, requiring no energy to pump, and can be done with inexpensive, commercially available polymer substrates. The key to the production of uniform GO paper using this method is the behaviour of the substrate surface. On a suitably hydrophilic polymer substrate, GO will spread evenly, forming an almost uniform film after evaporation. Dura-lar textured polyester films (Grafix), is an ideal substrate for the production of GO paper using the evaporation method. Passive evaporation of the water from a GO suspension also allows the production of GO paper with arbitrary size and shape as determined by the substrate used. The thickness of the film can be easily controlled by changing the volume or concentration of the GO suspension.

5.3 Reduction of GO Paper

The reduction of GO is the second essential step in the production of graphene/Si NP composite anode materials. Reduction removes the oxygen from the GO paper, returning it to a conductive form capable of performing the dual function of Li ion storage and current collection. This section describes the method used to create an electrically conductive freestanding graphene film from GO paper.

Several methods have been reported for directly creating or transforming GO paper into conductive graphene films. Chemical reduction can be performed before [93], or after [94, 85] the GO paper film is formed. Thermal reduction can also be performed after the film is formed [71, 72]. Photo-thermal reduction of GO paper films can be accomplished using using both flash lamps and lasers [69].

Thermal reduction of GO paper occurs above 250°C in air. The transformation to rGO requires only a few minutes above this temperature. Figure 5.2 shows the resistance of samples vs. temperature. Samples were placed in a furnace set for different temperatures and held at the temperature for 10 min. The sheet resistance of each sample was then measured with a 4-point probe using the van der Pauw technique. The resistance of thermally reduced samples drops nearly four orders of magnitude. The surface of the reduced samples becomes shiny and metallic as shown in the centre of figure 5.3 compared to the translucent brown colour of the unreduced sample.

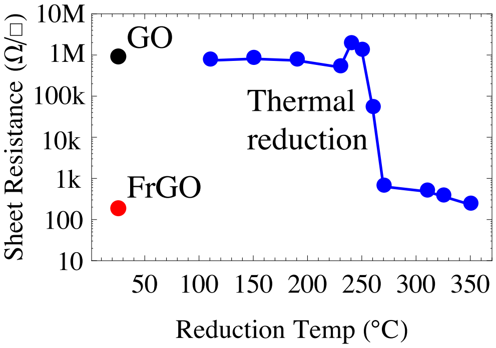

Fig. 5.2 Sheet resistance of GO, FrGO and TrGO plotted vs. reduction temperature. The temperature at which the resistance drops is consistent with the temperature of reduction indicated by TGA. Flash reduction is capable of producing films with sheet resistance similar to thermal reduction at 350°C

Photo-thermal or flash reduction is a violent reaction; the reduction products and adsorbed water are rapidly ejected from the material causing cracks and pores to appear in the reduced paper anode [95, 96]. The result is a porous 3D structure that can allow electrolyte permeation and faster Li migration into the material. An image of a flash reduced sample is shown in the right of figure 5.3.

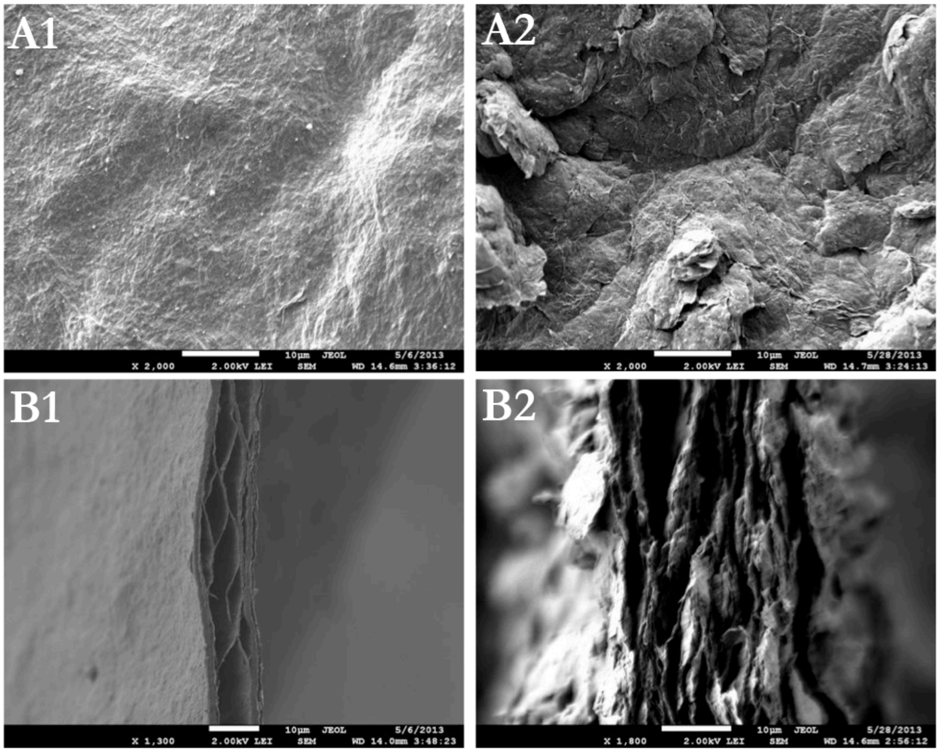

Fig. 5.3 The surface of TrGO (A1) shows fewer cracks than that of FrGO (A2). The side profile of TrGO (B1) shows a dense layer stacking compared to the loose stacking of FrGO (B2).

5.4 Design of Freestanding Anode

The design of this novel material was developed after an extensive review of literature on Si and Si/graphene composite anode materials. The main goals of the material design were:

1. To form a freestanding conducting graphene film capable of performing the dual task of Li-ion storage and current collection.

2. To achieve higher capacity by inclusion of Si NP materials.
3. To encapsulate and immobilize Si NPs in order to mitigate formation of SEI layers with Si.
4. To create an open structure to facilitate electrolyte penetration and better Li intercalation dynamics by using a photothermal reduction process.
5. To achieve simple self assembly of the structure from commercially obtainable materials requiring only minor preparation.

In order to achieve these goals, the self assembly mechanism for GO paper was employed. A base layer of purely graphene was used to improve the mechanical stability and as a conductive current collector. Si NP were attached to the flakes before assembly of a second layer and became encapsulated between sheets of GO, giving protection from SEI formation and vacant space for expansion. This was accomplished using a passive evaporation self-assembly technique. The whole structure was flash reduced to introduce pores and cracks while making the film conductive. Fig. 5.4 shows a schematic of the side view of this material.

5.5 Material Production

The production of layered films was a multi-step process that first requires the formation of a base film consisting of only GO. Following this, a mixture of Si NP and GO was produced with a method that couples the NP to the surface of the GO flakes. These Si NP attached GO flakes were then added as a second layer to the base GO layer. These flakes self assembled into a laminar structure, and the film, once made, was reduced.

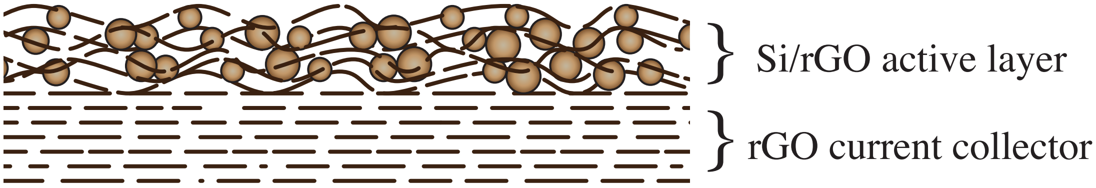

Fig. 5.4 Schematic of the layered anode material. The base layer was a well ordered rGO substrate that supplies both electrical conductivity and some small Li storage capacity. The second layer was an active layer consisting of high capacity rGO encapsulated Si NP. The Si NP was embedded in the material to promote formation of an SEI layer with the carbon only. Flash reduction opened cracks and defects promoting ionic conductivity between basel planes.

5.5.1 Graphene Oxide Films

Single-layered films of GO were produced from an aqueous GO suspension commercially available from Graphene Supermarket (Ultra HC, 6 mg ml^{-1}). The suspension, as received, was sonicated for 1h prior to coating the textured polyester film with an approximate GO areal gravimetric density of 1.25 mg cm^{-2}. After spreading the suspension evenly over the substrate, the water was allowed to evaporate for 24 h to 48 h in a desiccator, producing a continuous film of GO paper. When dry, the film was carefully peeled from the substrate and stored in the desiccator until further use.

5.5.2 Production of Si/GO composite suspension

In order to facilitate the binding of Si NP to the GO sheets, the surface was functionalized with (3-aminopropyl) trimethoxysilane (APS), which gave the Si NP a positive surface charge that attracted to the negative surface charge of the GO. Si NP powder with average diameter of 100 nm was purchased from Alfa Aesar. The Si NP were exposed to air for several hours to ensure the formation of a native oxide. The oxidized Si NPs (200 mg) were dispersed in toluene (10 mL) and APS (2 mL, Aldrich) with N_2 as a protective gas for

24 h while stirring. The APS-Si was then separated through centrifugation, washed with toluene and ethanol, dried, and stored until further use.

APS-Si was added to deionized water (6 mg ml^{-1}) and sonicated for 1 h to evenly disperse the particles and reduce conglomeration. This sonicated APS-Si was added in equal amounts to a GO suspension and sonicated for an additional 1 h to facilitate mixing. The mixture of materials formed a stable suspension that appeared a uniform opaque light brown.

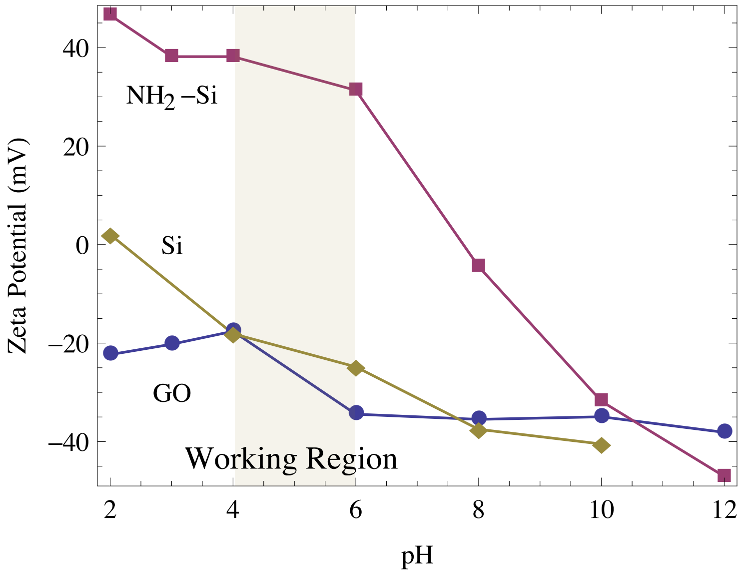

Fig. 5.5 Zeta potential measurement for GO and APS-Si. In low pH solutions, functionalization of the Si NP with APS gives the particles a positive surface charge and promotes electrostatic attraction to the GO surface. Ionic assembly occurs most efficiently between pH 4 and pH 6.

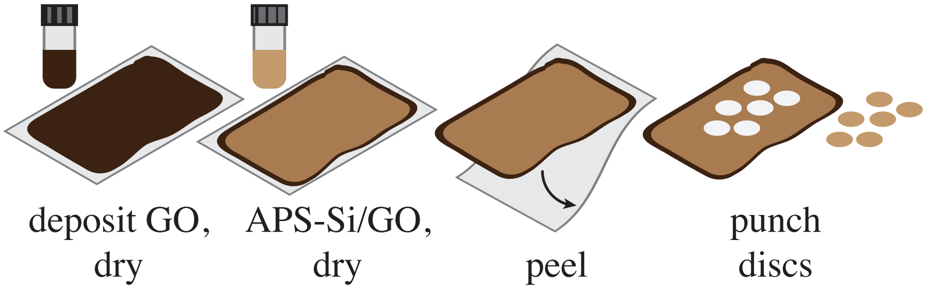

Fig. 5.6 Schematic of the steps to produce layered GO and Si/GO anode discs prior to reduction. First, GO was deposited and dried on a polymer substrate. Next, a layer of functionalized APS-Si NP mixed with GO was deposited and dried. Finally, the dried film was peeled from the substrate and cut into discs for later reduction and characterization.

5.5.3 Production of Layered Composite Anode Films

The procedure for producing the double-layered film is described in Fig. 5.6. A layer of pure GO paper was produced and dried as before using the evaporation method. Then, an additional layer of a ionically coupled Si/GO composite material was added and dried as before. Once dry, the film could be carefully peeled from the polymer substrate and stored in a desiccator for future use. After removal from the substrate, the freestanding film could be reduced by chemical, thermal or photo-thermal means. The layering process was required to improve the Si percentage by weight. If a layering process is not used, films disintegrate while drying, as shown in the left of Fig. 5.7. An image of a dried layered composite film is shown in the right of Fig. 5.7.

5.5.4 Reduction of Anode Films

The punched anode discs can be reduced by any of the methods used to reduce GO films. A flash lamp was used to initiate a photo-thermal process to reduce the films violently, opening cracks and pores in the material that facilitated electrolyte penetration. The discs were placed Si side up 2-3 cm below a flash lamp (B400, Paul C. Buff) and repeatedly subjected

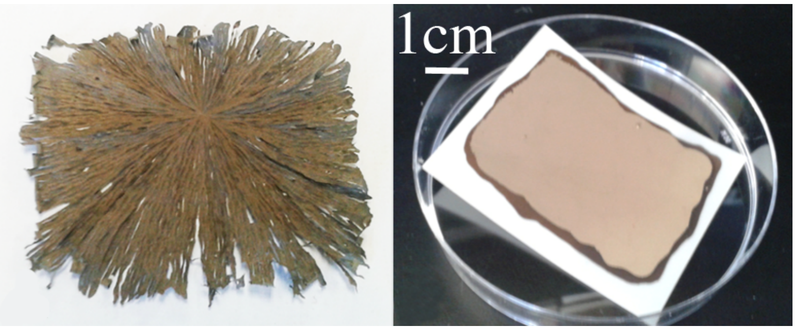

Fig. 5.7 (Left) Image of a single layer of composite material dried on polyester substrate. The addition of Si NP resulted in the film disintegrating when drying. (Right) A successful multi layered composite GO and Si/GO paper film on polyester substrate. The Si percentage by weight was found to be the same (60%) in both films.

to 500 μs flash with 160 J energy until the reaction occurred, typically this required 5 flashes. The same procedure was used for the FrGO comparison samples. Figure 5.8 shows an image demonstrating the macroscopic appearance of the flash reduction method compared to thermal reduction. The black surface of the FrGO sample indicates the severe level of damage to the film compared to thermal reduction.

Fig. 5.8 Image of the effect of different reductions methods. Thermal reduction creates a shiny metallic surface with far fewer defects than the flash reduced film which resembles a piece of ash

5.6 Material Characterization

5.6.1 SEM

The micro structural properties of the layered anode films were visualized by imaging of the surface and profile using an electron microscope. Scanning electron microscopy was performed on a Jeol JSM7600F at an acceleration voltage of 5kV. To image the cross section of the materials, samples were carefully cut with a razor blade to produce a clean edge. Figure 5.9A shows SEM images of the profile of the FrGO sample, demonstrating the expanded structure as compared to a thermally reduced GO sample (TrGO, reduction temperature of 350°C) in Figure 5.9B. The double-layered micro-structure and the nano-structure of FrGO/Si is shown in Figure 5.9C and a detail of the silicon nanoparticles embedded between layers of reduced GO in the Si rich layer is shown in Figure 5.9D. An image of the surface of FrGO/Si (Figure 5.9E) shows the Si nanoparticles sized 100 ± 50nm both atop and embedded into the anode material. Figure 5.9F shows cracks on surface of the FrGO/Si material due to the flash reduction.

5.6.2 Raman Spectroscopy

The Raman spectrum of graphene is well studied [73]. The G peak is a single phonon resonance that indicates the presence of hexagonal (sp2) carbon. The G' peak is also characteristic of sp2 carbon. The D peak and D' peak appear because defects in the lattice and grain boundaries break the symmetry of the hexagonal lattice. The ratio of the D peak to the G peak can be used to estimate the density of defects in the material. Higher order harmonic mixing occurs giving rise to G+D and G+D' peaks.

The functional groups on GO are photo luminescent, and re-emit a broad spectrum of photons. Photoluminescence is present in the GO samples but is suppressed by the

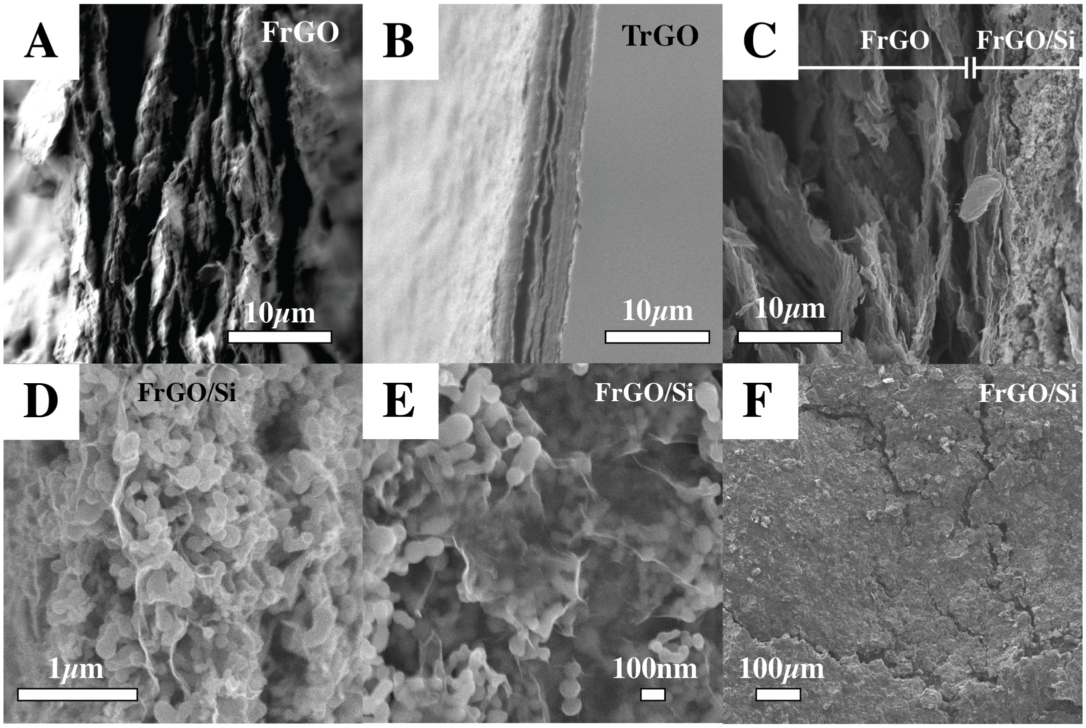

Fig. 5.9 SEM micrographs of side profiles of (A) FrGO, showing the expanded structure, (B) TrGO showing the dense layered structure, (C) FrGO/Si showing the double layered structure, and (D) a higher magnification of the active region showing APS-Si encapsulated between layers of FrGO. (E) The top surface of FrGO/Si showing APS-Si with size 100±50 nm encapsulated in the material. At a 5 kV acceleration voltage, the electron penetration depth was sufficient to see many layers below the surface. (F) The top surface of FrGO/Si showing cracks induced by the flash reduction.

conductivity of the rGO samples. The D peak does not get smaller with reduction because reduction does not substantively repair the lattice. Reduction products during photothermal reduction include the carbon compounds CO and CO_2, and usually leave behind vacancies in the lattice [97]. Raman can also be used to verify the structure of Si NP, as crystalline Si will have sharp peaks at 520cm^{-1}, but amorphous Si has a broad spectrum. The atomic structure of the material was not probed with XPS or TEM because the thickness of the final composite material makes these techniques less useful.

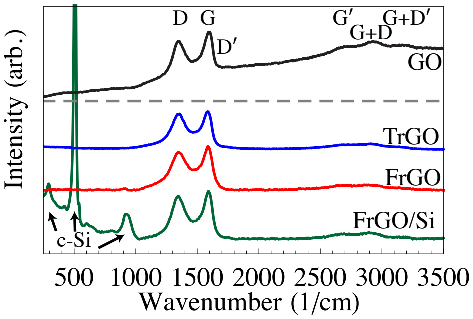

Fig. 5.10 Raman spectra of GO (black), TrGO (blue), FrGO (red), and FrGO/Si (green). The spectrum of the Si rich reduced GO layer shows crystalline Si peaks at 520cm^{-1} from the APS-Si.

5.6.3 Thermo-Gravimetric Analysis

TGA was used to determine the Si content of composite anode materials. As a sample is heated to high temperature in atmospheric conditions, carbon material will oxidize and burn away above 600°C leaving behind only Si. The percentage of mass remaining after the carbon has burned away indicates the weight percentage of Si in the anode which can be used to calculate a theoretical capacity for the material. Above 600°C the Si begins to oxidize, gaining mass.

In addition to determining the weight percentage of Si in a sample, TGA can also be used to observe the reduction of GO, and confirm that rGO materials are fully reduced, as partially reduced samples will still exhibit weight loss from the ejection of reduction products.

Figure 5.11 shows the TGA of GO, FrGO, TrGO, and FrGO/Si films in a dry air environment. The GO first lost adsorbed water (region I), then reduced, thereby ejecting a significant amount of CO and CO_2 (region II). The lack of mass loss for the FrGO in regions I and II indicated that the flash reduction was nearly complete and equivalent to TrGO, reduced at 350°C . Above 500°C , the carbon content of the material underwent oxidative decomposition (region III). The remaining mass of the FrGO/Si sample following decomposition contained Si and Si oxides and was at most 60% percent Si by weight, giving an approximate maximum theoretical capacity of $2600 \mathrm{mAhg}^{-1}$, taking into account a capacity for graphene of $372 \mathrm{mAhg}^{-1}$ and for Si of $4200 \mathrm{mAhg}^{-1}$.

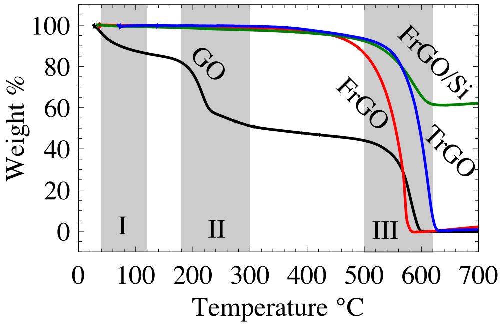

Fig. 5.11 TGA curves of GO (black), FrGO (red), TrGO (blue), and the FrGO/Si (green) composite material. There was no additional weight loss for the FrGO, and FrGO/Si samples in the drying region (I) and the reduction region (II) indicated the flash reduction was complete. TGA indicated the layered composite after carbon decomposition (region III) was 60% Si content by weight.

5.6.4 Sheet Resistance

The conductivity of the anode film is critical to the performance of the battery. To gauge the effect of flash reduction on the conductivity of anodes as compared to thermal reduction, an experiment was performed comparing the sheet resistance measured on films reduced at different temperatures. Sheet resistance is a more consistent measurement when comparing materials where the thickness is changing through the process. Discs of GO were punched and heated in a furnace. The reduction temperature was increased for each sample and a van Der Pauw measurement was taken with a four point probe. The results are summarized in Fig. 5.2. The resistance dropped four orders of magnitude by 350°C . The temperature where the resistance drops was consistent with the thermal reduction temperature found with TGA. The flash reduction process produced a film sheet conductivity on par with thermal reduction in air at 350°C .

5.7 Cell Production and Testing

5.7.1 Coin Cell Fabrication

Anodes were assembled in a nitrogen glove box into a CR2032 coin cell with a Li metal counter electrode. A 1M $LiPF_6$ solution in equal parts ethyl carbonate (EC) and dimethyl carbonate (DMC) was used as the electrolyte. For samples containing Si, fluoroethylene carbonate (FEC) was added (10% by weight) to stabilize the capacity [98, 99]. A microporous tri-layered polypropylene (PP) and polyethylene (PE) polymer membrane (Celgard) was used as the separator. Due to the fragility of the FrGO/Si sample, care was required while handling the film before assembly. However the high pressure used to compress the components of the battery together stabilized the material within the cell.

5.7.2 Half Cell Testing

The assembled cells were allowed to rest until the open circuit voltage stabilized. The cells then were subject to galvanostatic cycling on an Arbin BT2000 battery tester. Initially, cells were subject to a formation cycle from their open circuit voltage to 0.05V and back to 1.5V. The cycling was then repeated in the 0.05V to 1.5V window. The FrGO anode was cycled at 40mAg^{-1} for 100 cycles (C/10) for a total test time of 35 days. The APS-Si anode was cycled with a formation cycle of 70mAg^{-1} (C/50) and then at 360mAg^{-1} (C/10) for 200 cycles for a total test time of 17 days. The FrGO/Si anode was first cycled with a formation cycle at 40mAg^{-1} (C/50) and then at 200mAg^{-1} (C/10) for 200 cycles for a total test time of 50 days. The slow cycle rate of the materials was chosen to probe the gravimetric charge capacity with minimal impact from kinetic effects such as the dynamic cell impedance.

5.8 Results

The primary concern in the evaluation of the performance of the anode materials is the amount of specific capacity they contain following the formation of an SEI, and how much capacity they retain after repeated cycling. In addition to specific capacity, analyzing differential capacity can give insight into the formation of SEI layers and the specific electrochemical reactions occurring during each cycle.

5.8.1 Battery Cycle Performance

The discharge (lithiation) capacity of the FrGO, Si and FrGO/Si anode materials are shown in Fig. 5.12. The large initial capacity is due to the consumption of Li during the formation of a stable SEI layer. This effect is particularly pronounced for the FrGO sample which had a first cycle efficiency of 12%. After the initial SEI formation, however, the capacity of the FrGO anode was stable at 200mAhg^{-1} from 10 to 100 cycles.

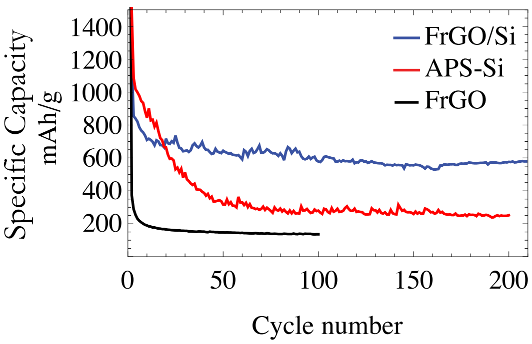

Fig. 5.12 200 cycles comparing the FrGO/Si anode with the APS-Si and FrGO anodes.

The APS-Si anode had an first cycle efficiency of 77%. This can also be attributed to the formation of an SEI layer with the Si NP. Because the SEI formed with Si is less stable than that formed with carbon, the capacity of the APS-Si fades steadily for 60 cycles. This fading is likely due to the repeated expansion of Si NP. While they are small enough to avoid fracturing, some will become electrically isolated and will no longer participate in the intercalation reaction. The capacity stabilizes to around 300mAhg^{-1} for the following cycles, less than 10% of the ideal Si capacity.

The FrGO/Si anode has a first cycle efficiency (FCE) of 39.5% but the efficiency rises above 90% for the second cycle. The capacity stabilizes to around 600 mAhg^{-1} after 10 cycles and is stable to at least 200 cycles. The first 10 cycles of for the FRGO-Si sample are shown in Figure 5.13.

The improved stability and long-term capacity of the FrGO/Si anode over the reference

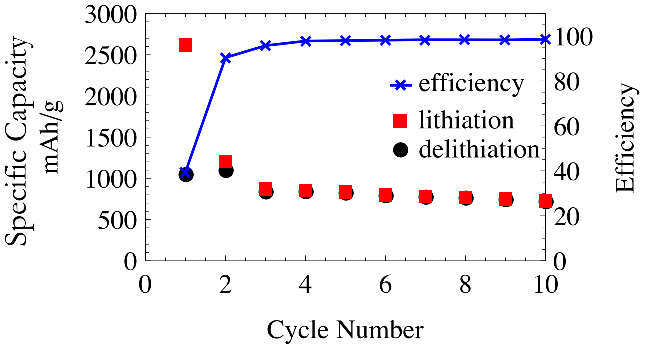

Fig. 5.13 First 10 cycles of the FrGO/Si anode. The initial capacity is large due to the formation of SEI

APS-Si anode indicates that the Si nanoparticle expansion is likely being appropriately buffered by the graphene encapsulation. To fully investigate this claim, SEM and TEM analysis post cycling is required.

5.8.2 Differential Capacity

The stable SEI formation on the large internal surface area of the FrGO and FrGO/Si samples results in low first cycle efficiency during formation. Analysis of the differential capacity (dQ/dV) curve in Figure 5.14 shows that the first cycle produces similar alloys for the SiNP sample and the FrGO/Si sample. These alloys match those found by Ogata et. al. in NMR studies on Si nanowires [**?**]. The initial lithiation creates the α-Li$_{3.75}$Si alloy at 100mV which goes through α-Li$_{2.0}$Si and α-Li$_{1.1}$Si alloys at 350 mV and 450 mV, respectively, during delithiation. Analysis of the differential capacity in Fig. 5.15 for the subsequent cycle shows the progression through these alloys. However, by the fifth cycle, the transition to and from α-Li$_{3.75}$Si is diminished and only the transition to and from

α-$Li_{2.0}Si$ participates in the electro-chemical reaction.

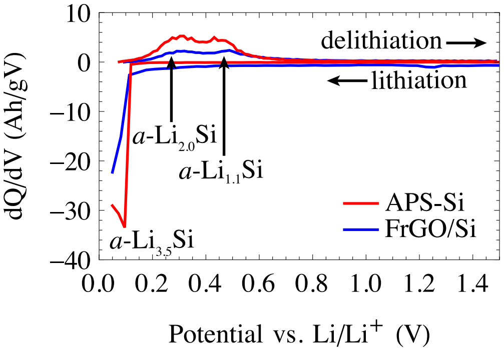

Fig. 5.14 Comparison of the first cycle dQdV curves for APS-Si and FrGO/Si. Lithiation/delithiation peaks from the APS-Si sample are also clearly present in the FrGO/Si sample.

5.9 Discussion

The novel layered composite FrGO/Si material has higher capacity than conventional graphite anodes, with the potential to significantly improve the gravimetric capacity of Li-ion batteries. Once the large amount of SEI was formed, the performance of the material was stable up to 200 cycles.

The large SEI formation, however, presents a serious issue for the performance of these anodes in a commercial battery system. The large irreversible capacity loss on the first cycle, a Coulombic efficiency of only around 40% consumes too much Li to be viable. Commercial carbon based materials can have initial Coulombic efficiencies approaching 95%. While some Li loss is acceptable given the stabilizing effect of the SEI, the level observed in the material is far too high. Work presented in the next chapter explores a method to reduce

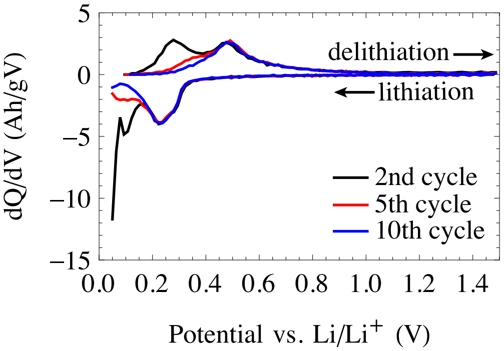

Fig. 5.15 Evolution of the dQdV peaks in FrGO/Si from the second to the tenth cycle. The capacity for later cycles comes only from transitions to and from α-$Li_{2.0}Si$.

the large interior surface area available for SEI formation while controllably introducing cracks and holes between the planes of graphene sheets.

More generally, we have shown that a layering strategy can be readily applied to evaporative rGO film synthesis. This opens the door to hierarchical rGO composite designs with micron sized layers that have a wider range of accessible properties than single layer films.

The issue of the loss of the higher capacity Li alloys is not well understood. It is clear that the high capacity $Li_{22}Si_5$ phase with a capacity of 4400mAhg^{-1} is not created in this, nor any Si containing anode reported in the literature. Even though the highest capacity alloys are not being utilized during cycling, the capacity provided by the α-$Li_{2.0}Si$ is a significant improvement over simple carbon materials.

Chapter 6

Hybrid Reduction Method for Controllable Properties of rGO Films

6.1 Introduction

The FrGO/Si anodes discussed in chapter five are functional, but the performance is lacking in the areas of initial efficiency, high rate capacity, and long term stability. While these deficiencies preclude the materials use as is in a commercial Li-ion battery, it is possible further optimizations could improve performance. In addition to the electrochemical performance, the mechanical strength is poor.

The open structure produced by flash reduction produces films that are only loosely bound together, and can disintegrate with handling. While thermally and chemically reduced GO films maintain much higher mechanical strength, they exhibit poor electrolyte penetration and poor rate performance. The penetration of electrolyte into the film is critical for improving performance and facilitating thicker films that would allow the improvement of volumetric capacity as well as gravimetric capacity.

This chapter describes a production method that can controllably introduce cracks into the structure to balance the benefits and trade offs of the open structure. The use of a dual reduction technique, first partially thermally reducing films, then completing the reduction with a photo-thermal process as before allows the tunable introduction of pores and cracks. The method produces films with similar conductivity and improved mechanical properties over flash reduction. Anodes produced with this method show much improved first cycle efficiency and significantly lower SEI formation.

This chapter first describes the method devised to produce dual thermal/flash reduced graphene oxide films (TFrGO). Material characterization is presented to highlight the benefits of this production technique. Mechanical properties are measured and compared to those for unreduced, thermally reduced and flash reduced GO. Finally, anodes produced with this technique and tested and compared to the FrGO/Si material discussed in the previous chapter.

6.2 Thermal Flash Reduction

For precise control of reduction time and temperature, samples were reduced in an oven designed for reflow soldering of printed circuit assemblies (DDM Novastar GF-12HT). The oven implements precise and repeatable temperature profiles and uses a mechanical conveyor to move samples through controlled heating zones. The profile shown in figure 6.1 was chosen in order to completely dry the sample before briefly raising the set point above the reduction temperature to allow the partial reduction of the sample. The surface of the samples reduced at low temperature have a dull lustre, as opposed to the bright metallic surface of previous samples reduced at 300°C .

Following thermal reductions, some films were subject to the same flash reduction used

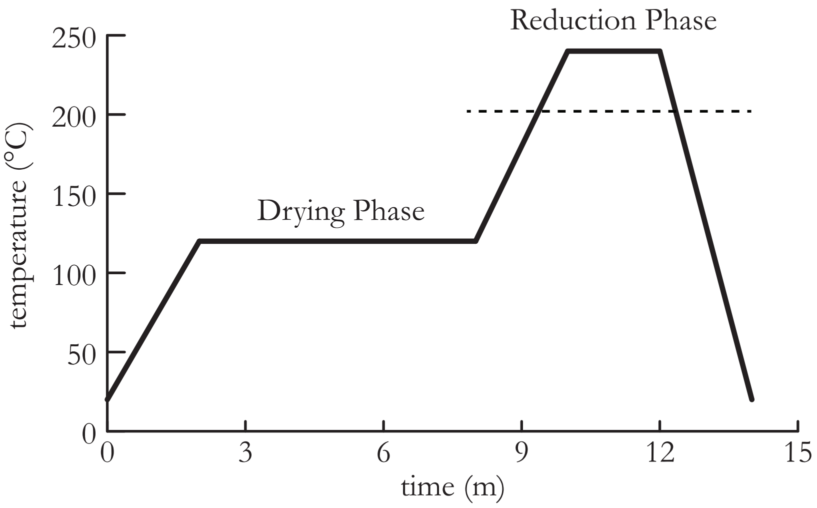

Fig. 6.1 Plot of the programmed heating profile for the reduction oven. The slope of transitions between temperatures is dependant on the thermal inertia of the materials being heated. For tuning the reduction, only the temperature during the reduction phase was changed.

for the materials in chapter 5. Samples were placed 2-3 cm below a flash lamp (B400, Paul C. Buff) and subjected to five 500 μs flashes with 160 W s energy each. The surface of the sample visibly changes, developing small black spots on the surface due to pits and cracks. The number of cracks and holes introduced with this dual reduction method is far less than for purely using flash reduction. Figure 6.2 shows a comparison of the surface appearance of FrGO, TrGO, TFrGO, and unreduced GO samples.

6.3 Material Characterization of Thermal/Flash Reduced GO

6.3.1 Sheet Resistance

To verify the level of reduction, a sheet resistance measurement was performed using the van der Pauw method described in section 3.5.1. Figure 6.3 shows the effects of flashing samples

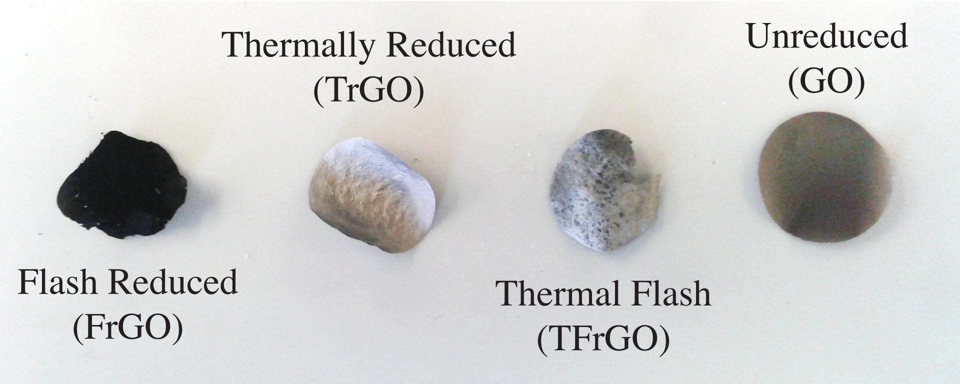

Fig. 6.2 Image comparing the appearance of GO films reduced with different methods as identified.

after reduction at increasing temperatures. GO samples reduced at lower temperature and then flashed exhibit a lower resistance than those at the middle temperature. Samples at the highest temperature appear to have reduced sufficiently enough that further flashes produced no change.

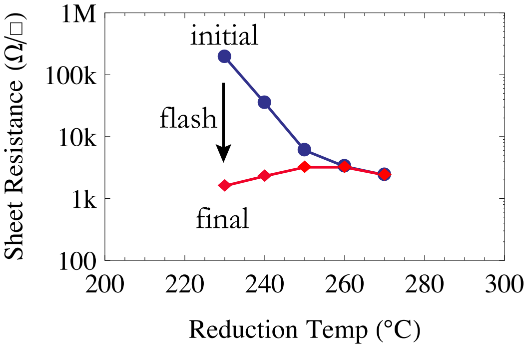

Fig. 6.3 Change in sheet resistance as a result of flash reduction after partial thermal reduction at increasing temperature. After 260°C , this treatment has no effect on the thermally reduced samples

6.3.2 Spectroscopic Characterization

Raman and XPS, shown in 6.4, were performed to characterize the change to the materials as a result of the dual reduction. There is no discernible difference in the Raman spectrum between the flash reduced, thermally reduced and the thermal/flash reduced materials. XPS was performed before reduction, after partial thermal reduction, and following the additional flash treatment. The additional flash treatment further reduces the sample as evidenced by the decrease in intensity from oxygen containing groups, and the increase in intensity from C-C bonds.

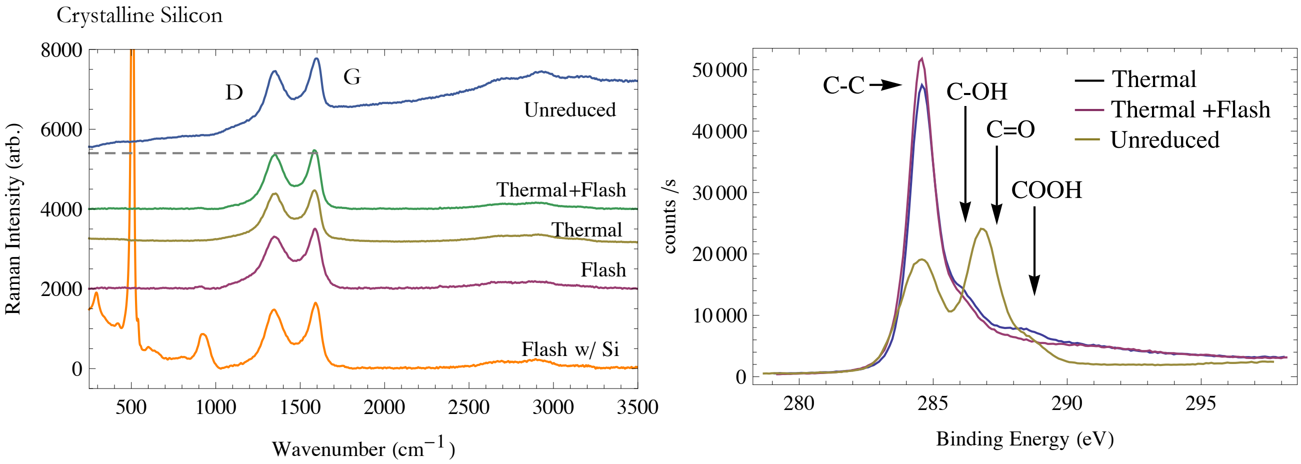

Fig. 6.4 (Left) Comparison of Raman spectra for films reduced with different methods including thermal/flash reduction. The spectrum for TFrGO is nearly identical to both TrGO and FrGO. (Right) XPS spectrum comparing the C1S spectrum before and after the extra flash reduction.

6.4 Mechanical Properties of Thermal/Flash Reduced GO

The mechanical strength of freestanding anodes is a large consideration. Current production methods for Li-ion battery anodes incorporate a roll to roll process for processing and coating Cu foil current collectors. The ideal replacement foil would be compatible with current production methods in order to minimize the cost of switching a production line. Pure copper has a tensile strength of 70 MPa. GO paper, depending on the method of production, can have a tensile strength as high as 300 MPa [100]. The strength of GO paper depends on the inter-sheet bonding, GO films can be made stronger with the addition of molecules that bind sheets together [92]. The strength of reduced GO paper also depends strongly on the inter-sheet bonding and varies significantly with the production and reduction method, but tensile strengths higher than 150MPa for films reduced in hydroiodic acid at 100°C [94] have been reported.

For mechanical measurements, a single sheet of GO paper was placed between glass slides and cut into several dog-bone shaped samples using a a pulsed UV laser beam (Vitrolux, 355 nm, 0.5 W, 4 kHz repetition rate, 45 ns pulse duration from Vitro Laser Solutions UG). Samples were then subjected to the different reduction methods to be compared. Thermal reduction prior to flash reduction was performed at 230°C . Thermal reduction alone was performed at 270°C . Samples that were flash reduced were ultimately too fragile to be measured and so were not included in this series of tests. An image of the samples tested appears in figure 6.5.

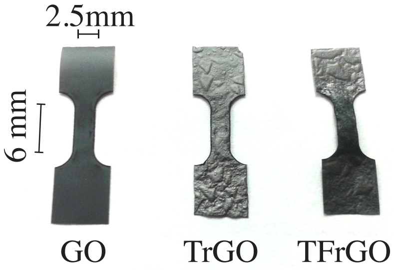

Fig. 6.5 Image of mechanical test samples. Samples are cut into a form with a thin middle section so the sample will mechanically fail there instead of where stress is induced from clamping the samples to the load tester. The FrGO material was too fragile to be included in this test.

Mechanical strength was measured on an tensile testing system (MTII/Fullam) with

10lb load cell. Prior to reduction the strength of the GO material can handle more then 80MPa of stress before breaking. The low yield strength of these GO samples as compared to others reported in the literature is due to the fabrication method, which produces films without the Al ions shown to improve the mechanical strength of GO paper produced with vacuum filtration on alumina filters [92]. Reduced samples failed at much lower stresses. TrGO samples failed at 8MPa with an elongation of 1.5%, while TFrGO samples failed at around 2MPa with an elongation of 2.6%. The higher strain before final yielding indicates TFrGO material is more ductile than TrGO. Measurements of tensile strength are shown in figure 6.6. While mechanical properties such as yield strength may be important for automated assembly of batteries in a commercial process, these properties do not necessarily translate into mechanical stability inside the cell during cycling. What is most important in this situation is that the individual components of the composite maintains electrical connectivity throughout the material during volume expansion upon lithiation.

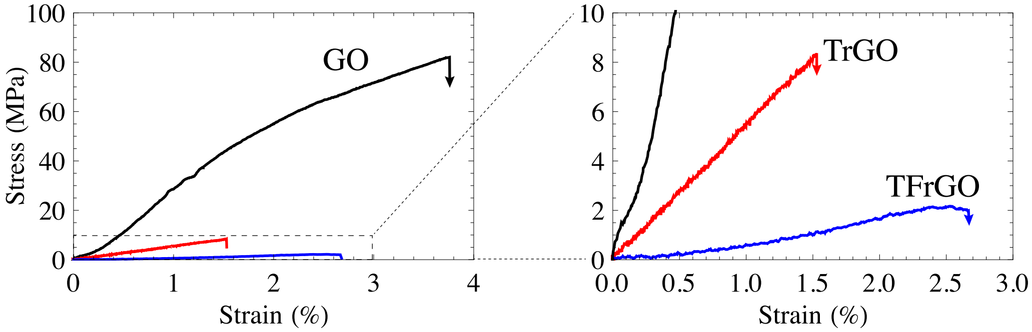

Fig. 6.6 Plot of stress/strain analysis on GO, TrGO and TFrGO materials. The FrGO material was too fragile to be tested with this system.

6.5 Thermal/Flash Reduced Layered Composite Anodes

The thermal/flash reduction method is capable of producing films with comparable conductivity, but higher mechanical strength than those reduced by flash reduction alone. Additionally, the level of porosity is greatly reduced. In the following sections, composite anodes synthesized using the same methods and materials described in Chapter 5, but reduced instead with the new method are discussed. Their performance as Li-ion battery anodes are analyzed in light of the previous chapter's results.

6.5.1 TGA

TGA was performed on the TFrGO/Si anodes to determine the weight fraction of Si in the material. Te results of the analysis are shown in Fig. 6.7. TGA analysis showed a discrepency in the Si content of the two materials. The TFrGO/Si material contained only 40% Si while the FrGO/Si material contained 60% Si by weight. The theoretical maximum capacity for the TFrGO material is 1900mAhg^{-1} compared to the 2600mAhg^{-1} for the FrGO/Si material.

6.5.2 SEM

SEM performed on the surface and cross-section of the material reveals the nanoscale structure of the material. Fig. 6.8 shows the surface and side profile of the TFrGO/Si anode film. The surface is somewhat transparent to electrons, which allows visualizing the Si NP embedded in the first few layers of material. The side profile clearly shows the delineation between thin silicon rich active layer, and the conductive rGO base layer. A low resolution view of the surface clearly shows some cracks and pores in the surface. There are clearly fewer than with the FrGO/Si anode film in Fig. 5.9.

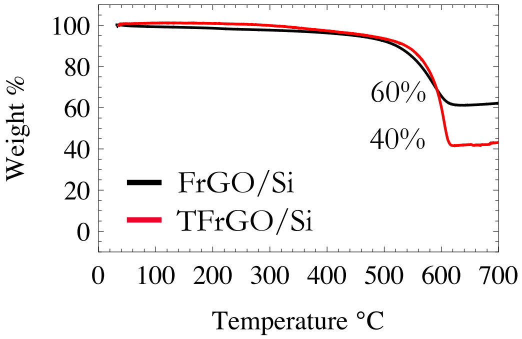

Fig. 6.7 TGA results comparing the dual reduced TFrGO/Si anode with the FrGO/Si anodes from the previous chapter. The TFrGO/Si anode contained only 40% Si by weight, compared to 60% for the FrGO/Si.

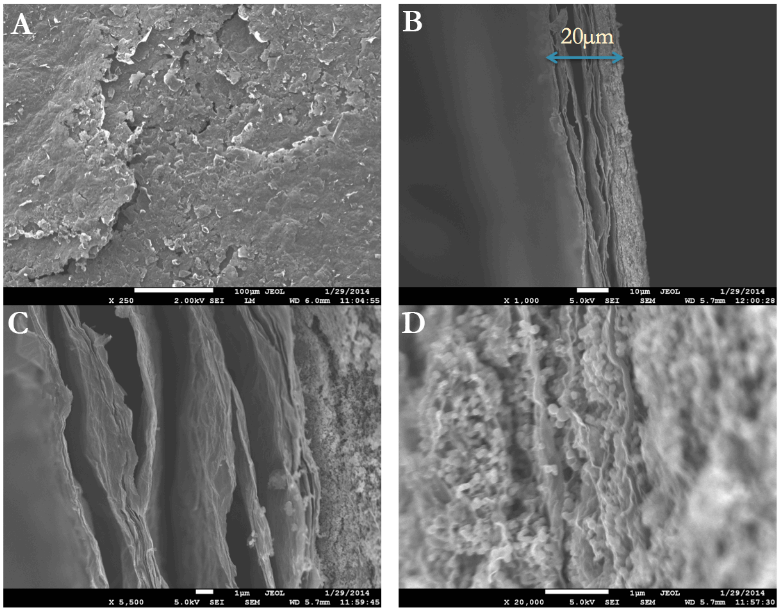

Fig. 6.8 SEM images of the surface (A) and side profile (B, C, & D) of a TFrGO/Si anode. The surface shows some cracks and openings into the material. The side profile shows the well ordered layers of the rGO base layer. Imaging close up on the Si rich layer shows the Si NP encapsulated in layers of graphene.

6.6 Battery Performance

Anodes were assembled in a nitrogen glove box into CR2032 coin cells with a Li metal counter electrode. A 1M $LiPF_6$ solution in equal parts ethyl carbonate (EC) and dimethyl carbonate (DMC) was used as the electrolyte. The chemical used in previous tests to Si capacity, fluoroethylene carbonate (FEC), was not available and was not used for the TFeGO/Si anode tests. A microporous tri-layered polypropylene (PP) and polyethylene (PE) polymer membrane (Celgard) was used as the separator.

The exclusion of FEC from the electrolyte makes comparison of the long term stability of TFrGO/Si anodes to the FrGO/Si and Si anodes difficult. The effect that FEC has in stabilizing the long term capacity of Si anodes is clear when comparing the three anodes. The FrGO/Si and TFrGO/Si anode have similar initial performance when taking into account the difference in Si% by weight (60% vs. 40%). Fig. 6.9 shows the first hundred cycles of the four materials being compared. For the first 15 cycles, on the scale of the graph, the FrGO/Si and TFrGO/Si materials behave similarly. However, by 40 cycles the capacity continues to fade, and by cycle 100 has capacity no better than the FRGO anode containing no Si.

The improved performance of the TFrGO/Si anode is clear, however, when looking at the first cycle. The initial capacity loss due to SEI formation in the open porous structure of the FrGO/Si anode is mitigated with the TFrGO/Si material. Fig 6.10 shows the voltage capacity profile for these two materials. The initial amount of Li-ions inserted into the anode in the first lithiation of the FrGO/Si sample equate to more than $2500 mAhg^{-1}$ of capacity, while the TFrGO/Si sample exhibits insertion of Li-ions equating to $1600 mAhg^{-1}$ of capacity. Upon delithiation, the amount of Li extracted is nearly the same for the two materials, just over $1000 mAhg^{-1}$ of capacity.

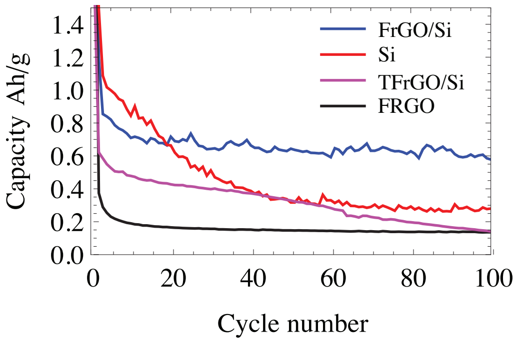

Fig. 6.9 Discharge capacity for 100 cycles of FrGO/Si, Si, TFrGO/Si and FRGO anodes.

Fig. 6.11 shows the differential capacity profile for the first lithiation/delithiation cycle of the two materials. The same peak for the lithation of crystalline Si is shown in both materials. The size of the peak for the TFrGO/Si material is greater than that of the FrGO/Si sample, despite containing 33% less Si. The significant SEI formation on the FrGO/Si smaple is seen as non-zero dQ/dV as the cell potential is changed from 1.5 V to 0.1 V when the Si Lithiation occurs. For delithiation, the peaks of the TFrGO/Si sample are again comparable if not slightly larger than those of the FrGO/Si sample.

6.7 Discussion

A direct comparison of the TFrGO/Si and FrGO/Si materials is difficult. The difference in initial Si content complicates the comparison of gravimetric capacity. The exclusion of Si stabilizing electrolyte additives also makes it impossible to compare the long term cycle ability of the two materials. Further work is required to improve control over the composition of rGO/Si composites and firmly establish the optimum composition and processing

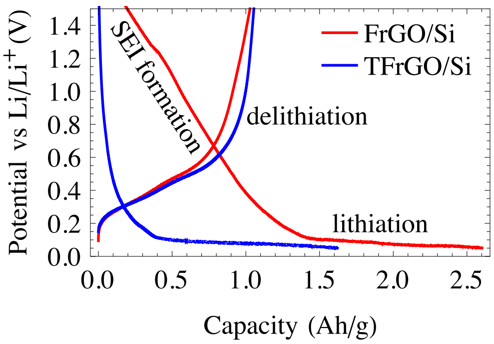

Fig. 6.10 Plot of the potential of the half-cell during the first lithiation/delithation cycle for FrGO/Si and TFrGO/Si anodes. The slower drop in potential and massive 2500mAhg^{-1} capacity for the FrGO/Si anode during lithiation is indicative of large amounts of SEI formation causing irreversible capacity loss. The two samples exhibit nearly the same 1000mAhg^{-1} first cycle delithiation capacity.

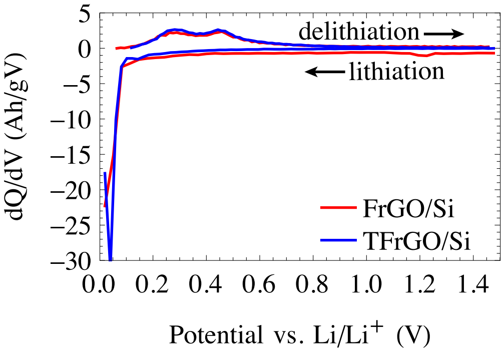

Fig. 6.11 Differential capacity plot comparing a TFrGO/Si anode with an FrGO/Si anode. Both have the same characteristic c-Si alloy and a-Si de-alloy peaks. A significant amount of Li is entering the FrGO/Si anode before the main lithiation peak as indicated by the non-zero value of dQ/dV between 1.5V and 100mV when Li begins alloying with Si. The delithiation peaks for TFrGO/Si are larger despite having lower theoretical capacity than the FrGO/Si sample.

conditions for Li ion anode applications.

While GO paper films can be reduced to create strong conductive anodes for Li-ion batteries, the literature confirms that the lack of porosity in thermally reduced GO films limits the effectiveness of these materials in anode applications. On the other hand flash reduction alone clearly results in a highly porous material with limited mechanical strength and high levels of SEI formation. The process used to create the TFrGO/Si material represents a compromise between these two methods. SEM analysis shows the porosity of the TFrGO/Si. Additionally, analysis of the initial lithiation and delithiation cycle shows that far less SEI formation occurs initially on the TFrGO/Si material. The mechanical properties of the films could be improved by using additional functionalization to bind the individual sheets together in the material, but any method used must not interfere with the electrochemistry of the anode system.

The degree of porosity achieved with the dual reduction method can be tuned by adjusting the amount of initial thermal reduction performed. More initial reduction, either with higher temperatures of longer reduction times, followed by flash reduction results in lower overall porosity. The final conductivity of the material is low regardless of the amount of initial reduction. The level of porosity is tunable without compromising conductivity, and could be optimized for the desired performance. More porosity may be desirable for faster charge/discharge dynamics, while low porosity is desirable for low SEI formation and higher volumetric capacity.

Chapter 7

Summary and Future Work

7.1 Summary

In this thesis, we presented a family of engineered Si / graphene composites consisting of Si nanoparticles attached to micron scale graphene flakes. The inclusion of significant amounts of GNP material serves to improve the CE for the first cycles by buffering the volume expansion and allowing the formation of stabilizing SEI with the carbon materials.

By producing and testing three composite materials with nearly identical formulations, we have experimentally shown that the nature of the attachment between Si nanoparticles and graphene flakes - physical, ionic, or covalent - is critical to the suppression of capacity fading in the composite anodes. The covalent coupling of Si NP to GNP creates a more stable material, with better cycle ability and less capacity fading than a mixed composite material.

A covalently coupled composite material containing 60% Si by weight has an initial capacity after formation of 1600mAhg^{-1} , more than 4 times greater than commercial carbon anode materials. The capacity of this material after 50 cycles is higher than previously reported for a covalently coupled Si NP/graphene material.

In the next chapter we presented a novel strategy for improving the total gravimetric capacity of the Li-ion battery anode by eliminating the heavy copper foil current collector. A light-weight, flash reduced graphene oxide thin film current collector is integrated with a high capacity film of graphene encapsulated Si nanoparticles. This is the first report on a composite freestanding Si/graphene film produced with photo-thermal reduction techniques. The resulting two-layered conductive anode film contains 60% Si by weight, and has a gravimetric capacity of nearly 1100mAhg^{-1} after the formation cycle . The specific capacity after 200 cycles is stable at greater than 600mAhg^{-1} .

Most importantly, this work shows for the first time that a layering strategy can be readily applied to evaporative rGO film synthesis, allowing hierarchical rGO composite designs with micron sized layers that have a wider range of accessible properties than single layer films.

The final contribution of this thesis is the comparative study of three low energy reduction techniques. Low temperature thermal reduction, flash lamp induced photo-thermal reduction, and a novel hybrid reduction technique for the preparation of Si / graphene composites were applied to GO and composite Si/GO films.

Measurements on the electrical properties of reduced films show similar conductivities can be achieved with each technique, while measurements of the mechanical properties show a wide range of material strength. Flash reduced GO films are open and porous, but fragile. Thermally reduced graphene oxide films are mechanically robust, but exhibit poor electrolyte penetration and poor rate performance when used as Li-ion battery anodes. The use of a hybrid reduction technique, partial thermal reduction followed by reduction with a flash process, allows for the tunable introduction of pores. The films can be made with higher yield strength than flash reduction alone.

Measurements of composite Si/graphene anodes produced using the hybrid reduction technique show the material has a gravimetric capacity of more than $1000 \mathrm{mAhg}^{-1}$ after formation, nearly as much as flash reduced composite anodes despite containing 33 % less Si. Analysis of the formation cycle shows significantly lower initial capacity loss, consistent with less SEI formation. These experiments demonstrate that a hybrid reduction technique used to produce free standing composite materials is not only applicable to high energy density Li-ion battery anodes but potentially to other high capacity electrodes for cathodes, capacitors and electrochemical sensors as well.

7.2 Future Work

The work reported in this thesis this leaves many questions and suggests further enquiry for the synthesis of improved Li-ion battery electrodes. The following is a summary of potential new avenues of research.

1. **Application of covalent attachment techniques to smaller Si NP and Si NP with reduced native oxide.**

   Recently reported work clearly shows a benefit to smaller Si NP materials in preventing capacity fading. There is a trade-off however between the size of the NP and the surface area. As the size decreases, the surface area goes up, leading to the production of more SEI. With smaller Si NP covalently attached to graphene materials, the beneficial effect of SEI formation with carbon surface instead of Si might mitigate this problem and lead to even higher capacity, longer life anodes. Additionally, because the formation of native oxide on Si surface increases with surface area, the removal of most of this oxide by treatment with HF before functionalization should be explored.

2. **Reproduce the TFrGO/Si material with improved Si loading and capacity stabilizing additives to facilitate a more accurate comparison. Optimize the performance by tuning the porosity of the material.**

   A more complete investigation of the hybrid reduction technique introduced in this work requires a systematic study of the effect of tuning of porosity with improved consistency of parameters. Reproducing the work on composite materials produced using hybrid reduction technique while optimizing the Si content, reduction method, and electrolyte composition could lead to significantly higher Li-ion anode performance for this class of material.

3. **Explore further optimizations to reduction.**

   The reduction temperatures used in this work are not sufficient for the full reduction of GO. Performing high temperature reduction in an anaerobic environment or a strong chemical reduction process after introducing pores with flash reduction will further reduce the rGO materials. This treatment will improve conductivity and alter the mechanical properties as well. Further reduction will limit undesired reactions between electrolyte and the remaining functional groups on the rGO material. A higher conductivity anode may be essential for higher current applications.

4. **Investigate methods to enhance mechanical properties of rGO composite films.**

   The mechanical strength of GO films can be improved by cross-linking layers with monomers, polymers, or polyvalent ions. If mechanical strength can be improved without sacrificing electrochemical performance, the production of freestanding anodes could potentially scale with an automated roll to roll process. These materials would not be limited in usefulness to Li-ion battery anodes but have the potential to be useful for their purely mechanical properties as well.

5. **Explore uses of GO and rGO films for other mechanical applications.**

   The high strength to weight ratio of GO films suggests they may find many uses in ultra lightweight structural materials, micro-mechanical systems, and acoustic or ultra-sonic transducers. Additional work has already been done to create functional acoustic membranes using the techniques described here.

References

[1] Susan Solomon, *Climate Change 2007 - The Physical Science Basis*, Contribution of Working Group Ito the Fourth Assessment Report of the Intergovernmental Panel on Climate Change. Cambridge University Press New York (2007).

[2] Stacy C Davis, Susan W Diegel, and Robert G Boundy, "Transportation Energy Data Book", U.S. Department of Energy Oak Ridge (2013).

[3] J Blunden and D S Arndt, "State of the Climate in 2014", *Bulletin of the American Meteorological Society* **96**(7), pp. S1–S267 (2015).

[4] International Energy Agency, *Transport, energy and CO : moving toward sustainability.*, International Energy Agency Paris (2009).

[5] J Tarascon and M Armand, "Issues and challenges facing rechargeable lithium batteries", *Nature* **414**(2001), pp. 359–367 (2001).

[6] Akira Yoshino, "The Birth of the Lithium-Ion Battery", *Angewandte Chemie International Edition* **51**(24), pp. 5798–5800 (2012).

[7] R Yazami and P Touzain, "A reversible graphite-lithium negative electrode for electrochemical generators", *Journal of Power Sources* **9**(1983), pp. 365–371 (1983).

[8] K Mizushima, P C Jones, P J Wiseman, and J B Goodenough, "Li x CoO 2 (0< x 1): A new cathode material for batteries of high energy density", *Solid State Ionics* **3/4**(1981), pp. 171–174 (1981).

[9] X. Yuan, H. Liu, and J. Zhang, *Lithium-Ion Batteries: Advanced Materials and Technologies*, Green Chemistry and Chemical Engineering. Taylor & Francis (2011).

[10] Venkat Srinivasan, "Batteries for vehicular applications", *AIP Conference Proceedings* **1044**(1), pp. 283–296 (2008).

[11] H Wu, G Zheng, N Liu, T Carney, Y Yang, and Y Cui, "Engineering empty space between Si nanoparticles for lithium-ion battery anodes", *Nano Letters* **12**(2012), pp. 904–909 (2012).

[12] Peter G Bruce, "Solid-state chemistry of lithium power sources", *Chemical Communications* **19**(1997), pp. 1817–1824 (1997).

[13] L Gaines and R Cuenca, "Costs of Lithium-ion Batteries for Vehicles", Technical report Argonne National Laboratory (2000).

[14] D. Linden and T.B. Reddy, *Handbook of Batteries*, McGraw-Hill handbooks. McGraw-Hill (2002).

[15] J Dunn, L Gaines, M Barnes, M Wang, and J Sullivan, "Material and energy flows in the materials production, assembly, and end-of-life stages of the automotive lithium-ion battery life cycle", U.S. Department of Energy Oak Ridge (2012).

[16] A J Smith, J C Burns, S Trussler, and J R Dahn, "Precision measurements of the coulombic efficiency of lithium-ion batteries and of electrode materials for lithium-ion batteries", *Journal Of The Electrochemical Society* **157**(2), pp. A196–A202 (2010).

[17] M Winter and J Besenhard, "Electrochemical lithiation of tin and tin-based intermetallics and composites", *Electrochimica Acta* **45**(1999), pp. 31–50 (1999).

[18] H Marsh and F R Reinoso, *Activated Carbon*, Elsevier Science (2006).

[19] Martin Winter, Jürgen Besenhard, Michael Spahr, and Petr Novak, "Insertion electrode materials for rechargeable lithium batteries", *Advanced Materials* **10**(10), pp. 725–763 (1998).

[20] Ping Yu, B N Popov, J A Ritter, and R E White, "Determination of the Lithium Ion Diffusion Coefficient in Graphite", *Journal Of The Electrochemical Society* **146**(1), pp. 8–14 (1999).

[21] M Endo, C Kim, K Nishimura, T Fujino, and K Miyashita, "Recent development of carbon materials for Li ion batteries", *Carbon* **38**(2), pp. 183–197 (2000).

[22] Edward Buiel and J R Dahn, "Li-insertion in hard carbon anode materials for Li-ion batteries", *Electrochimica Acta* **45**(1), pp. 121–130 (1999).

[23] A K Geim and K S Novoselov, "The rise of graphene", *Nature Materials* **6**(3), pp. 183–191 (2007).

[24] B Brodie, "On the atomic weight of graphite", *Philosophical Transactions of the Royal Society of London* **149**(1859), pp. 249–259 (1859).

[25] W Hummers Jr and R Offeman, "Preparation of graphitic oxide", *Journal Of The American Chemical Society* **80**(6), pp. 1339 (1958).

[26] D A Dikin, S Stankovich, E J Zimney, R D Piner, GHB Dommett, G Evmenenko, S T Nguyen, and R S Ruoff, "Preparation and characterization of graphene oxide paper", *Nature* **448**(2007), pp. 457–460 (2007).

[27] E Yoo, J Kim, E Hosono, H Zhou, and T Kudo, "Large reversible Li storage of graphene nanosheet families for use in rechargeable lithium ion batteries", *Nano Letters* **8**(8), pp. 2277–2282 (2008).

[28] G Wang, X Shen, J Yao, and J Park, "Graphene nanosheets for enhanced lithium storage in lithium ion batteries", *Carbon* **47**(8), pp. 2049–2053 (2009).

[29] A Gerouki, M A Goldner, R B Goldner, T E Haas, T Y Liu, and S Slaven, "Density of states calculations of small diameter single graphene sheets", *Journal Of The Electrochemical Society* **143**(11), pp. L262–L263 (1996).

[30] Z Wu, W Ren, L Xu, F Li, and H Cheng, "Doped graphene sheets as anode materials with superhigh rate and large capacity for lithium ion batteries", *ACS Nano* **5**(7), pp. 5463–5471 (2011).

[31] X Li, D Geng, Y Zhang, X Meng, R Li, and X Sun, "Superior cycle stability of nitrogen-doped graphene nanosheets as anodes for lithium ion batteries", *Electrochemistry Communications* **13**(2011), pp. 822–825 (2011).

[32] T D Hatchard and J R Dahn, "In situ XRD and electrochemical study of the reaction of lithium with amorphous silicon", *Journal Of The Electrochemical Society* **151**(6), pp. A838–A842 (2004).

[33] V L Chevrier, J W Zwanziger, and J R Dahn, "First principles studies of silicon as a negative electrode material for lithium-ion batteries", *Canadian Journal of Physics* **87**(6), pp. 625–632 (2009).

[34] Hui Wu and Yi Cui, "Designing nanostructured Si anodes for high energy lithium ion batteries", *Nano Today* **7**(5), pp. 414–429 (2012).

[35] L Y Beaulieu, K W Eberman, R L Turner, L J Krause, and J R Dahn, "Colossal Reversible Volume Changes in Lithium Alloys", *Electrochemical and Solid-State Letters* **4**(9), pp. A137–A140 (2001).

[36] S Bourderau, T Brousse, and D Schleich, "Amorphous silicon as a possible anode material for Li-ion batteries", *Journal of Power Sources* **82**(1999), pp. 233–236 (1999).

[37] Jeannine R Szczech and Song Jin, "Nanostructured silicon for high capacity lithium battery anodes", *Energy & Environmental Science* **4**(1), pp. 56 (2011).

[38] T Takamura, M Uehara, J Suzuki, and K Sekine, "High capacity and long cycle life silicon anode for Li-ion battery", *Journal of Power Sources* **158**(2006), pp. 1401–1404 (2006).

[39] M Uehara, J Suzuki, K Tamura, and K Sekine, "Thick vacuum deposited silicon films suitable for the anode of Li-ion battery", *Journal of Power Sources* **146**(2005), pp. 441–444 (2005).

[40] H Guo, H Zhao, C Yin, and W Qiu, "A nanosized silicon thin film as high capacity anode material for Li-ion rechargeable batteries", *Materials Science and Engineering: B* **131**(2006), pp. 173–176 (2006).

[41] J Graetz, C C Ahn, Rachid Yazami, and Brent Fultz, "Highly reversible lithium storage in nanostructured silicon", *Electrochemical and Solid-State Letters* **6**(9), pp. A194–A197 (2003).

[42] S Ohara, J Suzuki, K Sekine, and T Takamura, "A thin film silicon anode for Li-ion batteries having a very large specific capacity and long cycle life", *Journal of Power Sources* **136**(2004), pp. 303–306 (2004).

[43] H Jung, M Park, Y Yoon, G Kim, and S Joo, "Amorphous silicon anode for lithium-ion rechargeable batteries", *Journal of Power Sources* **115**(2003), pp. 346–351 (2003).

[44] L Cui, R Ruffo, C Chan, H Peng, and Y Cui, "Crystalline-amorphous core- shell silicon nanowires for high capacity and high current battery electrodes", *Nano Letters* **9**(1), pp. 491–495 (2008).

[45] C Chan, H Peng, G Liu, K McIlwrath, and X Zhang, "High-performance lithium battery anodes using silicon nanowires", *Nature* **3**(2008), pp. 31–35 (2008).

[46] C Chan, R Patel, M O'Connell, B Korgel, and Y Cui, "Solution-grown silicon nanowires for lithium-ion battery anodes", *ACS Nano* **4**(3), pp. 1443–1450 (2010).

[47] M Ge, J Rong, and X Fang, "Porous Doped Silicon Nanowires for Lithium Ion Battery Anode with Long Cycle Life", *Nano Letters* **12**(2012), pp. 2318–2323 (2012).

[48] T Burr, A Seraphin, E Werwa, and K Kolenbrander, "Carrier transport in thin films of silicon nanoparticles", *Physical Review B* **46**(8), pp. 4818–4824 (1997).

[49] Hong Li, Xuejie Huang, Liquan Chen, Zhengang Wu, and Yong Liang, "A High Capacity NanoSi Composite Anode Material for Lithium Rechargeable Batteries", *Electrochemical and Solid-State Letters* **2**(11), pp. 547–549 (1999).

[50] H Kim, M Seo, M H Park, and Jaephil Cho, "A Critical Size of Silicon Nano-Anodes for Lithium Rechargeable Batteries", *Angewandte Chemie International Edition* **49**(12), pp. 2146–2149 (2010).

[51] Shengnan Yang, Qinmin Pan, and Jia Liu, "Improving the cycleability of Si anodes by covalently grafting with 4-carboxyphenyl groups", *Electrochemistry Communications* **12**(3), pp. 479–482 (2010).

[52] H Xiang, K Zhang, G Ji, J Lee, C Zou, X Chen, and J Wu, "Graphene/nanosized silicon composites for lithium battery anodes with improved cycling stability", *Carbon* **49**(5), pp. 1787–1796 (2011).

[53] X Zhou, Y X Yin, L J Wan, and Y G Guo, "Facile synthesis of silicon nanoparticles inserted into graphene sheets as improved anode materials for lithium-ion batteries", *Chemical Communications* **48**(16), pp. 2198–2200 (2012).

[54] S Yang, G Li, Q Zhu, and Q Pan, "Covalent binding of Si nanoparticles to graphene sheets and its influence on lithium storage properties of Si negative electrode", *Journal of Materials Chemistry* **22**(2012), pp. 3420–3425 (2012).

[55] Min Zhou, Fan Pu, Zhao Wang, Tingwei Cai, Hao Chen, Haiyong Zhang, and Shiyou Guan, "Facile synthesis of novel Si nanoparticles–graphene composites as high-performance anode materials for Li-ion batteries", *Physical Chemistry Chemical Physics* **15**(27), pp. 11394 (2013).

[56] Guangyu Zhao, Li Zhang, Yufeng Meng, Naiqing Zhang, and Kening Sun, "Decoration of graphene with silicon nanoparticles by covalent immobilization for use as anodes in high stability lithium ion batteries", *Journal of Power Sources* **240**(2013), pp. 212–218 (2013).

[57] Wei Wang, Moni Kanchan Datta, and Prashant N Kumta, "Silicon-based composite anodes for Li-ion rechargeable batteries", *Journal of Materials Chemistry* **17**(30), pp. 3229–3237 (2007).

[58] Z S Wen, J Yang, B F Wang, K Wang, and Y Liu, "High capacity silicon/carbon composite anode materials for lithium ion batteries", *Electrochemistry Communications* **5**(2), pp. 165–168 (2003).

[59] G Wang, J H Ahn, J Yao, S Bewlay, and H K Liu, "Nanostructured Si–C composite anodes for lithium-ion batteries", *Electrochemistry Communications* **6**(2004), pp. 689–692 (2004).

[60] Pengfei Gao, Jianwei Fu, Jun Yang, Rongguan Lv, Jiulin Wang, Yanna Nuli, and Xiaozhen Tang, "Microporous carbon coated silicon core/shell nanocomposite via in

situ polymerization for advanced Li-ion battery anode material", *Physical Chemistry Chemical Physics* **11**(47), pp. 11101–11105 (2009).

[61] Juchen Guo, Ann Sun, Xilin Chen, Chunsheng Wang, and Ayyakkannu Manivannan, "Cyclability study of silicon–carbon composite anodes for lithium-ion batteries using electrochemical impedance spectroscopy", *Electrochimica Acta* **56**(11), pp. 3981–3987 (2011).

[62] Nian Liu, Hui Wu, Matthew T McDowell, Yan Yao, Chongmin Wang, and Yi Cui, "A Yolk-Shell Design for Stabilized and Scalable Li-Ion Battery Alloy Anodes", *Nano Letters* **12**(6), pp. 3315–3321 (2012).

[63] J Luo, X Zhao, J Wu, H D Jang, H H Kung, and J Huang, "Crumpled Graphene-Encapsulated Si Nanoparticles for Lithium Ion Battery Anodes", *Journal Of Physical Chemistry Letters* **3**(13), pp. 1824–1829 (2012).

[64] Y Zhao, X Liu, H Li, T Zhai, and H Zhou, "Hierarchical micro/nano porous silicon Li-ion battery anodes", *Chemical Communications* **48**(2012), pp. 5079–5081 (2012).

[65] M Yazici, D Krassowski, and J Prakash, "Flexible graphite as battery anode and current collector", *Journal of Power Sources* **141**(2005), pp. 171–176 (2005).

[66] Y Hu, X Li, D Geng, M Cai, R Li, and X Sun, "Influence of paper thickness on the electrochemical performances of graphene papers as an anode for lithium ion batteries", *Electrochimica Acta* **91**(2013), pp. 227–233 (2013).

[67] F Yao, F Güneş, H Ta, and S Lee, "Diffusion mechanism of lithium ion through basal plane of layered graphene", *Journal Of The American Chemical Society* **134**(2012), pp. 8646–8654 (2012).

[68] X Zhao, C M Hayner, M C Kung, and H H Kung, "In-Plane Vacancy-Enabled High-Power Si–Graphene Composite Electrode for Lithium-Ion Batteries", *Advanced Energy Materials* **1**(6), pp. 1079–1084 (2011).

[69] R Mukherjee, A V Thomas, A Krishnamurthy, and N Koratkar, "Photo-Thermally Reduced Graphene As High Power Anodes for Lithium Ion Batteries", *ACS Nano* **6**(9), pp. 7867–7878 (2012).

[70] J Z Wang, C Zhong, S L Chou, and H K Liu, "Flexible free-standing graphene-silicon composite film for lithium-ion batteries", *Electrochemistry Communications* **12**(2010), pp. 1467–1470 (2010).

[71] J K Lee, K B Smith, C M Hayner, and H H Kung, "Silicon nanoparticles–graphene paper composites for Li ion battery anodes", *Chemical Communications* **46**(12), pp. 2025–2027 (2010).

[72] H C Tao, L Z Fan, Y Mei, and X Qu, "Self-supporting Si/Reduced Graphene Oxide nanocomposite films as anode for lithium ion batteries", *Electrochemistry Communications* **13**(2011), pp. 1332–1335 (2011).

[73] Ado Jorio, Mildred S Dresselhaus, Riichiro Saito, and Gene Dresselhaus, *Raman Spectroscopy in Graphene Related Systems*, John Wiley & Sons (2011).

[74] L J van der Pauw, "A method of measuring specific resistivity and hall effect of discs of arbitrary shape", *Philips Research Reports* **13**, pp. 1–9 (1958).

[75] Chang Huan and Sun Shu-Qing, "Silicon nanoparticles: Preparation, properties, and applications", *Chinese Physics B* **23**(8), pp. 088102 (2014).

[76] Xiao Hua Liu, Li Zhong, Shan Huang, Scott X Mao, Ting Zhu, and Jian Yu Huang, "Size-Dependent Fracture of Silicon Nanoparticles During Lithiation", *ACS Nano* **6**(2), pp. 1522–1531 (2012).

[77] M Delamar, R Hitmi, and J Pinson, "Covalent modification of carbon surfaces by grafting of functionalized aryl radicals produced from electrochemical reduction of diazonium salts", *Journal Of The American Chemical Society* **114**(1992), pp. 5883–5884 (1992).

[78] P Allongue, M Delamar, and B Desbat, "Covalent modification of carbon surfaces by aryl radicals generated from the electrochemical reduction of diazonium salts", *Journal Of The American Chemical Society* **119**(1997), pp. 201–207 (1997).

[79] G Zeb, P Gaskell, X Le, X Xiao, T Szkopek, and M Cerruti, "Decoration of Graphitic Surfaces with Sn Nanoparticles through Surface Functionalization using Diazonium Chemistry", *Langmuir* **28**(2012), pp. 13042–13050 (2012).

[80] Gul Zeb, Peter Gaskell, Yongnam Kim, Ghulam Jalani, Xingcheng Xiao, Thomas Szkopek, and Marta Cerruti, "The importance of covalent coupling in the synthesis of high performance composite anodes for lithium ion batteries", *RCS Advances* **6**(2016), pp. 45519–45524 (2016).

[81] G Che, B Lakshmi, E Fisher, and C Martin, "Carbon nanotubule membranes for electrochemical energy storage and production", *Nature* **393**(1998), pp. 346–349 (1998).

[82] R Morris, B Dixon, T Gennett, R Raffaelle, and M J Heben, "High-energy, rechargeable Li-ion battery based on carbon nanotube technology", *Journal of Power Sources* **138**(2004), pp. 277–280 (2004).

[83] S Chew, S Ng, J Wang, P Novák, F Krumeich, S L Chou, J Chen, and H K Liu, "Flexible free-standing carbon nanotube films for model lithium-ion batteries", *Carbon* **47**(13), pp. 2976–2983 (2009).

[84] C Wang, D Li, C Too, and G Wallace, "Electrochemical properties of graphene paper electrodes used in lithium batteries", *Chemistry Of Materials* **21**(2009), pp. 2604–2606 (2009).

[85] Ali Abouimrane, Owen C Compton, Khalil Amine, and SonBinh T Nguyen, "Non-Annealed Graphene Paper as a Binder-Free Anode for Lithium-Ion Batteries", *The Journal of Physical Chemistry C* **114**(2010), pp. 12800–12804 (2010).

[86] Lin Wang, Xin Deng, Pei-Xia Dai, Yu-Guo Guo, Dong Wang, and Li-Jun Wan, "Initial solid electrolyte interphase formation process of graphite anode in LiPF6 electrolyte: an in situ ECSTM investigation", *Physical Chemistry Chemical Physics* **14**(20), pp. 7330–7336 (2012).

[87] Yu-Chan Yen, Sung-Chieh Chao, Hung-Chun Wu, and Nae-Lih Wu, "Study on Solid-Electrolyte-Interphase of Si and C-Coated Si Electrodes in Lithium Cells", *Journal Of The Electrochemical Society* **156**(2), pp. A95–A102 (2009).

[88] D R Dreyer, S Park, C W Bielawski, and R S Ruoff, "The chemistry of graphene oxide", *Chemical Society Reviews* **39**(1), pp. 228–240 (2010).

[89] N Kovtyukhova, P Ollivier, and B Martin, "Layer-by-layer assembly of ultrathin composite films from micron-sized graphite oxide sheets and polycations", *Chemistry Of Materials* **11**(1999), pp. 771–778 (1999).

[90] M El-Kady, V Strong, S Dubin, and R Kaner, "Laser scribing of high-performance and flexible graphene-based electrochemical capacitors", *Science* **335**(2012), pp. 1326–1330 (2012).

[91] V Strong, S Dubin, M El-Kady, A Lech, Y Wang, B H Weiller, and R B Kaner, "Patterning and electronic tuning of laser scribed graphene for flexible all-carbon devices", *ACS Nano* **6**(2), pp. 1395–1403 (2012).

[92] Che-Ning Yeh, Kalyan Raidongia, Jiaojing Shao, Quan-Hong Yang, and Jiaxing Huang, "On the origin of the stability of graphene oxide membranes in water", *Nature Chemistry* **7**(2015), pp. 166–170 (2015).

[93] D Li, M Mueller, S Gilje, and R Kaner, "Processable aqueous dispersions of graphene nanosheets", *Nature* **3**(2008), pp. 101–105 (2008).

[94] Songfeng Pei, Jinping Zhao, Jinhong Du, Wencai Ren, and Hui-Ming Cheng, "Direct reduction of graphene oxide films into highly conductive and flexible graphene films by hydrohalic acids", *Carbon* **48**(15), pp. 4466–4474 (2010).

[95] L J Cote, R Cruz-Silva, and J Huang, "Flash Reduction and Patterning of Graphite Oxide and Its Polymer Composite", *Journal Of The American Chemical Society* **131**(31), pp. 11027–11032 (2009).

[96] S Gilje, S Dubin, A Badakhshan, J Farrar, S A Danczyk, and R B Kaner, "Photothermal deoxygenation of graphene oxide for patterning and distributed ignition applications", *Advanced Materials* **22**(3), pp. 419–423 (2010).

[97] S Pei and H M Cheng, "The reduction of graphene oxide", *Carbon* **50**(9), pp. 3210–3228 (2011).

[98] V Etacheri, O Haik, Y Goffer, G Roberts, I C Stefan, R Fasching, and D Aurbach, "Effect of fluoroethylene carbonate (FEC) on the performance and surface chemistry of Si-nanowire Li-ion battery anodes", *Langmuir* **28**(2012), pp. 965–976 (2011).

[99] S Dalavi, P Guduru, and B L Lucht, "Performance Enhancing Electrolyte Additives for Lithium Ion Batteries with Silicon Anodes", *Journal Of The Electrochemical Society* **159**(5), pp. A642 (2012).

[100] Owen C Compton and SonBinh T Nguyen, "Graphene Oxide, Highly Reduced Graphene Oxide, and Graphene: Versatile Building Blocks for Carbon-Based Materials", *Small* **6**(6), pp. 711–723 (2010).